JOURNAL OF
ADVANCED MANUFACTURING TECHNOLOGY

Contents

Volume 10 **Number 1** **January - June 2016**

Chief Editor

First and foremost, warm greetings to all the readers. I am delighted to announce the 18th issue of the Journal of Advanced Manufacturing Technology (JAMT). Currently, JAMT addresses three objectives; to provide a platform for the discussion and knowledge sharing on current and future issues, practices, innovations and trends of engineering and information technology amongst the academics, researchers and practitioners, to promote and encourage exploration and dissemination of knowledge in relation to engineering and information technology, and to publish papers in the areas of engineering and information technology particularly green technology, system engineering, human-technology interaction and emerging technology.

JAMT will continuously be a great and significant contribution to the Faculty of Manufacturing Engineering and UTeM. JAMT strives to attract and engage an international readership that is primarily academic as well .This move is in line with the mission of university "To Be One of the World's Leading Innovative and Creative Technical Universities" JAMT welcomes any papers, either written individually or co-operatively, which will make a substantial contribution to the development and success of the journal. Please do not hesitate to contact us for any uncertainties or enquiries.

I wish to take this opportunity to thank all the individuals involved in this publication particularly the editorial and technical boards for their tireless efforts in ensuring the continued success of JAMT. Moreover, my gratitude is extended to all contributors.

Best wishes and thank you for your support.

DESIGN AND DEVELOPMENT OF UNDERWATER ROBOT FOR CLEANING PROCESS

M.S.M. Aras[1*], M. K.M. Zambri[1], F.A. Azis[1], S.S. Abdullah[2], A.M. Kassim[1]

[1]Underwater Technology Research Group (UTeRG),
[1]Faculty of Electrical Engineering, Universiti Teknikal Malaysia Melaka, Hang Tuah Jaya, 76100 Durian Tunggal, Melaka, Malaysia,

[2]Department of Electric and Electronics, Malaysia-Japan International Institute of Technology, Universiti Teknologi Malaysia, International Campus, Jalan Semarak, 54100 Kuala Lumpur, Malaysia.

Email: shahrieel@utem.edu.my

ABSTRACT: This paper shows the conception and growth of an underwater robot for cleaning operation that can help human beings to perform cleaning tasks underwater. Unmanned underwater vehicles can cut down the danger to human life in term of underwater cleaning job where a human can dive and descent at a certain depth and is not able to stay there in a longer period of time. Underwater Robot for cleaning process was a combination between underwater robot such as Remotely Operated Vehicles (ROV) and cleaning part called Underwater Cleaning Robot (UCR). The main objective of this project was to develop a cleaning tool attached to the ROV to demonstrate the performance of the cleaning procedure as in water treatment operations. By the invention of this UCR, more underwater cleaning job can be done without involving human life. This project began with a design using Solidworks software to capture the dynamics of a newly fabricated UCR. The UCR can perform the cleaning task and this project can give much benefit to the related underwater business especially for the cleaning process.

KEYWORDS: *Remotely Operated Vehicle, Underwater Cleaning Robot (UCR), cleaning process.*

1.0 INTRODUCTION

Over the years, the engineers and scientists have struggled to create a machine or a robot that can help human beings in performing tasks involving underwater situations. Furthermore, shipping industry or catfish pond entrepreneurs face problems in cleaning purposes.For example, to clean the bottom of the vessel, a locksmith should dive under water to do the cleaning. Besides, to collect the rubbish under the sea, divers should dive to the ocean floor to collect it.. This process

takes a long time and can endanger humans lives.

These projects were focusing on designing and developing an underwater robot for a cleaning process. An underwater vehicle is a robot which travels underwater without requiring input from an operator. Underwater vehicle constitutes part of a larger group of undersea systems known as unmanned underwater vehicles. It is controlled and powered from the surface by an operator / pilot through an umbilical or remote control [1]. Hence, the operator can handle the underwater vehicle robot easily to move to any direction for cleaning process. The Underwater Robot for Cleaning Process (UCR) is a robot that is designed for cleaning purposes work under the sea. The main purpose of the creation of this robot is to perform operations that are harmful to humans as the depth of a high pressure can affect the human body. In the current state, most of the underwater cleaning job is done by human such as cleaning the bottom of the vessel, submarine as well as swimming pool [2]. Basically, this robot is using thruster as an actuator part and more likely as Remotely Operated Vehicle (ROV) that uses remote as a controller and is able to successfully complete a cleaning job. This UCR will use a motor pump to suck dirt in the water at any pool and transfer it to the filter division, which contains some filtering material to isolate the impurities and dirt in the water. This cleaning process requires two motor pumps in which one motor pump will be installed at the intake side of the filter and the rest at the outlet side in order to force the water from thr filtering division to come out.

Other than that, the underwater vehicles should have installed the cleaning part as this is a major reason for doing this project. This UCR should be able to perform some cleaning job in the pool or water reservoirs in the laboratory in order to fulfil the objective and scope of this project. By the invention of this underwater vehicle, more underwater cleaning job can be done without risking human life and, on the other hand, the number of human casualty in the sea can be reduced.

Based on three journals [3-5], all projects are related to the underwater cleaning task using different ways. Two of them operate in fully automated, which requires some programming language while the other one operates manually, which requires a pilot to control the whole system. The cleaning tools, method and area of cleaning are also different based on the purpose design and their capability. From the comparison that has been made in [3-5], the Underwater Cleaning Robot (UCR) for cleaning process will be created. This UCR used a manual controller and a pumping system to clean the water. The frame

body of this project utilized aluminium material. There are 6 thrusters used for the UCR propulsion system. The control board used was PSC28A from Cytron Technologies because this board have build-in requirements that were needed for UCR.

2.0 METHODOLOGY

This is the first phase of implementing this project. The first design of UCR using SolidWorks 2013 software can provide the basic structure of the UCR and ease the task of building hardware parts. The software allows users to easily pull in a three-dimensional view. By using this software, users can also measure the material strength in every part of the body frame of the UCR and other equipment installed [6].

2.1 Electronic Part Construction

To control the electronic and electrical part that were installed on UCR such as thruster and cleaning equipment, a control box that contained electronic circuit as a brain of the whole UCR system needed to be installed either by DIY method or plug and play method. For this UCR, PSC28A controller board manufactured by Cytron Technologies was used as a main controller. For smooth operation of the system, the PSC28A board should be used together with PS2 controller [9]. According to the datasheet provide by Cytron, this circuit is directly connected with input and output port / units. The input port is the PS2 controller and the output ports are the motor for the thruster, water pump for ballast tank and cleaning pump [7].

2.2 PSC28A Controller Board

The PSC28A is a circuit board that plays as an interface between PS2 controller and another device that needs to be controlled as shown in Figure 1. It could be connected either through microcontroller or directly to I/O device. The PSC28A does not also require a programming language to perform because the program is inserted inside the PIC microcontroller [7].

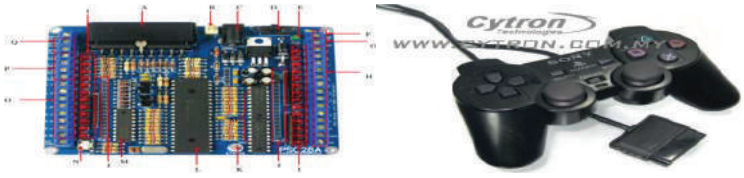

Figure 1: PSC28A controller board and PS2 controller [7]

2.3 Electronic Wiring

Figure 2 showsthe electronic Assembly details which was required for UCR in order to make it work properly. The 12V battery with 3A current power supply was used to supply current and voltage to 6 DC motors for 6 thrusters and water pump. The relay for H-Bridge circuit in was triggered in order to control the movement of the thruster as well as the water pump. Only 5V was required by the PSC28A controller board to power it up. The PSC28A is a circuit board play as an interface between PS2 controller and another device that needs to be controlled.

Figure 2: Electronic Assembly Details

To implement this project, all 6 DC motor for thruster along with water pump (for ballast tank) were wired to the H-Bridge circuit. The H-Bridge circuit board contained 2 single poles 4 throw relay in which each one of it was used either for forward and reverse motion of the thruster and water pump. With this proper connection, every movement like left, right, submerge or float of UCR was possible. This H-Bridge was wired to PSC28A as the relay required 5V power. At the same time, the input signal from the H-Bridge was connected to the PSC28A output terminal. This is important because that was the only way the signal from PS2 joystick controller could be be sent directly to the device that needed to be controlled.

2.4 Motor Driver

L293D is an H-Bridge motor driver which is used to drive a DC motor by using the signal that is generated by a PIC microcontroller as shown in Figure 3. This H-Bridge motor driver enabled voltage to be applied to cross a load (motor) in both directions. The main purpose of using this H-Bridge driver was to control DC motor in both directions either to run in clockwise or counterclockwise. The movement of DC motor could be applied using a combination of transistors and motor in H-Bridge driver in which the transistors would allow current to pass through in one direction only. This led the motor to run either forward or backward according to the position of transistors [8].

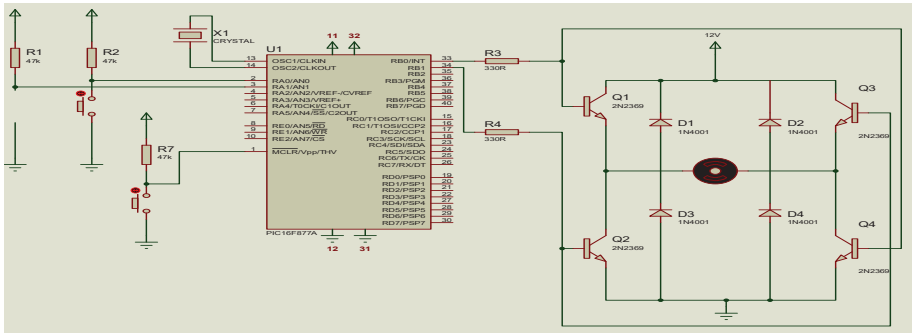

Figure 3: H-Bridge circuit

2.5 Cleaning Process Section

In order to build this project, the cleaning method should be the primary part that needs to be focused on. Based on literature, the water cleaning using sucking method is commonly used. Hence, this method was employed for this study.The dirt contained in the pool water was drawn and filtered using a filter that consists of several layers of filter material using highpowered vacuum or pump motors. This process continued until the water in the pond / pool changed a little from the previous cleaning. Part of this cleaning tools would be installed on the UCR and UCR would be controlled to move across the pond to speed up the cleaning process. This cleaning tool could also clean the most of the bottom surface of the pool at the same time. In order to make this cleaning method perform efficiently, there were several parts that needed to be studied.

3.0 RESULTS AND DISCUSSION

This section will describe and discuss the results and analysis. First, the results based on the design of the project by using SolidWorks software as shown in Figure 4 (a) - (c). Figure 4 (a) and (b) shows the project design with a different position of view using Solidworks. The open frame UCR design was developed because this configuration has been widely adopted by commercial ROV. This is because of its simplicity, robust, easy to maintain, more stable compared with closed hull and cheaper. Figure 4 (c) shows the parameter design of underwater cleaning robot.

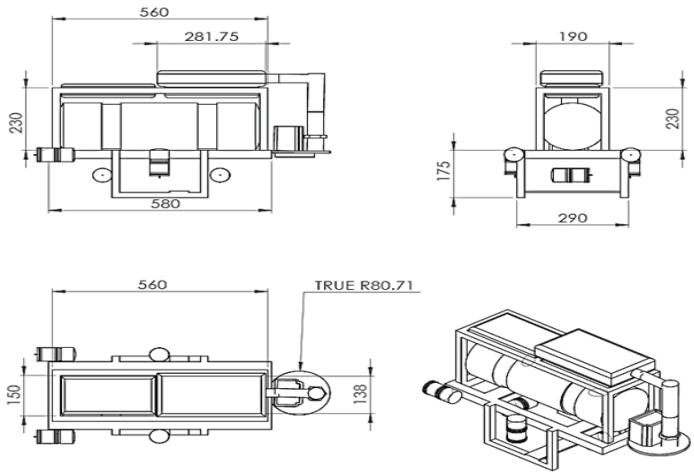

(a) Different view of UCR with dimension

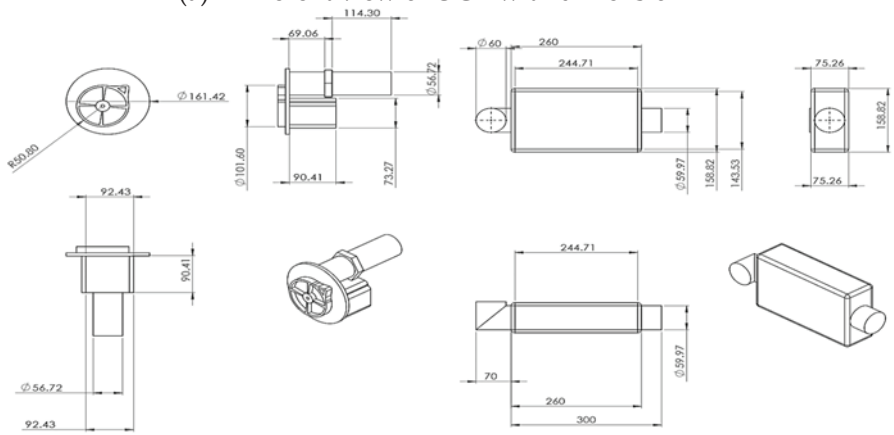

(b) Hose for cleaning system (c) Cleaning system storage

Figure 4: Parameter of design

3.1 Center of Gravity

The UCR used two thrusters for submerge and float movement. The thruster must be placed at the center of the UCR so that submerge and float motion can be conducted efficiently as shown in Figure 5. In order to place the thruster at the center of the gravity, the UCR must be in stable condition as the stability can affect the vertical movement of the UCR. The center of gravity of the UCR can be found by using Solid Work 2013 as shown in Figure 6.

Center of mass X : 423 mm, Y: 7.45 mm, Z: -467 mm

Figure 5: Prototype of UCR

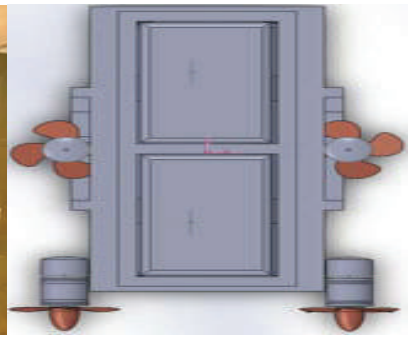

Figure 6: Center of Gravity UCR

3.2 Weight Estimation

The UCR must be floated at underwater level to ensure it can easily float and submerge. In order to do that, the weight of UCR was calculated. The buoyant theory states that, the force act vertically upward to the centroid of UCR and it can be defined mathematically by using Archimedes' principle as shown below [9]:

$$F_b = \gamma_f V_d \tag{1}$$

Where,
F_b =Buoyant force ,γ_f = Specific weight of the fluid, $_{Vd}$ =Displaced volume of the fluid.

In theory, when an object is floating, it displaces a sufficient volume of fluid to balance its height [10]. The application of the equation of static equilibrium in the vertical direction, $\Sigma F_v = 0$. In this case it is assumed that the object is in rest mode in fluid and the positive direction of the upward. The neutral buoyancy is exited when the body of an object stays in position wherever it is submerged in a fluid [11].

When an object is floating,

$$F_b = w = \gamma_f V_d \tag{2}$$

To submerge an object, an external force is required and the force buoyancy is:

$$F_b = w + F_e = \gamma_f V_d + F_e \tag{3}$$

The weight estimation of UCR should be calculated to ensure the UCR can be floated under a water level as needed. The whole part of UCR such as thruster, body frame, lamp, and a cleaning tool is already

submerged when it is placed into the water so that an external force acts on the parts.

3.2.1 Pressure Hull

Figure 7 shows the free body diagram for pressure hull. The unit is in millimeter.

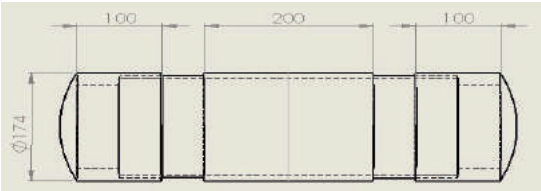

Figure 7: Pressure Hull free body diagram

$$\sum F_v = 0 \quad (4)$$

$$F_b = F_e + w \quad (5)$$

$$W = 2.512\ kg \qquad F_b = \gamma_f + V_d \quad (6)$$

$$\sum V_{dTotal} = V_{di} + V_{dii} + V_{diii} \quad (7)$$

r = 87 mm

$$V_{di} = \frac{1}{2}\left(\frac{4}{3}\pi r^3\right) + \pi r^2 \quad (8)$$

$$= \frac{2}{3}\pi(87^3) + \pi\,(87^2)\,100$$

$$= 3.757 \times 10^6\ mm^3$$

$$V_{dii} = \pi r^2 l \quad (9)$$

$$= \pi\,(87^2)\,(300)$$

$$= 7.133 \times 10^6\ mm^3$$

$$V_{diii} = V_{di}$$

$$= 3.757 \times 10^6\ mm^3$$

$$V_{dTotal} = 3.757 \times 10^6\ mm^3 + 7.133 \times 10^6\ mm^3 + 3.757 \times 10^6\ mm^3$$

$$= 14.647 \times 10^6\ mm^3$$

Water, $\gamma_f = 9.81 \times 10^3\ N/m^3$

$$F_{bl} = \left(\frac{9.81 \times 10^3}{m^3}\right)(14.647 \times 10^6\ mm^3)\left(\frac{1m^3}{10^9 mm^3}\right)$$

$$= 143.69\ N$$

$$F_{el} = F_{bl} - w_1 \quad (10)$$

$$= 143.69 - (2.512 \times 9.81)$$

$$= 119.047\ N$$

3.2.2 Ballast Tank

Figure 8 shows the free body diagram for ballast tank. The unit is in millimeter.

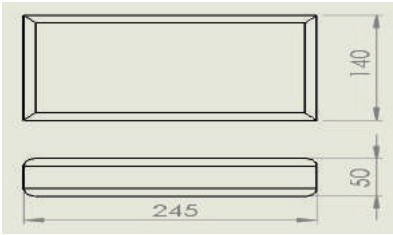

Figure 8: Ballast Tank Free Body Diagram

$$\sum F_v = 0 \quad (11)$$

$$F_b = F_e + w \quad (12)$$

$$W = 0.5kg$$

$$F_b = \gamma_f + V_d \quad (13)$$

$$V_d = l \times w \times h \quad (14)$$

$$= 140 \times 245 \times 50$$

$$= 1.715 \times 10^6 \text{ mm}^3$$

$$F_b = w = 2\left(\frac{9.81 \times 10^3}{m^3}\right)(1.715 \times 10^6 \text{ mm}^3)\left(\frac{1m^3}{10^9 mm^3}\right)$$

$$= 33.648 \text{ N}$$

$$F_{e2} = F_b - w \quad (15)$$

$$= 33.648 - (0.5 \times 9.81)$$

$$= 28.743 \text{ N}$$

3.2.3 Thruster

Figure 9 shows the free body diagram for the thruster. The unit is in millimeter.

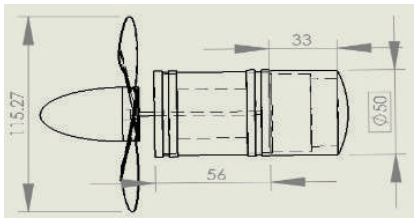

Figure 9: Thruster Free Body Diagram

$$\sum F_v = 0 \quad (16)$$

$$F_b = F_e + w \quad (17)$$

$$w = 0.4 \text{ kg}$$

$$F_b = \gamma_f + V_d \quad (18)$$

$$\sum V_{dTotal} = V_{di} + V_{dii} \quad (19)$$

$$r = 25 \text{ mm}$$

$$V_{di} = \pi r^2 l \quad (20)$$
$$= \pi(25^2)\ (56)$$
$$= 109.95 \times 10^3\ mm^3$$
$$V_{di} = \pi r^2 l \quad (21)$$
$$= \pi(25^2)\ (33)$$
$$= 64.79 \times 10^6\ mm^3$$
$$\sum V_{dTotal} = 109.95 \times 10^3\ mm^3 + 64.79 \times 10^6\ mm^3$$
$$= 174.74 \times 10^3\ mm^3$$
Water, $\gamma_f = 9.81 \times 10^3\ N/m^3$

6 Thruster

$$f_b = 6\left(\frac{9.81 \times 10^3}{m^3}\right)(174.74 \times 10^3\ mm^3)\left(\frac{1m^3}{10^9\ mm^3}\right)$$
$$= 10.28\ N$$
$$F_{e2} = F_b - w \quad (22)$$
$$= 10.28 - (0.4 \times 6 \times 9.81)$$
$$= 13.26\ N$$

3.2.4 Filter Container

Figure 10 shows the free body diagram for Filter containers. The unit is in millimeter.

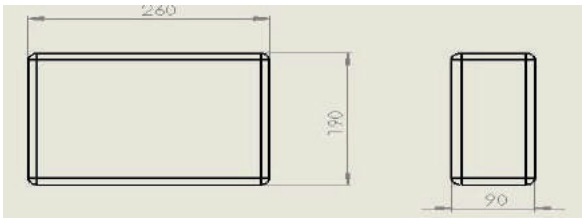

Figure 10: Filter Containers Free Body Diagram

$$\sum F_v = 0 \quad (23)$$
$$F_b = F_e + w \quad (24)$$
$$W = 1.5kg$$
$$F_b = \gamma_f + V_d \quad (25)$$
$$V_d = l \times w \times h \quad (26)$$
$$= 260 \times 190 \times 90$$
$$= 4.446 \times 10^6\ mm^3$$
$$f_b = w = \left(\frac{9.81 \times 10^3}{m^3}\right)(4.446 \times 10^6\ mm^3)\left(\frac{1m^3}{10^9\ mm^3}\right)$$
$$= 43.615\ N$$
$$F_{e2} = F_b - w \quad (27)$$
$$= 43.615 - (1.5 \times 9.81)$$
$$= 28.9\ N$$

Total weight,

$W_T = W_1 + W_2 + W_3 + W_4$

$= 143.69 + 33.648 + 10.28 + 43.615$

$= 231.233$ N

Newton to Kilogram,

$m = 23.57$kg

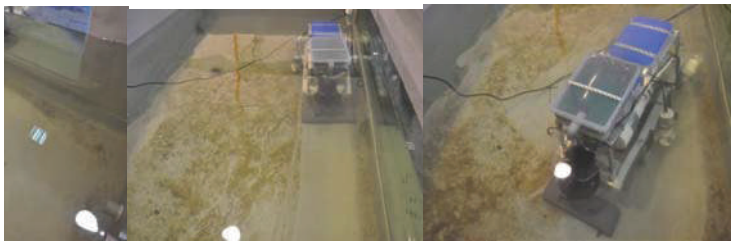

(a) (b) (c)

Figure 11: Cleaning Process Test

During the project, some problem occurs whereby the pressure hull that contained an electronic part was burnt due to a leakage occurred during the experiment as shown in Figure 11. This disaster led to the malfunction of the whole system of UCR. As a result, the whole electronic component needed to be replaced with new ones. To avert that catastrophe from happening in future, more glue and adhesive and other necessary objects were applied. This project did not cover the effectiveness of the cleaning process ,yet can be proposed on future works. This project focused more on design and development of UCR.

4.0 CONCLUSION

The underwater vehicle is one of the important developments in underwater research. This continuous research will guide the human being to know more about underwater lifestyle and based along the knowledge gained, the human can constantly make up new technologies that hold the capabilities in terms of an underwater condition. This technology will enable human to explore, visit as well as exploit place that humans could not otherwise go and replace the human job for cleaning tasks in order to avoid human life risk. The main objective of this project has been achieved where the Underwater Cleaning Robot (UCR) is able to do the cleaning task and some underwater motion as required. The UCR functionality such as forward-reverse left and right turn, float and submerge along with its cleaning method can be easily controlled by using a PS2 joystick controller where the PS2 joystick controller is wired to the PSC28A main controller board. The

UCR can submerge into any condition of the water that is less than 3-meter depth. The Solidworks software and mathematical analysis for every part in the UCR are useful in designing the UCR. This design gives more clarification on how to build the cleaning method for UCR. Hence, several ideas are produced in terms of cleaning puddle water, collecting garbage at the bottom surface of a pool or cleaning the side wall of a pool. In future works, the effectiveness of the cleaning process of the UCR will be tested.

ACKNOWLEDGMENTS

We wish to express our gratitude to Universiti Teknikal Malaysia Melaka (UTeM). Special appreciation and gratitude to Underwater Technology Research Group (UTeRG), Centre of Research and Innovation Management (CRIM) and to Faculty of Electrical Engineering from UTeM for giving the financial and moral support in completing this project successfully.

REFERENCES

[1] S.W. Moore, H. Bohm, V. Jensen, *"Underwater Robotic Science, Design &Fabrication", Marine Advance Technology Center, MATE",* 2010.

[2] M.H. Lee, Y.D. Park, H.G. Park, W.C. Park, S. Hong, K.S. Lee, H.H. Chun, *"Hydrodynamic Design of an Underwater Hull Cleaning Robot and its Evaluation"*, Pusan National University, Busan Korea.

[3] H. Albitar, A. Ananiev, I. Kalaykov, *"New Concept of In-Water Surface Cleaning Robot"*, School of Science and Technology Orebro University Sweden, 2013.

[4] Y. Li, K.M. Lo, *"Novel Underwater Vehicle-Manipulator for Cleaning Water Pool"*, Department of Electromechanical Engineering, University of Macau, 2009.

[5] D.M. Kocak, J.W. Neely, J. Holt, M. Miyake, *"A Specialized ROV for Cleaning Groundwater Recharge Basins"*, Harbor Branch Oceanographic Institution, Engineering Division, 1999.

[6] BS SolidWorks *"http://www.solidworks.com/"*, 2013

[7] Cytron Technologies PS2 I/O Converter PSC28A User Manual. *"http://www.solidworks.com/"* November 2013.

[8] Z.M. Sani, A. Noordin, A.M. Kassim, A.Z Shukor, *" Microcontroller Technology 2nd Edition"*, Universiti Teknikal Malaysia Melaka, UTeM, 2012.

[9] M.S.M. Aras, F.L. Sudirman, F.Ashikin Ali, F.A.Azis. SMSSA.Hamid, A.S.M. Nor, L.W. Teck, Faculty of Electrical Engineering, UTeM. *"Underwater Technology Research Group (UteRG) Glider for Monitoring and Surveillance Applications"*, 2011.

[10] Mohd Aras, Mohd Shahrieel and Ab Rashid, Mohd Zamzuri and Azhan, Ab. Rahman (2013) *Development And Modeling Of Unmanned Underwater Remotely Operated Vehicle Using System Identification For Depth Control.* Journal of Theoretical and Applied Information Technology, Vol 56 (1). pp. 136-145. ISSN 1992-8645.

[11] Ali, Fara Ashikin and Abdul Azis, Fadilah and Mohd Aras, Mohd Shahrieel and Muhammad Nur, Othman and Shahrum Shah, Abdullah (2013) *Design A Magnetic Contactless Thruster of Unmanned Underwater Vehicle*. International Review of Mechanical Engineering (I.RE.M.E.), 7 (7). pp. 1413-1420. ISSN 1970-8734.

THE INFLUENCE OF EXTRUSION DIE ANGLE DURING THE HOT EXTRUSION PROCESS OF AL ALLOYS

H.R. Rezaei Ashtiani

Department of Mechanical Engineering, Arak University of Technology, Arak, Iran.

Email: hr_Rezaei@arakut.ac.ir

ABSTRACT: One of the most important parameters for the hot extrusion process effecting the deformation force, material flow, microstructural and mechanical properties of the extruded material is the Extrusion Die Angle (EDA). In this investigation, the effects of EDA on load, material flow and microstructure of hot extruded commercially pure aluminum has been studied. The finite element simulation were carried out using Deform 3D. Finite element modeling shows that the values of the equivalent plastic strain and its distribution, flow material and deformation forces depend extremely on deformation temperature, reduction and EDA. To estimate the reliability of the numerical analysis, the FE model was validated using experimental results. The results showed that the lowest extrusion force occurs in an optimum die angle for each reduction. Optimum EDA obtained 16, 18 and 23 degrees at reductions of 50%, 60% and 70%, respectively. Also, material flow, inhomogeneity of microstructure and the equivalent plastic strain increases with increasing of EDA.

KEYWORDS: *Die angle; FEM; Hot extrusion; Material Flow; Microstructure; Reduction.*

1.0 INTRODUCTION

The advantages of aluminum and its alloys make it particularly appropriate for complex extrusion processes. High ductility and the ideal ratio of strength to mass density in aluminum alloy prepare various applications in automotive and aircraft manufacturing, and also in lightweight construction [1]. Nearly 80% of all metals products consisting of aluminum alloy undergo hot forming during some part of their processing history [2]. Hot deformation processes are a fundamental step in the production of engineering parts which require not only dimensional accuracy but also suitable microstructural and mechanical properties with minimization of load and energy. Therefore investigation of materials behavior during hot deformation is very essential.

Hot extrusion is one of the most important processes used to produce aluminum alloys. Minimization of load and energy, deformation homogeneity and controlling of microstructure of the extruded material are considerable aspects in die design process. It is commonly accepted that product properties are strongly correlated to microstructure. So it is of paramount importance to understand the way in which the structure is modified and how the forming parameters (i.e. die geometry, reduction, temperature, etc.) affect these modifications.

Simulation of hot forming processes with application of finite element method (FEM) has been the subject of many recent works. High temperature and large plastic deformations of the extrusion processes have led to developments in the microstructure of the material [3-7].

Joun and Hwang [8] applied a finite-element-based optimal process design technique in steady-state metal forming to die profile design in forward extrusion. They predicted the die profile for minimization of forming energy for various process conditions and materials. Lee et al. [9] designed the optimal die profile for hot rod extrusion that could yield more uniform microstructure. They applied the flexible polyhedron search (FPS) method to obtain the optimal die profile, and to show validity of result of their study, performed a hot extrusion experiment.

Byon and Hwang [10] presented a process optimal design methodology to minimize the punch force in steady-state forming process by using the finite-element method. The influences of die profile on the microstructural changes of the hot extruded sample have not been investigated in the previous researches. In the meantime, the effects of other parameters of hot extrusion process including temperature, friction coefficient, reduction and etc. have been disregarded in the prior investigation.

In this paper, the optimum angle of conical die is achieved using finite-element method for hot extrusion of pure aluminum rod. Also, the simulation results have been verified by experimental data, and finally, microstructural changes have been investigated for different die angles and various hot extrusion conditions.

2.0 MATHEMATICAL MODEL

2.1 Mechanical Model

As shown by Eq. (1) the actual work, W_a, to complete the extrusion process is the sum of the ideal work, W_i, that would be required for the shape change in the absence of friction and inhomogeneous flow, the work against friction between work and tools, W_f, and the work to do redundant or unwanted deformation, W_r [11].

$$W_a + W_i + W_f + W_r \tag{1}$$

Unlike the ideal work, the friction and redundant work depend on die angle. As it is clear from Figure 1, for a given reduction, the contact area between the die and material decreases with increasing die angle; so with a constant coefficient of friction, frictional work decreases while the redundant work term increases with die angle. Therefore, for each reduction, there is an optimum die angle, for which the total work is a minimum [11].

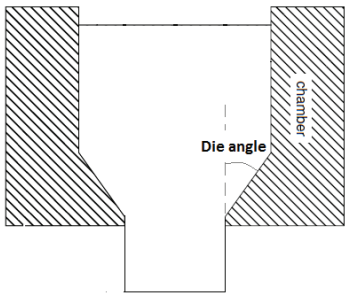

Figure 1: A typical conical die

Generally, the hot deformation behavior of metals and alloys are characterized by stress, strain, strain rate and temperature. The equations covering these values varying in wide ranges are given as [12]:

$$Z = \dot{\varepsilon} \exp\left(\frac{\Delta H}{RT}\right) = A(\sinh \alpha\sigma)^n \tag{2}$$

$$\sigma = \frac{1}{\alpha}\left\{\left(\frac{Z}{A}\right)^{1/n} + \left[\left(\frac{Z}{A}\right)^{2/n} + 1\right]^{1/2}\right\} \tag{3}$$

where σ is the flow stress, T is the absolute temperature, Z is the temperature compensated strain rate and commonly known as Zener-Hollomon parameter, A is a constant, n, ε, ΔH and R are the power exponent, the strain rate, the activation energy and the universal gas constant, respectively. The behaviour of an aluminum alloy during extrusion as a thermomechanical process depends on temperature, strain (reduction) and strain rate (ram velocity), as described by Eqs, (2) and (3).

2.2 Microstructural Model

Evolution of microstructural changes during hot extrusion is a very complicated operation. The distribution of microstructure through cross section and along the length of extrusion die varies considerably under normal extrusion conditions. This causes a non-uniform distribution of mechanical properties and hence may necessitate extra post-extrusion operations such as machining away the recrystallised layer.

The relationship between the volume fraction recrystallised and the holding time is generally represented by the JMAK equation clarified by Eq. (4) [13].

$$X_V = 1 - \exp\left\{-0.693\left(\frac{t}{t_{50}}\right)^k\right\} \tag{4}$$

Where X_V represents the static recrystallized volume fraction achieved at the annealing temperature, t is annealing time, k is the Avrami exponent with a commonly reported value of 2, t_{50} is the time to 50% static recrystallization. There are two kinds of models consisting of empirical and physical models for the calculation of t50. The empirical model bypasses the evolution of substructure, and relates the final microstructure with strain, strain rate and temperature by regression of the experimental data. The only advantage of this model is its easy usage.

$$t_{50} = A d_0^a \varepsilon^{b'} Z^c \exp\left(\frac{Q_{rex}}{RT_a}\right) \tag{5}$$

A, a, b', c are constants, d_0 is the initial grain size, ⌀ is the equivalent strain, Q_{rex} is the activation energy for recrystallization, R is the universal gas constant, Ta is the annealing temperature and Z is the Zener-

Hollomon parameter.

For the physical model, t_{50} is calculated based on the stored energy (P_D) and the density of recrystallization nuclei (N_V):

$$t_{50} = \frac{C}{M_{GB} P_D} \left(\frac{1}{N_V} \right)^{1/3} \tag{6}$$

where C/M_{GB} is a calibration constant.
As shown by Eq. (3) the recrystallized grain size is expressed as a function of initial grain size, strain, strain rate, and temperature.

$$d_{rex} = a_2 d_0^{h_2} \varepsilon^{n_2} \dot{\varepsilon}^{m_2} \exp\left(Q_2 \big/ RT \right) + c \tag{7}$$

where a_2, h_2, n_2, c and m_2 are material constants.
The kinetics of grain growth is described by isothermal equation as presented in Eq. (8).

$$d_{gg} = \left[d_{0g}^m + a_g t \exp\left(-Q_g \big/ RT \right) \right]^{1/m} \tag{8}$$

where d_{gg} denotes the final grain size after growth and holding time of t, whilst d_{0g} is the grain diameter prior to the holding period, a_g and m are materials constants, and Q_g is activation energy of grain growth.

2.3 Finite Element Modeling

The Finite Element Modeling (FEM) is one of the most precise methods to analyze the forming process, which is usually non-linear, thermomechanical coupled and involves very large deformations. To date, various models have been proposed and integrated into FEM programs to study the load and microstructure response under various forming conditions, and to control the microstructural evolution.

In this work, a 3D model has been constructed to simulate the hot extrusion process for aluminum alloys using finite element program DEFORM™. The billet is assumed to behave as a thermo–elastic viscoplastic material with temperature-dependent elastic modulus and poisson's ratio. The range of temperatures, strains and strain rates experienced by the material during the extrusion process is large, hence

it is necessary to define the plastic behavior of the billet as a function of temperature, strain and strain rate. This was done using a hyperbolic sine equation, shown in Eq. (3), which relates the steady state flow stress of the material to the strain rate and temperature under which it is deformed. It is also assumed that the die and stem materials behave as a rigid solid.

The geometry of the billet, stem and die of hot extrusion at the reduction value of 50% shown in Figure 2. The die with a round opening had a bearing length of 2.5 mm.

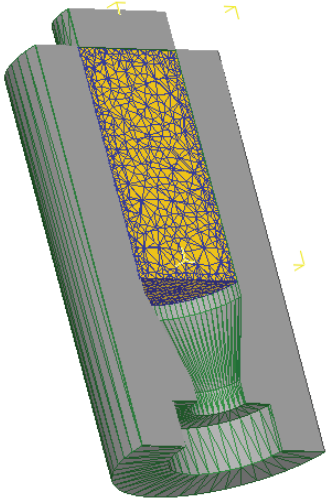

Figure 2: Billet, stem and die in FE model.

The process was carried out at three initial temperatures of 350 ºC, 450 ºC and 550ºC. Also three reductions of 50%, 60% and 70% have been studied. The density of the billet was assumed to be constant at 2710 kgm-3. Coefficient of friction depending on applying lubricant comes from test conditions.

3.0 EXPERIMENTAL PROCEDURE

3.1 Material

The chemical composition of the AA1070 aluminum alloy employed in this work is given in Table 1.

Table 1: Chemical composition of AA1070

%Ga	%Ti	%Cu	%Fe	%Zn	%Si	%Al
0.010	0.0126	0.0102	0.199	0.0102	0.0788	99.7

Aluminum billets were cut from a bar of AA1070 with 16mm in diameter and 30mm in height (that was reduced by wire drawing) to be used for the experiments. Samples were first annealed at 600 ºC with two holding time consisting of 5 and 50 min and then air cooled so that two initial grain sizes of 40 and 200 μm were obtained.

3.2 Equipment and Extrusion die

The schematic diagram of the die-set used in this study is shown in Figure 3. Three conical dies with a half angle of 10, 20 and 30 degrees have been constructed for the reduction of 50%. The die-set consists of die, container, punch, lower and upper shoes and rings. Samples were hot extruded under initial temperatures like FEM program. A5 glass lubricant was applied manually on the surfaces of the billet and die and container.

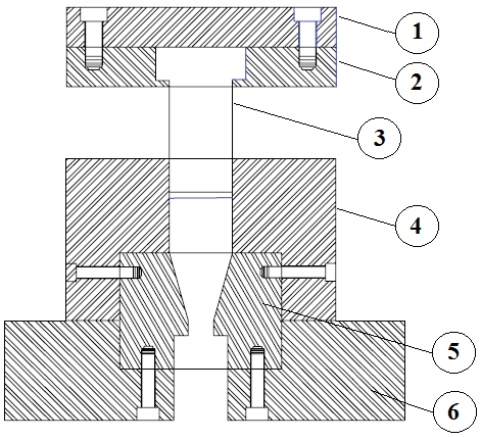

Figure 3: Schematic diagram of the die-set, (1) upper shoe, (2) holder ring, (3) punch, (4) container, (5) die and (6) lower shoe.

The best resolution of microstructures for investigation of microstructural changes and determination of grain sizes of annealed and hot extruded

samples is achieved by the examination of electrolytically anodized samples in a polarized light microscope (PLM). Figure 4a illustrates the die set; while Figure 4b shows the specimen before and after the tests.

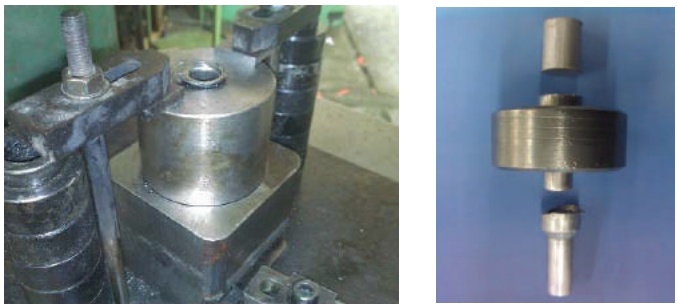

(a) (b)

Figure 4: Extrusion condition: (a) die-set and (b) billet and deformed sample

4.0 RESULTS AND DISCUSSION

The influence of die angle on maximum extrusion load illustrated in Figure 5, at reduction of 50% and the temperature of 450ºC and punch speed of 50mm/sec. As it is clear from this Figure, there is an optimum die angle, for which the maximum extrusion load is a minimum. Due to the similar condition, except for the die angle, it can be concluded that just the suitability of die angle causes this decreased load. Also, it is obvious from Figure. 5a that the experimental data and simulation results (FEM) have proper accordance at different die angles.

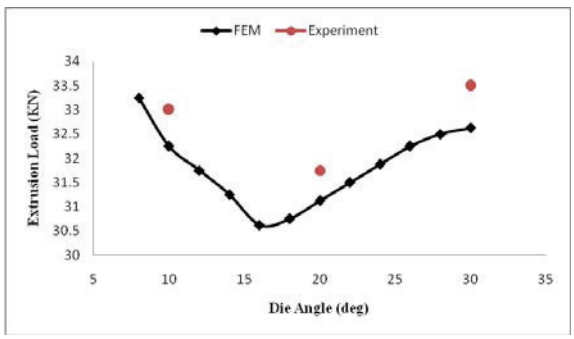

(a)

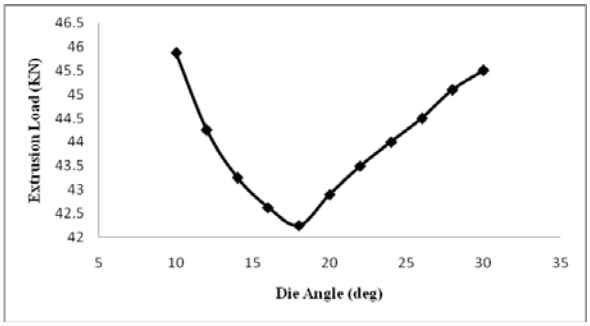

(b)

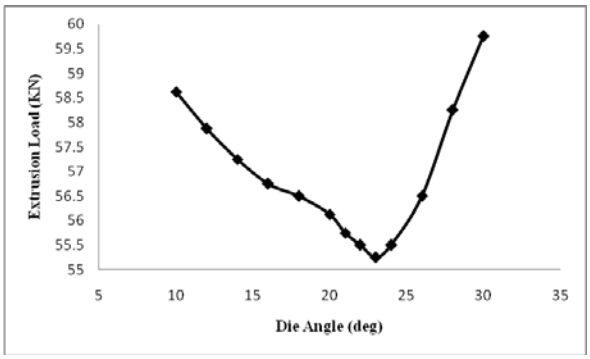

(c)

Figure 5: Influence of die angle on the maximum required extrusion load for different value of reduction: (a) 50%, (b) 60%, (c) 70%

The influence of reduction on the amount of required maximum load and optimum die angle resulted from the simulation is presented in Table. 2. It is clear that the amount of reduction can affect on the optimum die angle. In a same condition, the optimums die angle increases with increasing of the reduction amount.

Table 2: Reduction effects on the required maximum load and optimum die angle

Amount of reduction	50%	60%	70%
Required maximum load (kN)	30.62	42.19	55.25
Optimum die angle (deg)	16	18	23

Figure 6 shows distribution of the effective strain at different regions of deformation in the half cross-section of hot extruded billet. As illustrated in this Figure, the effective strain has a non-uniform distribution in the deformation zone.

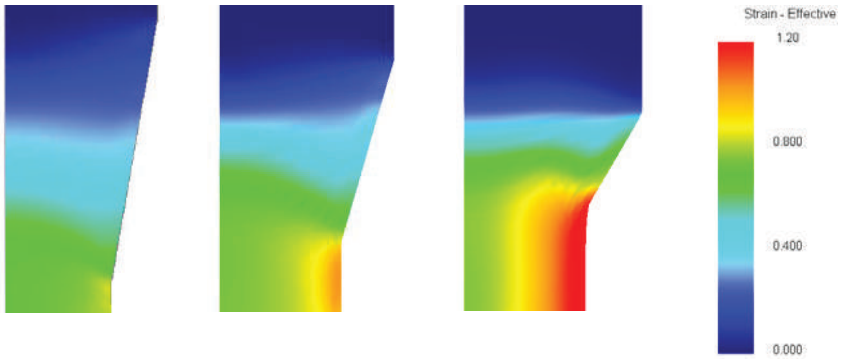

(a) (b) (c)

Figure 6: Distribution of effective strain for die angle of (a) 10º, (b) 16º and (c) 30º in the deformation zone

As can be seen from Figure 7, the amount of EDA can strongly control the manner of strain distribution and strain inhomogeneity.

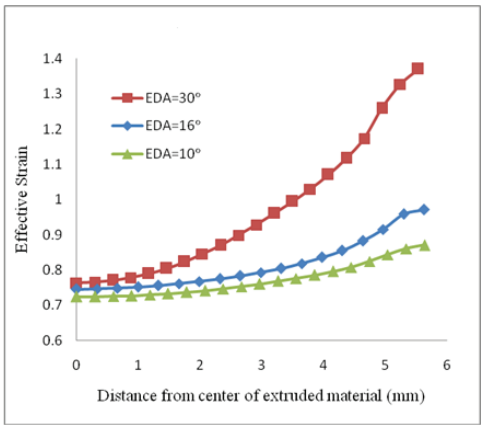

Figure 7: Effects of EDA on the distribution of effective strain at the exit position of deformation zone

The amount of effective strain increases with increasing dies angle. Also, inhomogeneity of the effective strain increases with increasing of distance from the center to the surface of the extruded material.

The effects of deformation temperatures on the maximum required load for different reductions during the hot extrusion process are illustrated in Figure. 8. It is obvious that the alternations and values of

the hot extrusion load increases with increasing of reduction values. Meanwhile the values of hot extrusion load decreases with increasing of deformation temperature values.

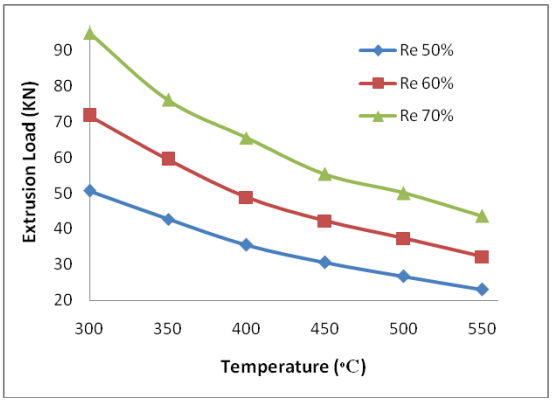

Figure 8: The variation of extrusion load at different deformation temperatures and reductions.

The influences of die angles and friction coefficients on the extrusion load are shown in Figureure 9. It is clear from this Figureure; extrusion load gradually decreases and after that increases with an increase in the die angle. Also, it is obvious that extrusion load increases with increasing of friction between die and workpiece surface.

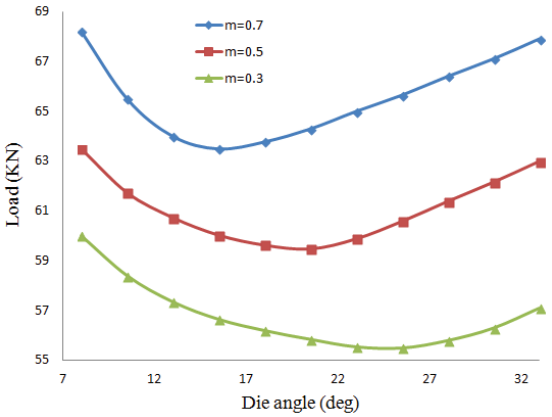

Figure 9: The variation of extrusion load at different friction coefficients and die angles.

Microstructures of the two samples with initial grain size of 40 and 200 μm before hot extrusion illustrated in Figures 10a and 10b, respectively. To investigate the initial microstructure, the samples are first annealed at 600 ºC with two holding times of 5 and 50 min, and

then air cooled, so the grain size of samples obtained are about 40 and 200 μm, respectively.

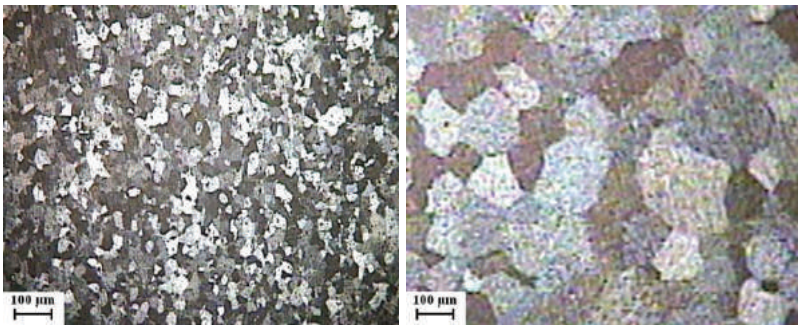

(a) (b)

Figure 10: Microstructures of samples before hot extrusion at annealing temperature of 600 ºC and holding time of (a) 5 min and (b) 50 min.

Microstructures of samples hot extruded at the temperature of 450ºC are shown in Figure 11. As shown in this Figure, severely elongated grains are observed at hot extruded sample with initial grain size of 200 μm, which suggest that dynamic or static recovery be the main restoration process during or after the hot extrusion.

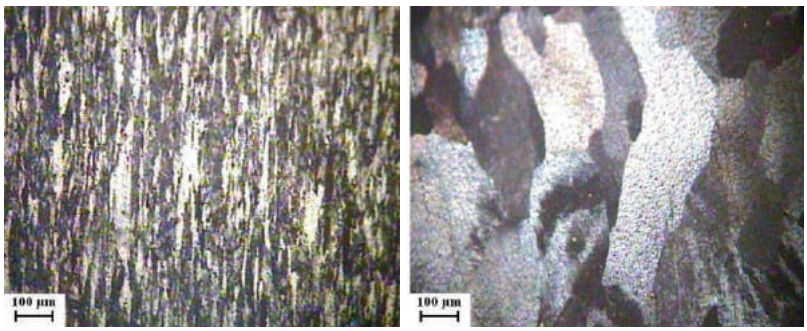

(a) (b)

Figure 11: Microstructures of samples after hot extrusion with die angle of 20º for two initial grain sizes of (a) 40 μm and (b) 200 μm.

In Figure 12, the influence of die angle on microstructure evaluation is illustrated. Detailed microstructural observation indicates that more homogenous structure in Figure 12(b) is due to the extrusion process with die angle of 20º which is close to the optimum die angle obtained from simulation.

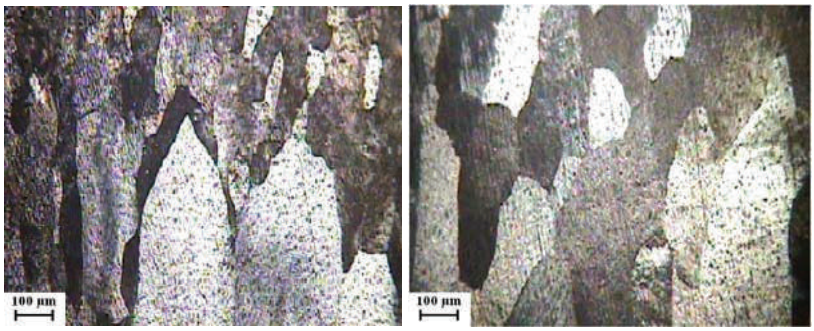

(a) (b)

Figure 12: Microstructures of samples after hot extrusion at the temperature of 550 ºC with two die angles of (a) 20º and (b) 30º.

5.0 CONCLUSIONS

In this work, a mathematical model based on the finite element analysis was proposed to predict the optimum die angle during the hot extrusion process of aluminum alloy. Deformation forces, material flow and microstructural evaluation of the hot extruded material affected by Extrusion Die Angle (EDA), were investigated. The results show that at each reduction, there is an optimum die angle providing minimum extrusion load. In the same conditions, optimum die angle increases with increasing the amount of reduction and decreasing friction of die. The results also show that the values of the equivalent plastic strain and its distribution depend extremely on EDA. The equivalent plastic strain increases with increasing of EDA. Investigations show that temperature is one of the most prominent parameters that controls the process.

Finally, microstructural investigations show that EDA and the other processing parameters of hot extrusion have efficient effects on the microstructure of hot extruded sample, as the optimum die angle prepares more homogenous microstructure.

REFERENCES

[1] J. G. Kaufman, Introduction to Aluminum Alloys and Tempers, ASM International, Materials Park, OH 44073-0002; 2000.

[2] Brown, K.H. Kim, L. Anand, An internal variable constitutive model for hot working of metals, *Int. J. Plasticity*, 5 (1989) 95–130.

[3] HR. Shercliff, A. M. Lovatt ER, "Modelling of microstructure evolution in hot deformation." Philosophical Transactions of the Royal Society A: Mathematical, *Physical and Engineering Sciences* 357, pp. 1621–1643, 1999.

[4] Furu, H.R. Shercliff, C. Sellars, M. Ashby, "Physically-based modelling of strength, microstructure and recrystallisation during thermomechanical processing of Al–Mg alloys." *Material Science Forum* 217–222, pp. 453–458, 1996.

[5] M. Sellars, Q. Zhu, "Microstructural modelling of aluminium alloys during thermomechanical processing." *Materials Science and Engineering A* 280 (1), pp. 1–7, 2000.

[6] Sheppard, "Prediction of structure during shaped extrusion and subsequent static recrystallisation during the solution soaking operation. *Journal of Materials Processing Technology* 177 (1–3), pp. 26–35, 2006.

[7] Chanda, J. Zhou, J. Duszczyk, "A comparative study on iso-speed extrusion and isothermal extrusion of 6061 Al alloy using 3D FEM simulation" *Journal of Materials Processing Technology* 114 (2), pp. 145– 153, 2001.

[8] M.S. Joun, S.M. Hwang, "Optimal process design in steady state metal forming by finite-element method. I. theoretical consideration", *Int. J. Mach. Tools Manuf.* 33 (1993) 51–61.

[9] S.K. Lee, D.C. Koo, B.M. Kim, "Optimal die profile design for uniform microstructure in hot extrusion", *Int. J. Mach. Tools Manufact.* 40 (2000) 1457–1478.

[10] S.M. Byon, S.M. Hwang, "FEM-based optimal design in steady-state metal forming", *J. Comp. Struct.* 79 (2001) 1363–1375.

[11] W.F. Hosford, R.M. Caddel, "Metal Forming, Mechanics and Metallurgy", Prentice-Hall, 1983.

[12] T. Sheppard, "Extrusion of Aluminium Alloys", Kluwer Academic Publishers, Dordrecht, 1999, p. 127.

[13] E. S. Puchi-Cabrera, C. J. Villalobos-Gutiérrez, A. Carrillo, F. DiSimone "Non-isothermal annealing of a cold rolled commercial twin roll cast 3003 aluminum alloy", *JMEPEG* 12 (2003) 261-271.

LASER FORMING OF METALLIC DOME-SHAPED PARTS USING SPIRAL AND RADIAL-CIRCULAR SCAN PATHS

S.H., Dehghan[1], M., Loh-Mousavi[2] , M., Farzin[3] and M., Safari[4*]

[1]Department of Mechanical and Manufacturing Engineering, Faculty of Engineering, Universiti Putra Malaysia, Serdang, 43400 Selangor, Malaysia.

[2]Faculty of Mechanical Engineering, Khomeinishahr Branch, Islamic Azad University, Khomeinishahr, Isfahan, Iran.

[3]Faculty of Mechanical Engineering, Isfahan University of Technology, Isfahan, Iran.

[4]Department of Mechanical Engineering, Arak University of Technology, Arak 38181-41167, Iran.

Email: m.safari@arakut.ac.ir

ABSTRACT: Laser forming process is a new flexible forming process without any contact between rigid tools and sheet metal, in which the form of a sheet metal is changed permanently by high thermal stresses caused by laser. In general, laser forming of spatial shapes and laser forming of two dimensional simple shapes are different. On one hand, heating path and pattern of thermal stress are increasingly being used in a laser forming process, which are especially important in forming three dimensional complicated parts. In a laser forming technique, a desired final shape can be achieved by a control of the laser scan path and other process parameters such as laser irradiation pattern, laser power, speed of laser scan and laser beam diameter. A new application of the laser forming process is production of dome-shaped parts as a prototype. For the production of curved parts, especially for the dome -shaped ones, different strategies have been developed which are mostly based on curved irradiation paths. In this paper, a circular-radial strategy of scanning path to form dome shapes by using laser is investigated. Experiments have been carried out to validate the numerical results. As a result, a new scanning pattern is presented as a spiral strategy. It was shown that the stress distribution is more uniform in laser forming with the use of spiral scanning path. In addition, the deformed parts with spiral scanning path are more uniform compared to other scanning paths investigated. Furthermore, it was found that laser forming with radialcircular scan paths will result in buckling mechanism whereas spiral irradiation will lead to gradient mechanism. The study also shows that radial and circular irradiations lead to occurrence of low thermal gradient and buckling mechanism. Additionally, low thermal gradient and buckling mechanism is happened by spiral irradiation. Finally, thickness distribution and temperature gradient of the deformed parts caused by different laser paths have been investigated.

KEYWORDS: *Laser Forming, Finite Element, Dome Shaped, Spiral Path.*

1.0 INTRODUCTION

Laser Forming is an advanced technology that has been developed in order to shape metal parts. The process is obtained by thermal stress to steel sheet by controlled radiation from a focused laser beam. Laser forming is a combination of mechanical heat process in which heat is applied by a laser beam on one side of the sheet metal in a specific direction [1]. Stress-strain relation on the sheet is not only nonlinear, but also is temperature dependent. In the laser forming process, the shape and position of a bend are determined by radiation exposure rate, beam size, and the position of the laser beam, all of which are considered process variables. In traditional forming techniques such as bending, stretching and pressing, heavy-duty tools are required for the applied external forces to transform a flat piece of sheet metal by devices or the form in which the deformation process can be completed. The biggest advantage of the laser forming technique compared to the traditional method is production flexibility and cost reduction as well as production time. Various applications of the laser forming process have been identified to shape the macro aspects of rapid prototyping and proofing industries like automobile, aerospace and ship building. Aspects of laser forming of micro-industry microelectronic components to precisely adjust the shape of laser applications and several new methods of laser forming are under review and development. Features of this process include extremely high reliability, flexibility, production of complex shapes, capability of rapid prototyping, production of high-precision, low recalculation and access to the detailed form of the slight return spring. Types of mechanisms that are produced by laser are as follows:

- Thermal gradient process
- Buckling process
- Upsetting process

As the gradient heat process suggests, the process depends on the creation of high slope heat in sheet thickness and it is caused as a result of bending the sheet towards the laser beam. Process buckling is created when the slope of heat in sheet width is small and due to low thickness of sheets, the diameter of heated region is bigger than sheet thickness. The result of the process is sheet bending towards laser beam and away from the laser beam. In the upsetting process, the heating conditions are the same as the other two mechanisms, but due to geometrical constraints, it is not possible to do sheet bending and, for this reason, deformation leads to an increase in the thickness or the upsetting of the sheet. In the general states, because of high thickness of sheets, a

diameter of heated region is equal to sheet thickness, a mechanism that causes reduction in the length of the sheet, but bending does not occur [2].

A new application of forming process using laser is called controlled irradiation as the specific pattern on the metal plates to create specific pieces for quick prototyping and production of small parts. Forming the circular plates as bowl-shaped or dome-shaped requires a contraction within a sheet and a bend outward of the sheet.

To manufacture complex curved space components (such as a domeshaped), somewhat different irradiation patterns on curved lines and curved radiation are to be discussed. In general, if curved lines of radiation are used instead of straight lines, collections of threedimensional laser forming will be created and thereby a significant change in the nature of the process and its dependence on the geometry of the components can be created [3-4].

Since 2000, Laser research group at the University of Liverpool has conducted extensive research in the field of laser forming alloys and composite materials used in aerospace industries, as well as forming a complex three-dimensional laser body and parts of the ship [5-8]. Edwardson offered radiation pattern to form a saddle-shaped surface and proposed an alternative model for the formation of a surface which is presented as a pillow [9]. Li and Yao presented a process based on the finite element method to determine the path of irradiation, irradiation step, exposure rate and exposure to form a curve in two dimensions [10]. On the other hand, Maggie and her colleagues studied concentric lines with upsetting mechanism in a laser forming of a domed surface [11]. Through experimentation on the circular ring segment of steel SAE1008 with 2-mm diameter, Hennige showed that the required amount of exposure of laser for circular plates and annular plates is lower in comparison with rectangular plate. Moreover, in the circular sections, aberration and distortion are more than that of ring sections [12-13]. Following the research done by Hennige et al, a radiation pattern consisting of radial radiations under upsetting mechanism and circular radiations under a temperature gradient mechanism for producing domeshaped surfaces are proposed. In the previous researches, two different irradiating schemes were used to produce double curvature shapes with laser beam. In the first irradiating scheme, circular paths were used. Also, in this irradiating scheme, thermal gradient mechanism was considered to be dominant. In the second irradiating scheme, the radial straight lines were used and the dominant mechanism was UM. Both of these irradiating schemes have their own advantages and

disadvantages depending on the initial geometry of the sheets [14].

In the second irradiating scheme, if only radial lines are used, the successive positions of the radiation will be very important, because not only can a linear beam be radiated at each step, but the residual stress distribution asymmetry can also be created as a result of the asymmetric shape. Therefore, the symmetry of the piece must be provided with successive radiations. These patterns are shown in Figure 1 [15].

Due to the disadvantages mentioned about radial pattern and circular pattern, a new irradiating scheme was presented by Henning for production of a dome-shaped plate in 2000. This irradiating scheme was a combination of both radial and circular patterns and aforementioned disadvantages were eliminated using this scheme. In this pattern, concentric lines are used in order to stabilize the plate due to the open edges curved radial lines during the heating process.

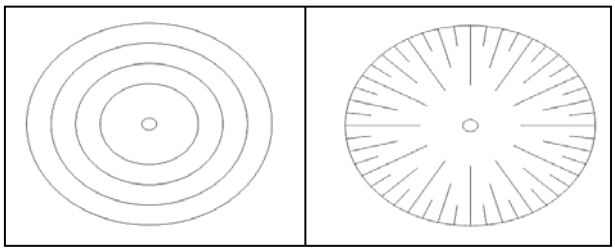

(a) (b)

Figure 1: (a) Pattern of concentric circles (b) Pattern of radial lines

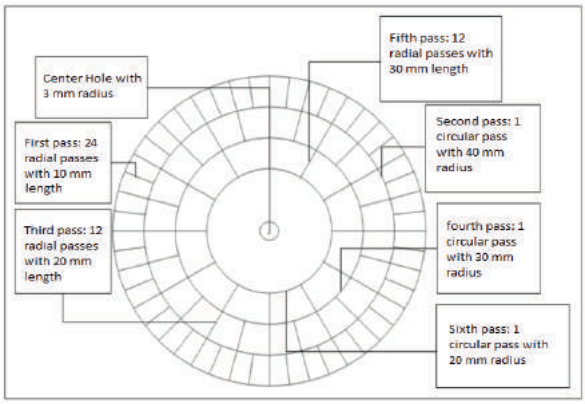

Figure 2: Radial - circular pattern [12]

In this paper, a new irradiating scheme is proposed for the production of a double curvature dome-shaped pattern from a circular blank. At first, one of the irradiating schemes that have been proposed by other researchers is used in the experimental and numerical works. In this stage, numerical simulations are verified with experimental observations. After this verification, numerical simulations of laser forming of a double curvature dome shape are performed along with spiral irradiating scheme. Finally, a comparison is made on the results of the produced dome-like shape with spiral irradiating scheme and the scheme contains circular paths. The results will be shown in terms of distribution of residual stresses, achievement of the domed-like shape, rate of edges symmetry and forming condition of edges. Spiral pattern is much better than the circular-radial pattern.

2.0 EMPIRICAL ANALYSIS

In this study, a source of carbon dioxide laser along with a power of 150 Watts was used. In order to move the samples to create necessary exposure pathways, a three-axis CNC workstation was used. A circular blank of 100 mm diameter and a- 1 mm and 2 mm thickness were cut from the as-received low carbon steel and were used as a specimen. In Figure 3, experimental setup of laser forming of circular blank is shown.

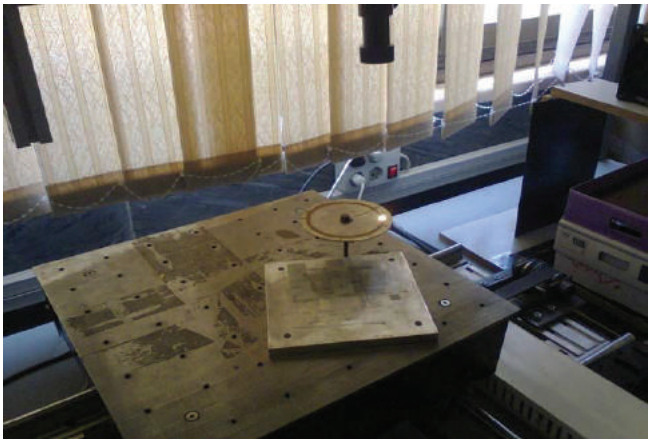

Figure 3: Configuration and installation of the work piece formed by radial - circular path with a thickness of 1 mm

In the following empirical analysis, a closer examination of the temperature distribution and the effect of intermittent and parallel exposure over time are examined. As indicated in Figure 4 in a straight line along the path of exposure, a third beam irradiation

was investigated. Initially, the temperature begins to rise due to the convective effect of the temperature, but when focused beam of laser reaches to the edge of the plate, convection between the laboratory and the sheet metal reduces the surface temperature of the sheet.

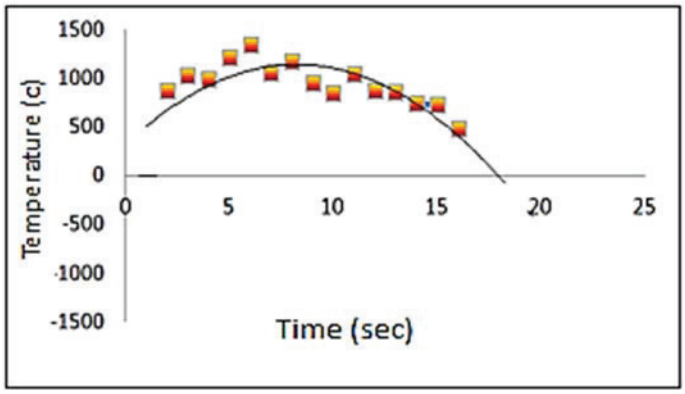

Figure 4: Plot of the variation of temperature during laser irradiation pitch 5 mm

3.0 FINITE ELEMENT ANALYSIS

In the finite element analysis of the forming process made by laser, ABAQUS software was used [16]. This analysis is also done implicitly. In the analysis related to simulations, mechanical calculations can be decoupled from the thermal ones. This is because of negligible energy dissipation from plastic deformation as compared with the high laser energy used in the process. In the decoupled solution, the thermal analysis is performed first to obtain the temperature field, and then the results of thermal calculations are used as the thermal loading for the mechanical analysis. During the process of formation used by laser and heat flux distribution on the sheet, the following equation is obtained:

$$q_{(r)} = \frac{2\eta P}{\pi R^2} \exp\left(-\frac{2r^2}{R^2}\right) \tag{1}$$

Here, the heat flux absorption coefficient, P, is the power of the laser beam, R acts as radius of the laser beam and r is the distance from the center of the plate to the center of the laser radiation source. After the metal plate is irradiated, the temperature of the radiation increases. Temperature rise is affected by convection and radiation heat transfer. Finite element model for the formation of a laser sheet is shown in figure 5. For the modeling, a circular plate with a radius of 50 mm and

a thickness of 1 mm were modeled in ABAQUS software model.

In order to compare the numerical results with the experimental ones, this paper is attempting to provide identical conditions with the experimental and numerical results. Properties of the steel used in the simulation are as follows.

Table 1: Physical properties of the work- piece

Young's modulus *Gpa*	154
Density kg/m^3	7700
Yield stress Mpa	243
Specific heat $J/kg\,k$	550

In the simulation of the process, three dimensional solid elements of the type DC3D8 which has 8-node tri-linear displacement were used. To be precise, 2 layers of elements through the thickness were generated in the work-piece and the mesh of the work-piece contained 15120 elements. In addition, DFLUX subroutine has been used to apply the heat flux. The analysis is performed in two modes: the first analysis was thermal and then, the deformation analysis of the sheet metal was done by results of thermal analysis.

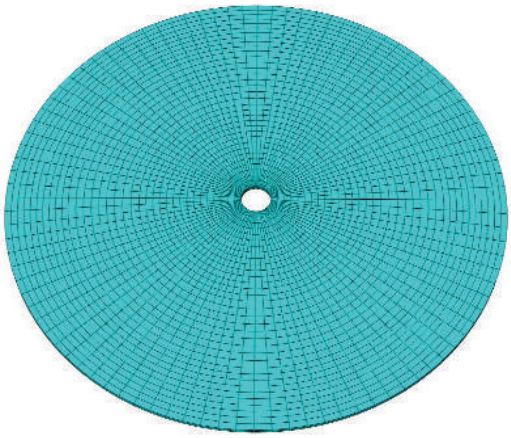

Figure 5: Finite element mesh of sheet

4.0 RESULTS AND DISCUSSION

4.1 Deformation by circular-radial radiation on the sheet

In Figure 6, the result of laser forming a circular blank with circular – radial irradiation paths is shown. As illustrated, the total deformation of the edge in the zero degree path is positive. On the other hand, in the 90- degree path the total deformation of the edge is negative. As such, the values of an edge dislocation in both paths were different and will be discussed below.

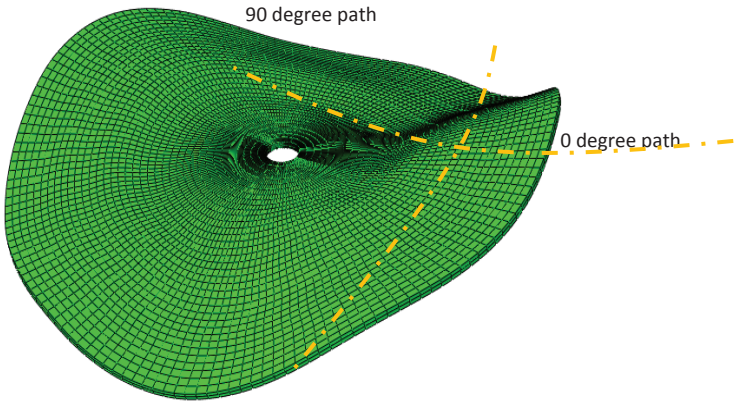

Figure 6: Status of sheet metal forming by circular-radial pattern radiation

4.2 Evaluation of removable edges of sheets forming in circular radial radiation

In Figure7, the status of the edge dislocation and profile of the dome with a circular- radial radiation are shown. As can be seen along both directions, the displacement along the edges in a zero degree direction is positive with the value of around 8 mm. Furthermore, the displacement of the edge along the 90- degree direction is negative and the value is nearly 8 mm.

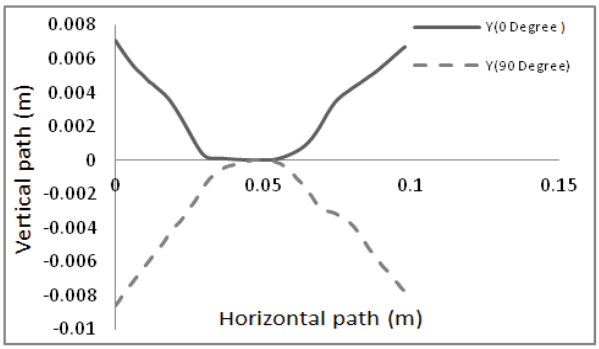

Figure 7: Diagram of the dome-shaped profile with a circular-radial pattern

4.3 Distribution of stress in the laser forming process by circular-radial radiation

Figure 8 shows the effect of von mises stresses and residual stress values on the final geometry of work piece. Residual stresses are those that remain in a solid material after the main causes of the stresses are removed. It is observed that the pattern of residual stresses is somewhat non-uniform and the areas of the plate that are affected by the stress are expanded. They are rooted in large number of radiation beams on the surface of the sheet, the immense variety of possible exposure and the other effective parameters.

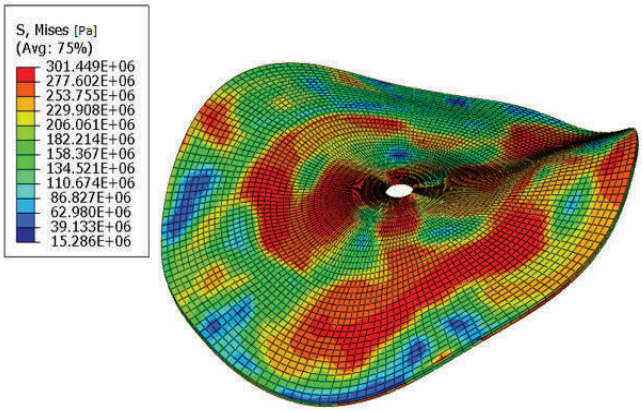

Figure 8: Residual stresses in circular-radial radiation pattern

4.4 Temperature distribution under circular-radial irradiation

In this section, the temperature distribution of the upper and lower surface of sheet metal under laser radiation of circular-radial path is investigated. Using this temperature profile, dominant mechanisms in the laser forming process are found. In figure 9, the temperature

distribution has been studied under radial irradiation. The buckling mechanism has occurred due to the very low thermal gradient between layers of the upper and lower plate by the radial irradiation.

In figure 10, the temperature changes under circular irradiation have been studied. According to figure 10, a small thermal gradient between the upper and lower surfaces have occurred. Therefore, low thermal gradient leads to buckling mechanism in the work-piece.

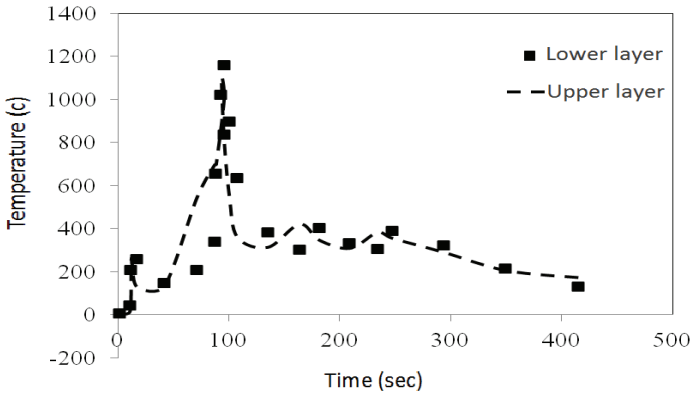

Figure 9: Temperature distribution in the exposure of the upper and lower layers of radial radiation

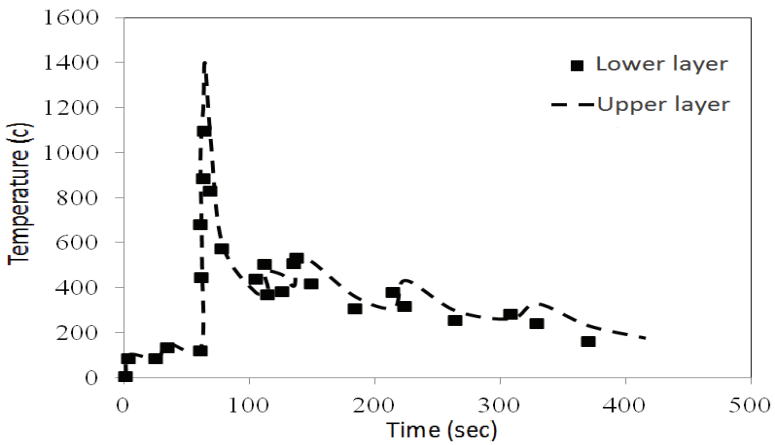

Figure 10: Temperature distribution in the exposure of the upper and lower layers of circular radiation

4.5 Distribution of thick sheet metal with circular-radial radiation

To investigate the formation of dome-shaped pattern by circularradial radiation pattern, increasing the thickness numerically at 9 points along the diameter direction at a zero degree angle is measured.

As it can be seen in Figure 11, value thickening terms are in micrometers. It should be noted that due to the fact that small thickness is increased, the amount of increase will have negligible effects on the nature of the sheet metal forming.

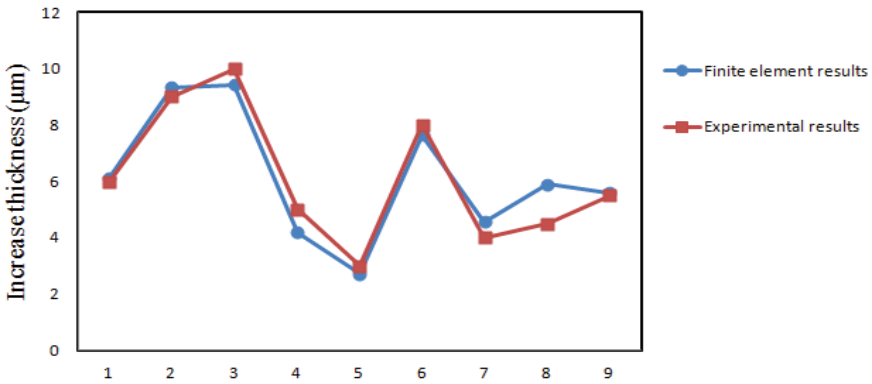

Figure 11: Thickness distribution by circular-radial irradiation

5.0 FORMING A BOWL SHAPE BY SPIRAL EXPOSURE

In continuation of the study about laser forming of bowl-shaped surface in this paper, a new path has been proposed. This path is radiated on sheet metal in terms of spiral pattern as shown in Figure 12. Hence, this path was investigated by the experimental and FEM analysis.

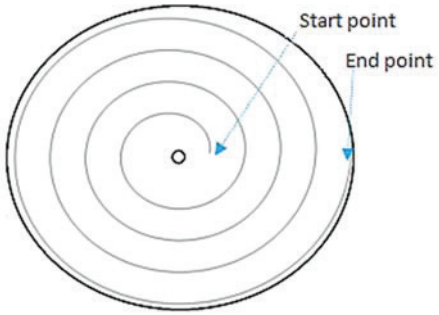

Figure 12: Spiral pattern observed in the study

Figure 13 shows the installation of sheet metal and laser irradiation in the laboratory under a spiral pattern.

Figure 13: Spiral exposure on sheet metal

5.1 Deformation caused by helix radiation on the sheet

Deformation caused by numerical analysis from the spiral pattern is specified in figure 14. Based on the illustration, the displacement of edge along the zero degree direction is positive. Also, displacement of edge along the 90 degree direction is better than the edge displacement by circular-radial pattern and it can be seen that spiral path results in domed-like shape. Of course, the values of edge displacement by circular-radial path and spiral path were different.

It can be noted that, the spiral pattern is better than the circular-radial one in achieving dome shaped forms.

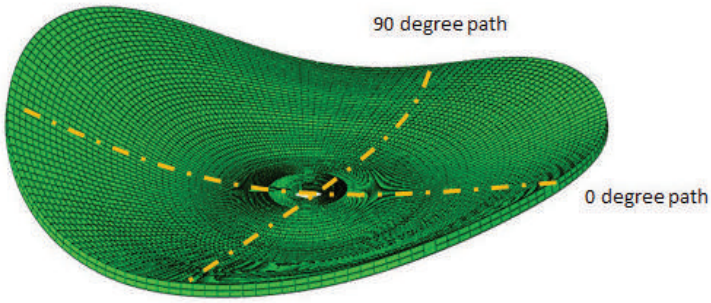

Figure 14: Status of sheet metal by forming a spiral pattern

5.2 The edge symmetry by spiral irradiation

In the following diagram, the status of the dome-shaped profile of edges is shown by spiral irradiation.

In addition, the symmetry of the dome-shaped surface that was formed by spiral pattern is also shown. As it can be seen from Figure 15 along the zero degree and 90 degree direction, the value of edge displacement along the direction of zero degree is positive and it is about 3 mm.

Likewise, the value of edge displacement along the direction of 90 degree is positive. In terms of edge symmetry, formation made by spiral pattern to achieve dome shape is appropriate. Furthermore, forming a bowl shape and motion of the positive edge by spiral radiation pattern is remarkably improved and is better than circular-radial pattern.

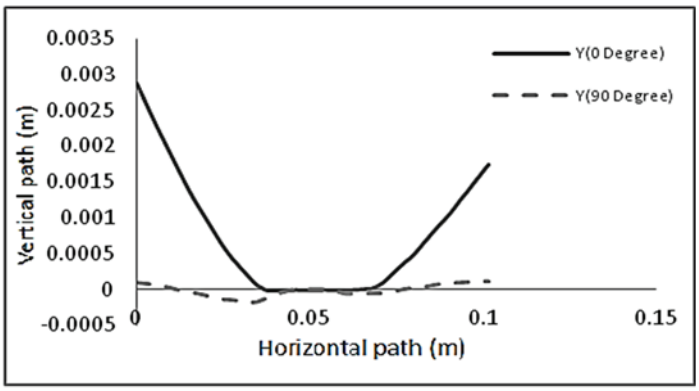

Figure 15: Diagram of the dome-shaped profile with a spiral pattern

5.3 Evaluation of the stress distribution in the forming process of laser in spiral irradiation

Figure 16 shows the effect of the von mises stress and the residual stress values on geometry of work piece. It is observed that the residual stresses are more uniform than the distribution of residual stresses on circular-radial pattern. The reasons are that, firstly, the spiral pattern is not complex compared to circular-radial pattern and secondly, starting points and ending points of spiral radiation patterns are much less than that of circular-radial radiation patterns.

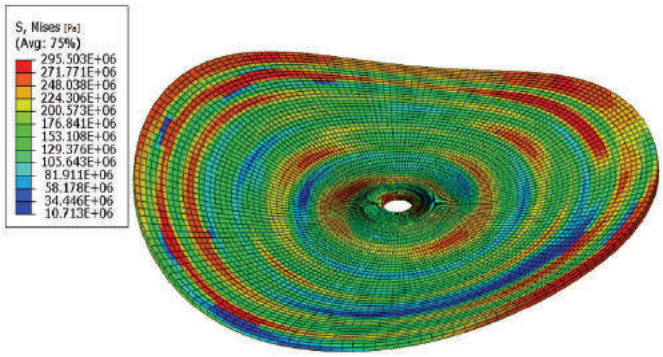

Figure 16: Residual stresses in circular spiral pattern

5.5 Examining the temperature distribution of the spiral beam path

Temperature distribution of the upper and lower surfaces of sheet metal under the spiral irradiation indicated how the process happened in the sheet.

In Figure 17, the status of temperature changes under spiral radiation is investigated. According to Figure 17, the less heat gradient has occurred between upper surface and lower surface showed that the buckling mechanism under spiral radiation has occurred.

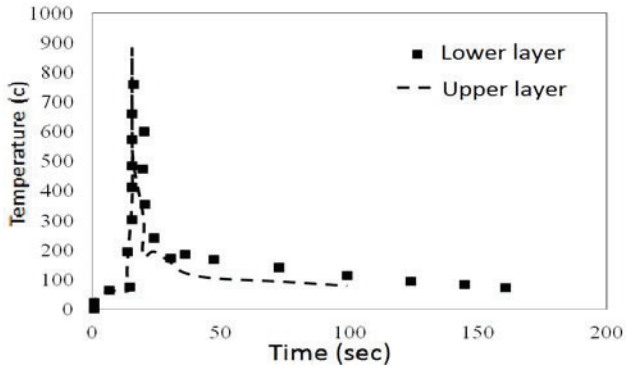

Figure 17: Temperature distribution in the exposure of the upper and lower layers of the spiral radiation

6.0 CONCLUSION

In this paper, the effects of circular-radial radiation to form domeshaped profile/pattern by laser were investigated experimentally and numerically.

In the laser forming process, domed steel parts produced by circularradial pattern have no axial symmetry and the final form produced by circular-radial irradiation pattern along an axis has positive displacement value while the other axis has negative displacement value. In other words, the final shape is saddled-like one.

In the final form, which is irradiated by circular-radial pattern, it does not lead to uniform displacement. Therefore, this irradiating pattern has not been industrially applied. Furthermore, the edges condition of the formed plate has no adequate quality as compared with the spiral pattern.

In a circular-radial radiation pattern, buckling mechanism under circular-radial radiation was created.

In terms of the distribution of residual stresses, due to an immense variety of the circular-radial irradiation and the exposure path parameters, the final form does not have any appropriate conditions. Precisely, residual stress is very high and it has bad effect on micro structure of work-piece.

For the proposed spiral radiation pattern, in terms of shaping sheet metal into a bowl, the symmetry boundary conditions are better than circular-radial radiation patterns.

In terms of the distribution of residual stresses, multiplicity and complexity of the spiral radiation pattern on the metal blank is simpler than circular-radial radiation. Likewise, because of the starting points and end points of laser radiation on work piece that result in an increase in stress on the blank, work piece under spiral irradiation has better forming condition than that under circularradial irradiation. Moreover, stress distribution in work piece under spiral pattern is more uniform than that of circular-radial pattern.

According to the influential parameters of buckling mechanism which rooted in low temperature gradient along the thickness, spiral radiation pattern contributes to thermal buckling mechanism.

REFERENCES

[1] H. C. Jung, "A study on laser forming processes with finite element analysis", PhD thesis in Mechanical Engineering at the University of Canterbury Christchurch, New Zealand, pp. 27-31, April, 2006.

[2] F. Vollertson, "Mechanisms and models for laser forming", Proceedings of Laser Assisted Net shape Engineering Conference, pp. 345-359, 1994.

[3] J. Kim and S. J. Na, "Development of irradiation strategies for free curve laser forming", *Opt. Laser. Technol.* Vol. 35, pp. 605-611, 2003.

[4] J. Kim and S. J. Na, "3D laser-forming strategies for sheet metal by geometrical information", *Opt. Laser. Technol*. Vol. 41, pp. 843-852, 2009.

[5] K. G. Watkins, S. P. Edwardson, J. Magge and G. Dearden, "Laser forming of aerospace alloys", Conference, Washington, US, 2001.

[6] S. P. Edwardson , G. Dearden, P. Frenchl and K. G. Watkins , "Laser forming of metal laminate composite materials", ICALEO2003 Laser institute of Orlando, pp. 225-339, 2003.

[7] S. P. Edwardson, K. G. Watkins, G. Dearden, P. French and J. Magee, "Strain gauge analysis of laser forming", *Journal of Laser Applications* ,Vol. 15, pp. 225- 232, 2003.

[8] Edwardson, S. P., Moore,S. A., Abed, E., McBride ., Dearden, G., Jones, J. DC., Watkins ICALEO 2004 Conference Laser Institute of Orlando, pp. 682-693, 2004.

[9] S. P. Edwardson, E. Abed, P. French, G. Dearden, K. G. Watkins and R. McBride, "Development towards controlled three-dimensional laser forming of continuous surfaces", *J Laser Appl, pp*.17, 2005.

[10] C. Liu and Y. L. Yao, "Fem-based process design for laser forming of double curved shapes". *Journal of Manufacturing Process*, Vol. 7(2), pp. 109–121, 2005.

[11] K.G. Watkins, S.P. Edwardson, J. Magee, G. Dearden, P. French, R.L. Cook, et al. "Laser forming of aerospace alloys", Society of Automotive Engineers; (2001).

[12] T. Hennige, "Development of irradiation strategies for 3D-laser forming", *Journal of Materials Processing Technology*, Vol. 103, pp. 102-108, 2000.

[13] H. Shen and Z. Yao, "Study on mechanical properties after laser forming", *Opt. Lasers. Eng.* Vol. 47, pp. 111-117, 2009.

[14] S. S. Chakraborty, V. Racherla, and A. K. Nath, "Parametric study on bending and thickening in laser forming of a bowl shaped surface", *Opt. Lasers. Eng.* Vol. 50, pp. 1548-1558, 2012.

[15] K. Masubushi and W.H. Luebke, "Laser forming of plates for ship construction", submitted from Massachusetts Institute of Technology, pp. 189- 196, 1995.

[16] ABAQUS software, 2012, Version 6.0, ABAQUS Inc., USA.

FAILURE MODE AND EFFECTS ANALYSIS OF SHIP SYSTEMS USING AN INTEGRATED DEMPSTER SHAFER THEORY AND ELECTRE METHOD

I, Emovon

School of Marine Science and Technology,
Newcastle University, Newcastle upon Tyne, NE1 7RU, UK

Email: i.emovon@newcastle.ac.uk

ABSTRACT: Failure Mode and Effects Analysis (FMEA) is a risk analysis tool which is used to define, identify, and eliminate known and/or potential failures from a system. The task is generally performed by a team of experts. Each of the team of experts can express diverse opinions in rating of failure modes of systems which may be in the form of precise data and imprecise distribution ratings. However the RPN of FMEA is incapable of using these various forms of information in the prioritisation of risk of failure modes. This is one of the main limitations of FMEA. Furthermore the technique is limited to the use of three decision criteria thereby excluding other important decision criteria such as production loss in prioritising risk. To address these problems a novel FMEA tool was proposed which combines Dempster Shafer Theory with the ELECTRE method to provide a more efficient failure mode prioritisation method. The Dempster Shafer Theory was used in aggregating different failure mode ratings from experts and the ELECTRE method was applied in the ranking of failure modes. The applicability of the proposed technique was demonstrated with a case study of a marine diesel engine. The results showed that the proposed method could be applied in addressing risk prioritisation problem more efficiently than the FMEA and its variants.

KEYWORDS: *Dempster Shafer Theory, ELECTRE method, FMEA, ship system.*

1.0 INTRODUCTION

Ship system operation requires high levels of safety and reliability and these can only be accomplished by having an effective maintenance system in place. Basically, maintenance system consists of three major elements that must perform optimally in order to attain high level of the ship system safety and reliability. The three main elements of maintenance management system are risk assessment, maintenance strategy selection and maintenance task interval determination. The focus in this paper is the risk assessment component and it is very central to the operation and maintenance of ship system because the maintenance task to be performed on each of the equipment item of the system is a function of the assessed risk. Failure Mode Effect and

Analysis (FMEA) is one of the most popular and powerful tools for assessing risk of ship systems [1, 2]. The technique was first proposed by NASA in the 1960s as a tool to identify and eliminate complex system failures in order for the system to achieve desirable levels of safety and reliability [3]. In analysing risk, FMEA puts into consideration how equipment items fail, the effect of an individual failure on the entire system and possible means of failure detection. Traditionally, FMEA uses Risk Priority Number (RPN) in evaluating and prioritising risk. FMEA is defined as the product of three risk criteria; probability of Occurrence (O), resulting level of Severity (S) and the inverse of the ability to Detect (D) the failure before it occurs. In assigning values to these three risk decision criteria an ordinal scale of 1-10 is generally applied by most researchers and industries [1,4,5]. Despite the popularity of the FMEA it has some limitations which has affected the efficiency of the tool in prioritising the risk of failure modes of most complex system of which the ship system is not excluded. Some of these limitations are: (1) the inability of the tool to utilise more than three decision criteria in prioritising risk of failure mode (2) the inability of the tool to consider the relative importance of decision criteria in the risk decision making process (3) the inability of the technique to utilise imprecise information from experts and (4) the questionable and debatable mathematical formula use in aggregating risk criteria[4, 6].

To overcome the limitations of the traditional FMEA, different techniques based on the Multi-Criteria Decision Making (MCDM) have been developed in literature. Braglia [7] presents a technique based on Analytical Hierarchy Process (AHP). The AHP is used as an alternative to the RPN in aggregating four risk criteria; O, S, D and expected cost, for the prioritisation of causes of failure for an Italian refrigerator manufacturing firm. Zammori and Gabbrielli [8] propose Analytical Network Process (ANP) approach for prioritising failures in FMEA system. The authors consider three risk criteria, O, S and D in prioritising risk of failure mode. The use of the ANP allows the interrelationship between risk criteria to be considered in the decision making process. Maheswaran and Loganathan [9] present a methodology based on Preference Ranking Organisation Method for Enrichment Evaluation (PROMETHEE as an alternative for the RPN used in the traditional FMEA, for ranking risk of failure modes of a boiler system.

All of the aforementioned papers have improved the efficiency of the traditional FMEA system, as it is possible to utilise more than three decision criteria in the ranking of risk of failure mode. Furthermore, the risk of different failure modes is better distinguished with various MCDM tools than the RPN of the FMEA system. However, the MCDM

tools applied increases the evaluation process complexity as the number of decision criteria increases. Furthermore, the techniques only allow the use of precise information from the experts in the decision making process whereas in real life situation the data may be precise or imprecise or a combination of both.

There is a need to develop a more systematic approach for prioritising risk of failure modes of ship systems. In order to overcome the challenges of the traditional FMEA and its variants in literature this study proposed a novel FMEA tool which combined Dempster Shafer Theory with the ELECTRE method. The Dempster Shafer theory technique was applied in aggregating different assessment which may be precise or imprecise from the experts that make up the FMEA team. The ELECTRE method is applied in the ranking of risk of failure modes of the ship system.

2.0 METHODOLOGY

2.1 Dempster Shafer Combination theory

The origin of Dempster Shafer Theory (DST) can be traced to Dempster [10] who develops the theory of upper and lower probabilities and Shafer [11] who further improves on the technique. The tool has been used in different fields in modelling and aggregating empirical evidence in individual's mind. DST has been integrated with the RCM logic tree in the selection of optimum maintenance strategy for different complex systems [12]. The technique has been applied in solving data inconsistency in reliability decision problem. Due to its remarkable success in addressing problem of data uncertainty in different domain, it is combined with the ELECTRE method in this paper to address the problem of data imprecision in risk prioritisation problem of ship system. The basics of the DST are presented in this section and are as follows [12, 13]:

Let be a finite set of mutually exclusive and exhaustive hypothesis. The set generally refers to the frame of discernment. A function m(Y) is defined as the Basic Belief Assignment (BBA) if the following conditions are satisfied.

$$m{:}2 \rightarrow [0,1]$$

$$m(\emptyset) = 0$$

$$\sum_{A \subseteq} m(Y) = 1$$

A new BBA, $m(C)$, can be formed from the combination of two BBAs $m_1(Y)$ and $m_2(Z)$ (Y and Z belong to set ⊚), as follows:

$$m(C) = m_1(Y) \oplus m_2(Z) = \begin{cases} \dfrac{\sum_{Y \cap Z = y} m_1(Y) m_2(Z)}{1 - k} & y \neq \emptyset \\ 0 & y = \emptyset \end{cases} \quad (1)$$

But

$$k = \sum_{Y \cap Z = \emptyset} m_1(Y) m_2(Z)$$

which denotes the degree of conflict between two bodies of evidence, Y and Z.

The application of this combination rule for aggregating different opinions of experts as it concerns risk of failure modes prioritisation is described as follows [4, 6].

⊚ = [1,2,3,4,5,6,7,8,9,10] i.e. ordinal scale 1 to 10 rating for risk decision criteria; $m(Y)$ represents the probability rating given by experts which support proposition Y. Y is the specific value from the set ⊚ to a decision criterion.

Example: The criterion D, rated by two experts for failure mode 1 in Table 3 is used to demonstrate the Dempster Shafer Theory combination rule application. From Table 3, the risk rating of criterion D, by expert 1 is 4:70% and 3:30% and that of expert 2 is 4:40% and 5:60%.

The discernment frame for this problem is formed as = [3, 4, 5] and the BBAs is as follows:

$m_1(3) = 0.3$, $m_1(4) = 0.7$, $m_2(4) = 0.4$ and $m_2(5) = 0.6$

$$m_{12}(3) = m_1(Y) \oplus m_2(Z) = \frac{\sum_{Y \cap Z=3} m_1(Y) m_2(Z)}{1 - \sum_{Y \cap Z=\emptyset} m_1(Y) m_2(Z)} = \frac{0}{1 - 0.12 + 0.18 + 0.42}$$

$$= 0$$

$$m_{12}(4) = m_1(Y) \oplus m_2(Z) = \frac{\sum_{Y \cap Z=4} m_1(Y) m_2(Z)}{1 - \sum_{Y \cap Z=\emptyset} m_1(Y) m_2(Z)} = \frac{0.7 \times 0.4}{1 - 0.12 + 0.18 + 0.42}$$

$$= 1$$

$$m_{12}(5) = m_1(Y) \oplus m_2(Z) = \frac{\sum_{Y \cap Z=3} m_1(Y) m_2(Z)}{1 - \sum_{Y \cap Z=\emptyset} m_1(Y) m_2(Z)} = \frac{0}{1 - 0.12 + 0.18 + 0.42}$$

$$= 0$$

For this problem, expert 1 and 2 combine rating for criterion, D,

$= 3 \times 0 + 4 \times 1 + 5 \times 0 = 4$

2.2 ELECTRE METHOD

The ELECTRE method development and origin can be traced to Roy and Vincke [14] and the acronym, ELECTRE, stand for, Elimination and Et Choice Translating Reality. The basic concept of the multi criteria technique is based on paired comparisons of alternatives with reference to some certain decision criteria. The technique has been used by different researchers in solving multi-criteria decision problems in different domain. Shanian, Milani, Carson and Abeyaratne [15] utilise the technique in solving a material selection problem and Sevkli [16] integrated ELECTRE with a fuzzy logic technique in addressing a supplier selection problem. The method is applied in this paper, to address the challenge of risk prioritisation of ship system. The steps involved in the ELECTRE method are as follows [17]:

Step 1: Decision matrix formation: ELECTRE method process begins with the construction of a decision matrix with alternatives, j with respect to criteria, i. Since the Dempster Shafer theory is integrated with the method, the evaluated data from the Dempster Shafer combination rule is used to form the decision matrix. An example of such a decision matrix with element xij is presented in Table 1.

Table 1 : Inspection interval alternatives decision table

Failure modes (Aj)	Decision criteria (Bi)		
	O	S	D
A_1	x_{11}	x_{12}	x_{13}
A_2	x_{21}	x_{22}	x_{23}
A_3	x_{31}	x_{32}	x_{33}
…	…	…	…
A_m	x_{m1}	x_{m2}	x_{m3}

Step 2: Normalisation of the decision matrix: The normalisation of the decision matrix xij is performed as follows:

$$p_{ij} = \frac{x_{ij}}{\sqrt{\sum_{j=1}^{m} x_{ij}}}, i = 1,2 \ldots, n; j = 1, \ldots, m \tag{2}$$

Where pij is the normalised decision matrix

Step 3: Weighted normalised matrix formation:
The weighted normalised matrix v_{ij} is obtained by multiplying decision criteria weights, w_j, with the normalised decision matrix and is presented as follows:

$$v_{ij} = w_j p_{ij}, \quad i = 1, \ldots, n; \quad j = 1, \ldots, m \tag{3}$$

Step 4: Concordance interval matrix formation: Given a pair of failure modes, (alternatives) A_j and A_k, the concordance index $c_1(j, k)$ can be estimated as the sum of all weights for those decision criteria where the weighted normalised score of A_j is greater than or equal to A_k, as follows:

$$c_i(j,k) = \sum_{w_i(j) \geq w_i(k) \neq k} w_i, \quad j, k = 1, \ldots, j \tag{4}$$

Where $v_i(j)$ and $v_i(k)$ are the weighted normalised scores of the j_{th} and k_{th} alternatives respectively. The concordance evaluation results are then used to form the concordance matrix as follows:

$$C_I = \begin{bmatrix} - & c_I(1,2) & \dots & c_I(1,m) \\ c_I(2,1) & - & \dots & c_I(2,m) \\ \vdots & \vdots & \ddots & \vdots \\ c_I(m,1) & c_I(m,2) & \dots & - \end{bmatrix} \tag{5}$$

Step 4: Discordance interval matrix formation: The discordance index $d_1(j, k)$, is evaluated as:

$$d_I(j,k) = \begin{cases} 0, & if \quad v_t(j) \geq v_t(k) \quad t = 1,2,\dots,n \\ \dfrac{\max\limits_{v_t(k)>v_t(j)} [v_t(k) - v_t(j)]}{\max\limits_{t=1,\dots,n} [|v_t(k) - v_t(j)|]}, & otherwise \qquad j,k = 1,2,\dots,m.\ j \neq k \end{cases} \tag{6}$$

The information obtained from the discordance index is then used to form the discordance matrix presented as follows:

$$D_I = \begin{bmatrix} - & d_I(1,2) & \dots & d_I(1,m) \\ d_I(2,1) & - & \dots & d_I(2,m) \\ \vdots & \vdots & \ddots & \vdots \\ d_I(m,1) & d_I(m,2) & \dots & - \end{bmatrix} \tag{7}$$

Step 5: Determination of the performance index:
Two indices, net superior values, C_a, and net inferior values, D_a use for measuring performance of failure modes (alternatives) are evaluated respectively as follows:

$$C_a = \sum_{k=1}^{m} c_I(j,k) - \sum_{\substack{j=1 \\ \neq k}}^{m} c_I(k,j) \quad j \tag{8}$$

$$D_a - \sum_{k=1}^{m} d_I(j,k) - \sum_{\substack{j=1 \\ \neq k}}^{m} d_I(k,j) \quad j \tag{9}$$

The two performance indices for prioritising failure modes will yield two rankings. The two rankings can either be applied individually or both can be averaged to generate overall ranking.

3.0 CASE STUDY

In this section, the marine diesel engine is considered to demonstrate the suitability of the integrated Dempster Shafer theory and ELECTRE method. The marine diesel engine was chosen because it is one of the key ship machinery systems as it provides the power for the propulsion of the entire ship system. In addition, the marine main engine accounts for over 45 percent of the total compensation for fault accident claims of the entire ship system according to the survey carried out by a Swiss shipping insurance Company [18]. It is then obvious that the marine diesel engine is central to the operation, of not only the machinery systems, but of the entire ship system powered by this type of engine. A total of 23 failure modes were identified in bits from combinations of different sources such as literatures, data logged records and experts' opinions. Causes of failure, together with effects for each of the failure mode are presented in Table 2.

Table 2: FMEA for marine diesel engine [2, 5, 20-24]

S/N	Failure modes	Failure cause	Local effects	Global effects
1	Hole in the piston crown	Dripping of fuel valve	Escape of combustion gas into the crankcase	Reduced engine performance, engine damage and stoppage
2	Piston ring scuffing	Lack of lubrication, liner roundness fault	Oil smoke from exhaust, blow-by	Reduced engine performance
3	Piston ring cracked	Excessive gap pressure, worn-out ring groove	Oil smoke from exhaust, loss of power	Reduced engine performance
4	Piston ring /groove side face wear	Liquid fuel degrading lubricant in ring grooves	Loss of power	Reduced engine performance, engine stop
5	Piston ring stuck in grooves	Insufficient clearance during installation, deposits	Excessive clearance, fire blow	Reduce engine output, Stop engine
---	---	---	---	---
23	Crankcase relief valve inoperable	Not seated properly	Allow air escape into crankcase	Reduce engine performance, explosion probable

In this paper, it is assumed that the FMEA team consists of two experts with equal expertise. Each of the expert ranks each of the 23 failure modes based on 3 decision criteria; O, S and D on an ordinal scale of 1-10. Table 3 represents the failure modes rating by two experts of which

some are precise and others are imprecise rating. Because the proposed methodology utilised decision criteria weights in the decision making process, these weights were evaluated using the Analytical Hierarchy Process (AHP) see[19] for description of the AHP. The weights obtained for O, S and D, using AHP are 0.4, 0.4 and 0.2 respectively.

Table 3: Expert 1 and 2 imprecise decision criteria rating

Failure modes	Risk criteria rating						
	Expert 1				Expert 2		
	O	S	D		O	S	D
1	7:30%	3	4:70%		7:30%	4	4:40%
	8:70%		3:30%		8:70%		5:60%
2	7	6:50%	8		6	6	7
		5:50%					
3	5	6	5: 100%		5	8	6
4	7	3	3: 80%		7:70%	4	4
			2: 20%		6:30%		
5	7: 100%	6	5: 50%		6	7	5:80%
			4:50%				6:20%
…	…	…	…		...	...	...
23	7:80%	2	9:90%		7:60%	3	9
	6:20%		8:10%		5:40%		

The Dempster Shafer combination technique was applied to the imprecise ratings of decision criteria by expert 1 and 2 in Table 3 to obtain aggregated ratings. The aggregated ratings were used to form a decision matrix (refer to Table 4) which was then used as input data into the ELECTRE tool for the ranking of failure modes.

Table 4: Decision matrix

Failure mode	O	S	D
1	7.84	3.5	4
2	6.5	5.89	5.5
3	5	7	5.5
4	6.95	3.5	3
5	6.5	6.5	5
…	…	…	…
23	7	2.5	8.99

In applying the ELECTRE method to rank risk of failure modes, the decision matrix in Table 4 was normalised using Eq. 2. Then, weighted normalised decision matrix was obtained which is a product of the normalised decision matrix and the weights of the decision criteria. The formation of the concordance interval matrix and the discordance interval matrix using Eq. 4 and 6 respectively was then performed. Based on the concordance matrix and the discordance matrix, the net superior, Ca, and net inferior, Da, values of the different failure modes were calculated using Eq. 8 and 9 and the results are presented in Table 5. Finally, the different failure modes were ranked using their net superior and inferior values and the rankings generated are also presented in Table 5. The performance of the different failure modes could be determined by applying either the net superior index or net inferior index or an average of both. For the net superior index, the greater the value the higher the risk possess by the failure mode. In applying the net inferior value index in determining performance of the different failure modes, the lower the net inferior value the higher the risk the failure mode possess to the system.

From Table 5, the two ranking indices produce quite dissimilar rankings for all the 23 failure modes. The net superior index ranked failure mode 10 in the first position and as such was the most critical failure mode of the marine diesel engine. The net inferior index ranked the same failure mode in the second position.

Table 5: ELECTRE II ranking of failure modes

Failure modes	Ca	Rank	Da	Rank
1	-0.4000	14	0.9508	14
2	1.6000	9	-9.4283	5
3	2.4000	7	-7.8602	7
4	-8.6000	23	12.9899	20
5	4.2000	6	-13.3375	3
6	0.2000	13	-5.1153	10
7	-6.6000	19	17.5393	23
8	7.2000	3	-17.5729	1
9	2.4000	7	-11.5548	4
10	11.2000	1	-16.3682	2
11	-3.0000	16	12.7088	19
12	-7.2000	21	14.2723	21
13	-1.4000	15	9.1666	16

14	1.2000	10	-3.8566	12
15	5.6000	5	-5.8254	8
16	0.6000	11	4.0543	15
17	0.2000	12	0.6266	13
18	8.4000	2	-5.3497	9
19	-5.2000	18	10.3197	17
20	6.4000	4	-9.0052	6
21	-6.8000	20	12.4422	18
22	-8.4000	22	14.3962	22
23	-4.0000	17	-4.1927	11

For the net superior index failure mode 4 ranked in the last position, indicating the least critical failure mode of the marine diesel engine while failure mode 7 ranked in the last position by the inferior index. The net superior index is commonly used as the optimum ranking technique. However some researchers have combined the two performance indices to obtain overall ranking of alternatives. The net superior index is recommended for risk prioritisation of ship system because it generates the same results as the PROMETHEE technique applied by Maheswaran and Loganathan [9]. This is illustrated in section 3.1.2.

From Table 5, the two ranking indices produce quite dissimilar rankings for all the 23 failure modes. The net superior index ranked failure mode 10 in the first position and as such was the most critical failure mode of the marine diesel engine. The net inferior index ranked the same failure mode in the second position. For the net superior index failure mode 4 ranked in the last position, indicating the least critical failure mode of the marine diesel engine while failure mode 7 ranked in the last position by the inferior index. The net superior index is commonly used as the optimum ranking technique. However some researchers have combined the two performance indices to obtain overall ranking of alternatives. The net superior index is recommended for risk prioritisation of ship system because it generates the same results as the PROMETHEE technique applied by Maheswaran and Loganathan [9]. This is illustrated in section 3.1.2.

3.1 Comparison of ELECTRE method with other methods

3.1.1 Comparison of the ELECTRE method with the conventional FMEA

As stated in the introduction section, one of the challenges of the conventional FMEA, is its inability to utilise imprecise information from experts. To overcome this challenge and for unbiased comparison with the proposed technique, the aggregated data shown in Table 4 was also used as an input into the conventional FMEA. The ranking of risk of failure modes produced by the two methods are shown in Figure 1.

From Figure 1, it is obvious that the rankings produced by the conventional FMEA differ considerably from that of the ELECTRE method as the majority of the failure modes are ranked differently. The variation is as a result of the limitations of the conventional FMEA which are as follows:

- The inability of the FMEA to consider decision criteria weights in the decision making process whereas in the ELECTRE methodology, the decision criteria weights are put into consideration.
- The multiplication of O, S and D in evaluating RPN of the conventional FMEA is not rational.

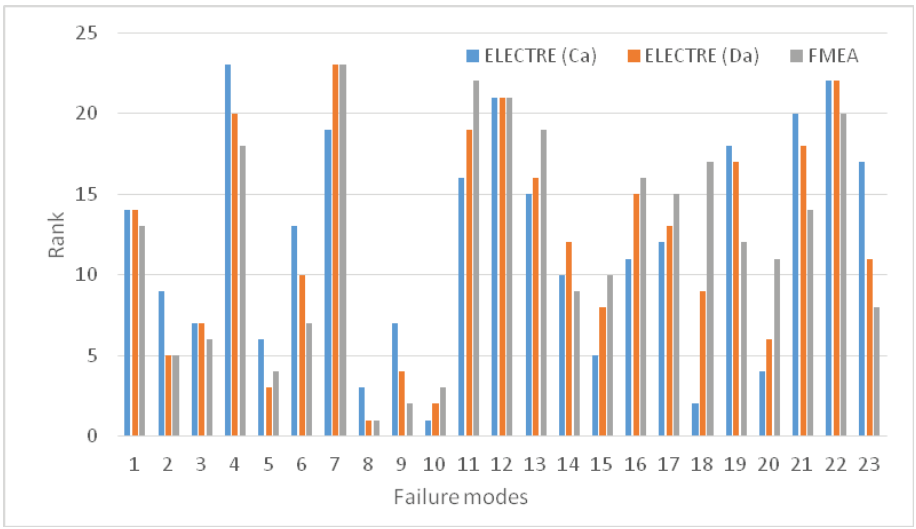

Figure 1: Comparison with conventional FMEA

These are some of the reasons why alternative approaches such as MCDM based methodology is recommended in the literature [7, 9]. The proposed methodology discussed in this paper overcomes all of these limitations of the conventional FMEA.

3.1.2 Comparison of the ELECTRE method with PROMETHEE method

In order to validate the novel technique, it was compared with the PROMETHEE method applied by Maheswaran and Loganathan [9]. Maheswaran and Loganathan [9]do not consider imprecise information from experts but use crisp values in the decision making process. However, in order to allow the use of both precise and imprecise information from experts, the data in Table 5 evaluated with the Dempster Shafer theory's combination technique was used as an input in the PROMETHEE methodology. The results of a comparative analysis of both the ELECTREE and the PROMETHEE technique are presented in Figure 2.

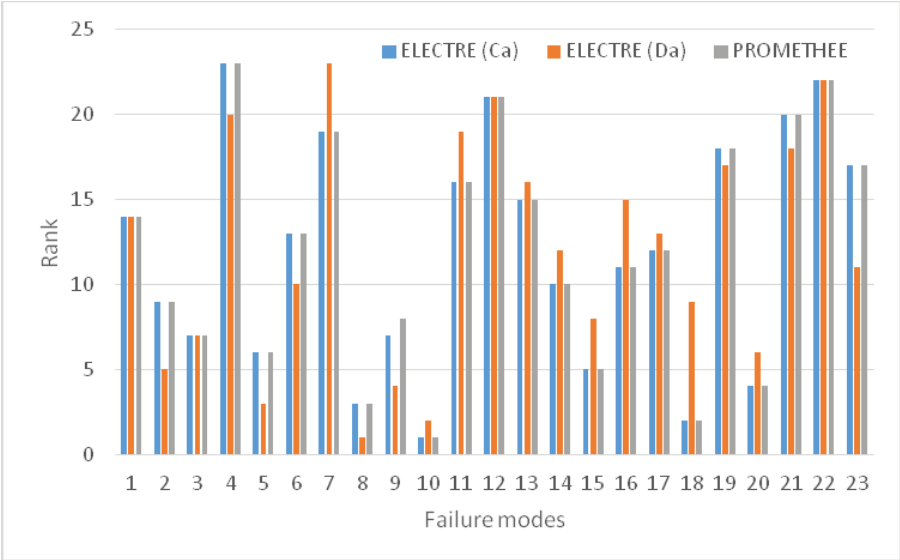

Figure 2: Comparison with PROMETHEE method

From Figure 2, the ELECTRE method (net superior (Ca)) and the PROMETHEE produces the same rankings for the 23 failure modes. However the ELECTRE method (net inferior (Da)) produces different ranking for most of the failure modes. On this basis, the ELECTRE method (net superior (Ca)) is recommended for prioritising risk of failure modes of ship systems. Although, Ca, produces the same results with that of the PROMETHEE technique applied by Maheswaran and Loganathan [9], it is easy to apply irrespective of the number of decision criteria utilised in prioritising risk of failure mode as opposed to PROMETHEE whose evaluation process complexity increases as the number of decision criteria increases. Furthermore, the ELECTRE method does not require the maintenance practitioners to determine

the preference function for each of the decision criteria which is one of the drawbacks of the PROMETHEE technique. The PROMETHEE technique as applied by Maheswaran and Loganathan [9] for risk of failure mode prioritisation only considers precise information from experts and in most real life situation, information may be precise and imprecise. The integration of the Dempster Shafer combination technique with the ELECTRE method and PROMETHEE method make it possible for both techniques to utilise both precise and imprecise data from experts.

4.0 CONCLUSION

The purpose of this paper was to develop a systematic approach for risk prioritisation which avoids the limitations of the traditional FMEA and its variant in order for risk to be prioritised more effectively. To achieve this objective a novel FMEA tool which combines the Dempster Shafer Theory with the ELECTRE method is presented. The Dempster Shafer Theory is used to aggregate imprecise failures modes rating from experts while the ELECTRE method is used in the ranking of failure modes. In demonstrating the applicability and validity of the proposed method, a case study of marine diesel engine is applied. The results of the case study analysis reveal the following:

- The proposed method distinguishes failure mode from each other than the traditional FMEA approach whilst avoiding the limitations of the traditional FMEA such as inability to utilise imprecise information from experts.
- The proposed method produces almost completely the same results as that of the PROMETHEE technique used by Maheswaran and Loganathan [9] thereby validating the proposed approach.
- The proposed technique is easy to apply irrespective of number of decision criteria used in prioritising risk of failure mode unlike the PROMETHEE technique whose analysis difficulty increases as the number of decision criteria increases.
- The proposed technique does not require maintenance practitioners to define preference function for each decision criteria which is an additional burden created by PROMETHEE approach.

In conclusion, it is evident from this research that the proposed method is capable of solving risk prioritisation problem more effectively than the traditional FMEA approach and its variants. Further work can be performed by incorporating other decision criteria such as environmental impact and expected revenue into the risk prioritisation process.

REFERENCES

[1] A. Pillay, and J. Wang, "Modified failure mode and effects analysis using approximate reasoning," Reliability Engineering and System Safety, vol. 79, no. 1, pp. 69-85, 2003.

[2] I. Emovon, R. A. Norman, and A. J. Murphy, "A new Tool for Prioritising the Risk of Failure Modes for Marine Machinery Systems."In: Proceeding of the 33rd International conference on ocean, offshore and Artic engineering OMAE14. American Society of Mechanical Engineers, California, United States, 2014.

[3] Y. Du, H. Mo, X. Deng, R. Sadiq, and Y. Deng, "A new method in failure mode and effects analysis based on evidential reasoning," International Journal of System Assurance Engineering and Management, vol. 5, no. 1, pp. 1-10, 2014.

[4] J. Yang, H.-Z. Huang, L.-P. He, S.-P. Zhu, and D. Wen, "Risk evaluation in failure mode and effects analysis of aircraft turbine rotor blades using Dempster–Shafer evidence theory under uncertainty," Engineering Failure Analysis, vol. 18, no. 8, pp. 2084- 2092, 2011.

[5] K. Cicek, and M. Celik, "Application of failure modes and effects analysis to main engine crankcase explosion failure on-board ship," Safety Science, vol. 51, no. 1, pp. 6-10, 2013.

[6] X. Su, Y. Deng, S. Mahadevan, and Q. Bao, "An improved method for risk evaluation in failure modes and effects analysis of aircraft engine rotor blades," Engineering Failure Analysis, vol. 26, no. 0, pp. 164-174, 2012.

[7] M. Braglia, "MAFMA: Multi-attribute failure mode analysis," International Journal of Quality and Reliability Management, vol. 17, no. 9, pp. 1017-1034., 2000.

[8] F. Zammori, and R. Gabbrielli, "ANP/RPN: A multi criteria evaluation of the risk priority number," Quality and Reliability Engineering International, vol. 28, no. 1, pp. 85-104, 2012.

[9] K. Maheswaran, and T. Loganathan, "A Novel Approach for Prioritisation of Failure modes in FMEA using MCDM," International Journal of Engineering Research and Application, vol. 3, no. 4, pp. 733-739, 2013.

[10] A. P. Dempster, "Upper and lower probabilities induced by a multivalued mapping," The annals of mathematical statistics, pp. 325-339, 1967.

[11] G. Shafer, "Mathematical theory of evidence.," Princeton University, 1976.

[12] U. K. Rakowsky, and U. Gocht, "Reasoning in reliability-centred maintenance based on a Dempster—Shafer approach," Proceedings of the Institution of Mechanical Engineers, Part O: Journal of Risk and Reliability, vol. 222, no. 4, pp. 605-612, 2008.

[13] D. D. Wu, "Supplier selection in a fuzzy group setting: A method using

grey related analysis and Dempster–Shafer theory," Expert Systems with Applications, vol. 36, no. 5, pp. 8892-8899, 2009.

[14] B. Roy, and P. Vincke, "Multicriteria analysis: survey and new directions," European Journal of Operational Research, vol. 8, no. 3, pp. 207-218, 1981.

[15] A. Shanian, A. S. Milani, C. Carson, and R. C. Abeyaratne, "A new application of ELECTRE III and revised Simos' procedure for group material selection under weighting uncertainty," Knowledge-Based Systems, vol. 21, no. 7, pp. 709-720, 2008.

[16] M. Sevkli, "An application of the fuzzy ELECTRE method for supplier selection," International Journal of Production Research, vol. 48, no. 12, pp. 3393-3405, 2010.

[17] L. Anojkumar, M. Ilangkumaran, and V. Sasirekha, "Comparative analysis of MCDM methods for pipe material selection in sugar industry," Expert Systems with Applications, vol. 41, no. 6, pp. 2964- 2980, 2014.

[18] C. Dong, C. Yuan, Z. Liu, and X. Yan, "Marine Propulsion System Reliability Research Based on Fault Tree Analysis," Advanced Shipping and Ocean Engineering, vol. 2, no. 1, pp. 27-33, 2013.

[19] I. Emovon, R. A. Norman, and A. J. Murphy, "Hybrid MCDM based methodology for selecting the optimum maintenance strategy for ship machinery systems," Journal of Intelligent Manufacturing, pp. 1-13, 2015.

[20] K. Cicek, H. H. Turan, Y. I. Topcu, and M. N. Searslan, "Risk-based preventive maintenance planning using Failure Mode and Effect Analysis (FMEA) for marine engine systems."

[21] America Bureau of Shipping, "Guidance note on Reliability-Centered Maintence," America Bureau of Shipping, 2004.

[22] A. Bejger, "An analysis of chosen engine failures of the "Seismic Research" type ship," Journal of Polish CIMAC, vol. 6, no. 2, pp. 9-14, 2011.

[23] C. Dunford, "Crankshaft purpose, design and modes of failure," CSL Technical focus, no. 2, pp. 1-5, 2011.

[24] A. J. Mokashi, J. Wang, and A. K. Vermar, "A study of reliabilitycentred maintenance in maritime operations," Marine Policy, vol. 26, no. 5, pp. 325-335, 2002.

WASTEWATER TREATMENT BY ELECTRO-OXIDATION PROCESS WITH TiO_2

Q.J., Rasheed[1], F., Ghanim[2] and T.A., Abdullah[3]

[1]Production Engineering & Metallurgy Department,
[2, 3]Applied Science Department,
University of Technology, Baghdad, Iraq.

Email: *2fanar_ganem@yahoo.com

ABSTRACT: The environment of wastewater containing toxic organic compounds by the industrial community has the environment of wastewater containing toxic organic compounds by the industrial community has increased significantly in the recent past. So, the treatment of such wastes generated from the industries is considered necessary. Untreated wastewater, if allowed to accumulate will result in the decomposition of organic material that leads to the production of toxic gases. For wastewater, the objective is to remove or reduce the concentration of organic and inorganic compounds. Some of the constituents and compounds present in wastewater lead to serious problem to the environment. This study presents the treatment of petroleum wastewater using nano scale TiO_2 in the presence of electro-oxidation process. TiO_2 physio-chemical characterization of sol-gel method analyzed using Ultraviolet light (which is an electromagnetic radiation), Scanning Electron Microgram (SEM), Fourier Transform Infrared Spectroscopy (FTIR) and X-ray Diffraction (XRD). The influence of TiO_2 dosage and initial pH on % COD reduction was studied. The results indicated that using TiO_2 in combination with electrocoagulation at a dosage of 0.15 g/l and a pH 10 in Current Density (CD) respectively is an efficient method for the treatment of petroleum wastewater

KEYWORDS: *TiO_2, nano, electrocoagulation, petroleum refinery effluent; COD reduction*

1.0 INTRODUCTION

Petroleum effluent contains free hydrocarbons, suspended solids, phenol, benzene, sulphides, ammonia, heavy metals, cyanide, mercaptans, solvents, inorganic elements having high concentration of salts, and organic carbon [1]. The current regulation of discharge limits for petroleum effluents prior to discharge into water bodies is in accordance with the Presidency of Meteorology and Environment (PME). The most toxic compounds present in petroleum effluent, according to the cooperative survey by the Environmental Protection Agency (EPA) and the American Petroleum Institute (API), are: methylene chloride, benzene, carbon tetrachloride, trichloroethane,

phenol, toluene, chloroform, trichloroethylene, ethyl benzene, pyrene, di-n-butyl phthalate, and bis (2- ethylhexyl) phthalate. These compounds cause major environmental impacts such as oxygen depletion and toxic effects on aquatic life tainting the water, and making it unsuitable for human use. Also, many studies have shown that oily effluents often have an impact on the fauna, fish, crustaceans, plankton, and algae, especially in the areas around the outfalls.

Biochemical Oxygen Demand (BOD) and Chemical Oxygen Demand (COD) values are in the range of 150-200 ppm and 300-600 ppm [1]. Typical cyanide, oil, phenols, benzene, sulfide, ammonia and heavy metals can be found in refinery effluents. Dependent of the source (surface water, ground water, re-used water) the make-up water will need a specific treatment such as sand filtration, iron removal, and (partial) softening. In addition, chemicals are dosed to control corrosion and biofouling. For boiler feed water the water is desalinated (reverse osmosis, ion exchange).

Nanoparticles are materials having a size in the range of 1–100 nm. Iron oxide, titanium dioxide, fullerenes and carbon nanotubes have been made into nanoparticles [2]. Titanium dioxide is an effective reducing agent and catalyst for various applications in environmental remediation [3]. The heterogeneous reaction using TiO_2 involves five steps: (i) mass transfer of the reactant to the TiO_2 surface from the bulk solution; (ii) adsorption of the reactant on the TiO_2 surface; (iii) chemical reaction at the TiO_2 surface; (iv) desorption of the reaction product from the TiO_2 surface; and (v) mass transfer of the product into the bulk solution [4]. Treatment of wastewater using nano-scale iron particles represents a new generation of environmental remediation and this provides cost-effective solutions to some important environmental problems [5]. The scope of the present study is the treatment of petroleum refinery wastewater sonochemically in the presence of TiO_2. TiO_2 particles were synthesized from ferrous sulfate, and were characterized using Ultraviolet light is electromagnetic radiation (UV), scanning electron microgram (SEM), Fourier transform infrared spectroscopy (FTIR) and X-ray diffraction (XRD). According to their finding, the removal observed with venturi was higher than with the orifice plate in combination with Fenton chemistry.

The degradation experiments on p-chlorophenol using both electrocoagulation and hypervalent iron and concluded that the electroassisted ferrate degradation method was more effective than the simple ferrate method [6]. Afzal et al [7] studied the combined action of sonochemical and UV irradiation for the treatment of carbaryl

(Carcinogenic compound). The sample was treated in an electrocoagulation reactor with three different current densities. The highest degradation of carbaryl was achieved at 130 KHz compared to 35 KHz. The combination of ultrasound and UV irradiation was considerably more effective than when UV or electrocoagulation was operated individually. Based on the sonochemical degradation of Congo red, the results showed that the initial dye concentration and pH of the dye solution influenced the decolorization and low initial values resulted in high decolorization [8]. Basiri [9] reported on the reduction of nitrite by electrocoagulation dispersed nanoscale TiO_2 and showed that TiO_2 could be an efficient reductant. Ther using of TiO_2 is to reduce nitrobenzene in aqueous solutions [10].

The scope of the present study is to treat petroleum refinery wastewater sonochemically in the presence of TiO_2. TiO_2 particles were synthesized from ferrous sulfate, and were characterized using scanning electron microgram (SEM) and X-ray diffraction (XRD) and Fourier Transform Infrared Spectroscopy (FTIER).

2.0 METHOD

2.1 Apparatus

The electro-oxidation process was carried out in a batch electrochemical reactor. Iron was used as anode and ruthenium oxide coating titanium as cathode with surface area of 45cm^2, working volume of 500 milliliter and sonication time of 10 min.

Chemical oxygen demand measurements were performed using COD digester (Open reflux method). All pH measurements were made using a digital pH meter.

2.2 Wastewater characteristics

The petroleum effluent was collected from a professional automobile service station in Baghdad, Iraq. Oily effluent is considered as one of the most serious polluting sources, as it contains toxic substances such as phenols, petroleum hydrocarbons, oil and grease, high biological oxygen demand (BOD) and chemical oxygen demand (COD) loads. This type of effluent comes from different sources, such as water produced from crude oil production, petroleum refinery, petrochemical, metal processing and car washing. The professional automobile service stations include all services like automobile maintenance, washing, and change of engine oil.

Petroleum wastewater from an automobile service station is caused by mixing of automotive oil, such as lubricant oil with emulsifiers and wash water. The initial characteristics of the petroleum effluent are as shown in Table 1.

Table 1: Characteristics of the Petroleum Effluent

S. No.	Parameters	Values
1	pH	7
2	Oil and grease	570mg/L
3	Total solids (TS)	1750mg/L
4	Total dissolved solids (TDS)	1610mg/L
5	Total suspended solids (TSS)	110mg/L
6	Chemical oxygen demand (COD)	3000mg/L
7	Biological oxygen Demand	370mg/L

2.3 Preparation of TiO2

The material used is a special grade reagents Titanium (IV) isopropoxide (Aldrich Chemicals Ltd., USA), Glacial acetic acid. All chemicals were reagent grade and used without further purification. Ultra pure deionized water was used in all the preparations.

The typical synthesis procedure for the preparation of TiO_2 nanoparticles by sol-gel method is as follows. Initially, 18.6 ml of Titanium (IV) isopropoxide was hydrolyzed by 35.8 ml glacial acetic acid at 0 ºC in which 395 ml of water was added drop wise to this solution under vigorous stirring for 1 h and the stirring was continued for a further 5 h. The prepared solution was kept in the dark for 24 h for nucleation process. After the period, the solution was placed in an oven at 70 °C for 12 h for gelation and aging process. The gel was then dried at 100 °C and subsequently the product was crushed into fine powder.

During the sol-gel synthesis of TiO_2 nanoparticles, high water ratio was kept to enhance the nucleophilic attack of water on titanium (IV) isopropoxide and to suppress the fast condensation of titanium (IV) isopropoxide species to yield TiO_2 nanocrystals.

2.4 Degradation experiments

Degradation experiments were performed in an electro oxidation reactor. Anode used was rhenium oxide coated titanium and cathode used was iron, while the area of the anode was 45cm^2. About 2000 ml

of the wastewater sample was placed in a beaker that was covered by a water bath to maintain constant temperature during Electro oxidation. To the beaker was added about 0.05 g of TiO_2, and Electro-oxidation was performed for 120 min. 1 ml samples were withdrawn at 5 min intervals and centrifuged for 10 min at 6000 rpm. The supernatant was subjected to COD determination. The pH optimization studies were performed under various initial pH conditions, including pH = 4, 6, 7, 8 and 10. At the optimum pH, nanoparticle dosage was then varied 0.05 g/L, 0.1 g/L and 0.15 g/L.

2.5 Analytical methods

Chemical oxygen demand (COD) was determined by the Open Reflux method.

3.0 RESULTS & DISCUSSION

3.1 Apparatus

The %COD remaining with respect to time of exposure to Effect of Oxidation time is shown in Fig.1. The results show clearly that the % degradation of wastewater increases with an increase in time and almost 60% of degradation was achieved in 120 min.

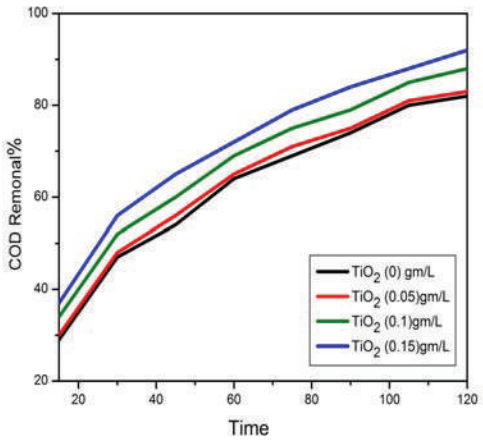

Figure1: Effect of Oxidation time on % COD removal

Generally, prolonged exposure of wastewater to electro-oxidation may enhance the generation of oxidative species in water. This is initiated by the hemolytic cleavage of water molecules by pyrolytic reactions, which may be represented as follows:

$$H_2O \longrightarrow OH + H \quad (1)$$

$$2\,OH + 2H \longrightarrow H_2O_2 + H_2 \quad (2)$$

The OH and $H2O_2$ are strong oxidizing agents, and the production rate of such oxidants depends on the final temperature and pressure at the time of bubble collapse. These oxidizing agents are responsible for the degradation of organic substances present in the wastewater.

3.2 Characterization of TiO2

Fig.2 shows the absorption spectra of TiO_2 nanocomposites taken at room temperature. The sample possess an absorption edge around 370-430 nm.

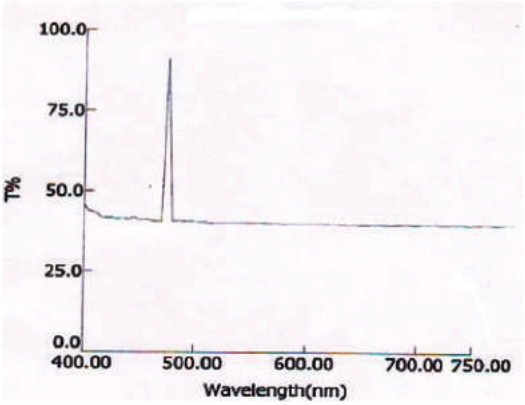

Figure 2: UV–vis spectrum for TiO_2 nanoparticles.

The scanning electron microscopy (SEM with EDX) image of synthesized TiO_2 particles were shown in Fig 3. The results indicate that the synthesized TiO_2 particles are almost spherical. Fig. 3(a) shows evenly distributed spherical particles approximately 1μm in size, and Fig. 3(b), under higher magnification, confirms the spherical shape and the size range of each particle. Fig.3 (b). These structures increased the available surface area of reaction. Fig.3 (c) shows the wt% for TiO_2 as 70.9 for Ti and 29.1 for O. Fig.4 shows the X-ray diffraction pattern of the TiO_2 sample annealed at 300°C in air for 1 h. The spectrum shows two major diffraction intensity peaks at $2\theta = 36.08°$ and 41.01°. The peaks were identified to originate from the (1 1 0), (1 1 1), (2 1 1), (2 2 0),

(0 2 2), (3 1 0) and (3 0 1) planes of FeO respectively (JCPDS no: 772355). The X – ray could be indexed to the $Fm^{-}3m$ (225) face group (Face – centered) cubic structure, with cell parameter a = 4.309 Å.

The information on the particle size was obtained from the full width at half maximum (FWHM) of the diffracted beam using scherrer formula: The crystalline size was calculated using Debye-Scherrer formula.

$$D = \frac{0.9\lambda}{\beta \cos\theta} \quad (3)$$

a : magnification at 20 lm/200

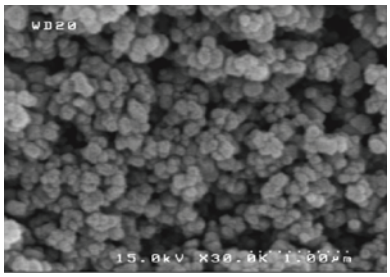

b: Magnification at 10 lm/1000

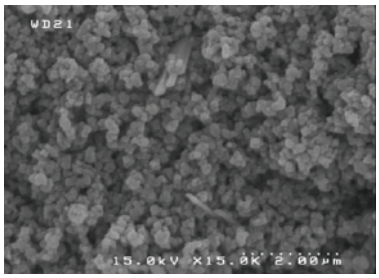

c: EDX of TiO_2

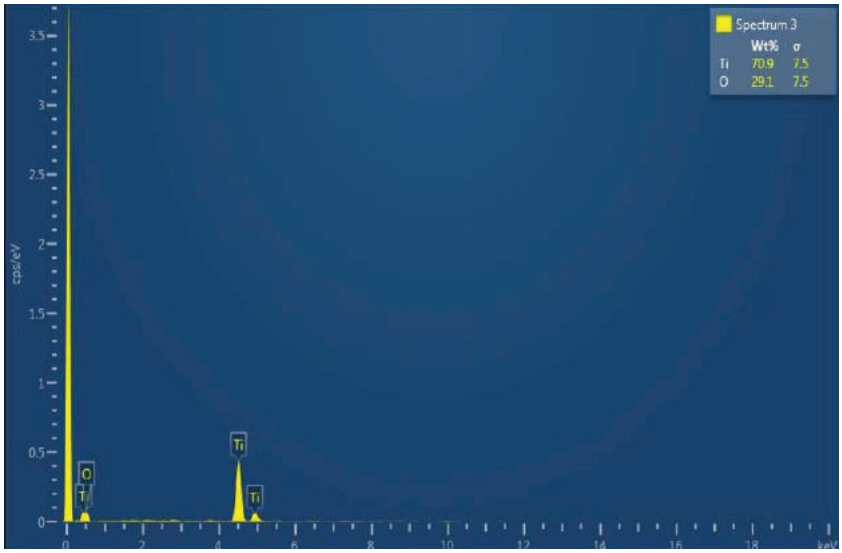

Figure 3: SEM –EDX images of TiO_2

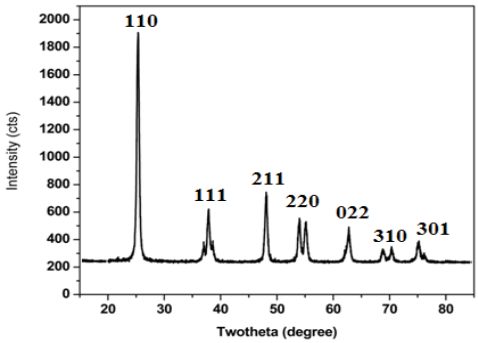

Figure 4: X-ray diffraction analysis of TiO_2 samples

The sample has an average crystalline size 226 of 3l.l nm +0.5.

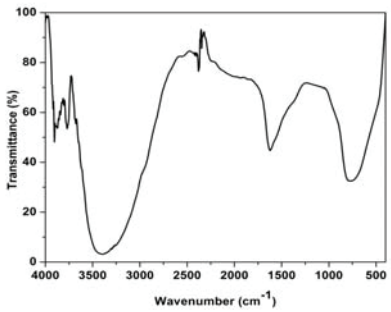

Figure 5: FTIR spectrum of TiO_2.

Fig.5 shows the absorption peak at 3457cm-1 as representation of the O-H stretching vibration of free water and its corresponding O-H bending vibration occurred at 1636 cm-1 due to the chemically adsorbed water.

3.3 Effect of current density

TiO_2 assisted Electro oxidation degradation was carried out and the %COD removal with respect to time is shown in Fig.6. During the first 5 min of the reaction, the reduction was much higher. This is due to the initial reaction of TiO_2 with the organic pollutants that are highly susceptible to oxidization. Later, due to the effect of oxidization, the COD continued to decrease to a considerable level, but became constant after a certain time. This may either be attributed to the presence of nondegradable organics in the effluent or to the exhaustion of TiO_2 particles.

The destruction may be improved by increasing the amount of TiO_2. In this kind of reaction, there are two ways in which the organic pollutants are degraded, namely, through pyrolysis and reduction on TiO_2 surface.

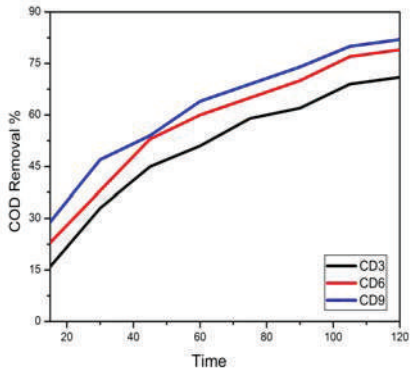

Figure 6: Effect of current density on COD with treatment time of 120 mins at pH=7.

3.4 Effect of pH

The effect of pH on the %COD removal after 120 min of processing is shown in Fig.7. From the results suggested by the figure, it could be noted that at pH 4, pH 6, pH 7, pH 8 and pH 10 the %COD removal value was much lower and hence the effective reduction took place at this pH. However, when the pH was adjusted to 6, a poorer effect on COD reduction was noted. This may be due to the reduced activity of TiO_2 under pH conditions.

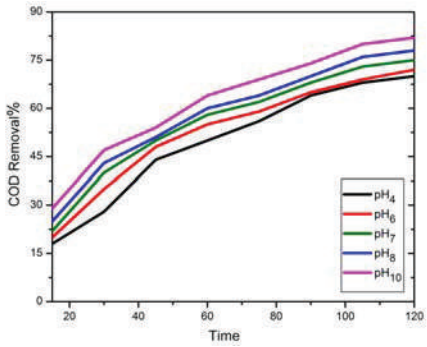

Figure 7: Effect of pH on % COD removal at treatment time of 120 min

3.5 Effect of TiO2 Dosage

The changes due to % COD under various TiO_2 dosage conditions are shown in Fig.8. The results show that an increase in TiO_2 dosage increased the reduction in COD, as the %COD removal decreased. This can be attributed to an increase in the surface area of TiO_2 accessible for the organic pollutants.

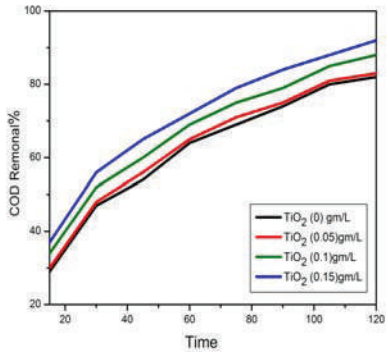

Figure 8: Effect of TiO_2 on % COD removal at treatment time of 120 min

4.0 CONCLUSSION

TiO_2 nanoparticles prepared through a liquid-phase reduction method are almost spherical and exhibit higher surface area available for reactions. The absorption spectrum of TiO_2 at 400 nm is due to the charge-transfer from the valence band (mainly formed by 2p orbitals of the oxide anions) to the conduction band (mainly formed by 3d t2g orbitals of the Ti4+ cations). The broad intense absorption edge of the spectrum is the result of formation of nanoparticles. The SEM find on the spherical particles where there were thread-like or tube-like structures clearly visible in these structures due to increased the available surface area of reaction. The sample annealed at 300°C/1h has an average crystalline size of 31.1 nm ±0.5. As the annealing time or temperature increases, the crystalline size increases. The band at 2432 cm-1 is assigned to C-H vibrations. The C-H could be attributed to the organic residues, which remained in TiO_2 even after calcinations. The broad intense band below 1200 cm-1 is due to Ti-OTi vibrations. Reduction test results indicated that oxidization can accelerate the reduction of organic pollutants present in wastewater when used with TiO_2. The degradation of organic pollutants present in wastewater with TiO_2 under Electro oxidation. Experiments carried out under various CD, pH levels revealed and dosage of TiO_2. The electro oxidation experiments

for the treatment of petroleum wastewater using ruthenium oxide coated titanium as the anode and iron as the cathode. were conducted in batch reactor. The optimized conditions was absorbed at current density of 9 mA/cm^2, pH of 10, catalyst additional of TiO_2 0.15 g/L, and treatment time of 120 min. Under these conditions, the COD removal efficiency of 92 %, were estimated. The electrochemical techniques are viable processes for the treatment of oily wastewater. The degradation strongly depended on pH 10 while efficient degradation occurred in acid media. TiO_2 serves as a substantial part that can be added to the reaction to reach desirable results.

REFERENCES

[1] Q. J. Rasheed, K. Pandian and K. Muthukumar, "Treatment of petroleum refinery wastewater by ultrasound-dispersed nanoscale zero valent iron particles," *Ultrasonics Sonochemistry*, Vol 18 No. 5, pp.1138-1142, 2011.

[2] H. Shi, R. Magaye, V. Castranova and J. Zhao, "Titanium dioxide nanoparticles: a review of current toxicological data," *Particle and Fibre Toxicology* , Vol.10 No.15, pp.1-33, 2013.

[3] K. W. Pi, Q. Xiao, H. Q. Zhang, M. Xia and A. R. Gerson, "Decolorization of synthetic Methyl Orange wastewater by electrocoagulation with periodic reversal of electrodes and optimization by RSM," *Process Safety and Environmental Protection*, Vol. 92 No.6,pp.796–806, 2014.

[4] L. Lei, N. Wang, X. M. Zhang, Q. Tai, D. P. Tsai, and H. L. W. Chan," Optofluidic planar reactors for photocatalytic water treatment using solar energy," *Biomicrofluidics*, Vol. 4 No.4,pp. 1932-1058, 2010.

[5] Q. J. Rasheed, "Synthesis and Optimization of Nisin-Silver Nanoparticles at Different Conditions," *Engineering & Technology Journal*, Vol.33 No.2, pp.331-341, Part (A), 2015.

[6] M. V. Bagal and P. R. Gogate, "Wastewater treatment using hybrid treatment schemes based on cavitation and Fenton chemistry: A review ," *Ultrasonics Sonochemistry*, Vol. 21 No.1, pp.1–14, 2014.

[7] A. Afzal, P. Pourrezaei, N. Ding, A. Moustaf, G. Hwang, P. Drzewicz, E.S. Kim, L. A. Perez-Estrad, P. Chelme-Ayal, Y. Liu and M. G. El- Din," Physico-Chemical Processes Water," *Environment Research*, Vol. 83 No. 10, pp.994-1091.

[8] K.P. Gopinath , K. Muthukumarand and M. Velan,"Sonochemical degradation of Congo red: Optimization through response surface methodology," *Chemical Engineering Journal* ,Vol. 157 No.2-3, pp. 427- 433, 2010.

[9] J. B. Parsa, "Treatment of wastewater containing Acid Blue 92 dye by advanced ozonebased oxidation methods," *Separation and Purification Technology*, Vol.98,pp. 315-320, 2012.

[10] E. A. Reynoso-Soto, S. Pérez-Sicairos, A. P. Reyes-Cruzaley, C. L. Castro-Riquelme, R. M. Félix-Navarro, F. Paraguay-Delgado, G. Alonso-Núñez and S. W. Lin-Hoa, "Photocatalytic Degradation of Nitrobenzene Using Nanocrystalline TiO2 Photocatalyst Doped with Zn Ions," *Journal of the Mexican Chemical Society*, Vol. 57 No.4,pp. 298- 305, 2013.

APPLICATION OF THEORY OF INVENTIVE PROBLEM SOLVING FOR SYSTEMATIC INNOVATION: CASE STUDY OF WATER DISPENSER DESIGN

M.R., Mansor[1], H., Rusnandi[2] and W.N., Mohd Isa[3]

[1,2]Faculty of Mechanical Engineering,
Universiti Teknikal Malaysia Melaka, Hang Tuah Jaya, 76100 Durian Tunggal, Melaka, Malaysia.

[3]Faculty of Computing and Informatics,
Multimedia University, 63100 Cyberjaya,
Selangor, Malaysia.

Email: [*1]muhd.ridzuan@utem.edu.my; [2]herdy@utem.edu.my;
[3]noorsha@mmu.edu.my

ABSTRACT: This paper analyzed an application of the Theory of Inventive Problem Solving (TRIZ) method in providing systematic innovation process of consumer product. The TRIZ tools namely contradiction matrix and 40 inventive principles were employed in this project. The contradiction matrix was applied for problem identification purpose whereas the 40 inventive principles were employed to generate conceptual solutions for the problem. The application of both tools was demonstrated through a case study of water dispenser. Based on the case study, the utilization of the TRIZ tools resulted in the development of new water dispensing bottle design which was able to offer a simple and cost effective solution while retaining the current principle of operation especially during the water bottle changeover process.

KEYWORDS: *TRIZ, Contradiction Matrix, 40 Inventive Principles, Water Dispenser.*

1.0 BACKGROUND

TRIZ is a Russian acronym for "Theory of Inventive Problem Solving" [1]. It is a systematic innovation theory developed by Genrich S. Altshuller after analysing thousands of patents in the 40s. TRIZ has been successfully implemented by big companies, such as Samsung, General Electrics (GE), Intel, and many others to assist with product and technological innovation [2].

TRIZ is based on "contradictions that can be methodically resolved through the application of innovative solutions" [3]. TRIZ has three premises; an ideal design; contradictions that help to solve problems; innovative process which can be structured systematically [3].

Contradictions are technical compromises or trade-offs that lie in an engineering system where some design parameters have become worsen in order for the problem to be solved. TRIZ has been demonstrated for ceramics processing in 70 ways, whereby its aim is "to teach ceramics processing to the next generation of scientists and engineers but closely allied to classification is the question of creativity and inventiveness and how they are fostered". The contradictions refer to simplified ceramics processing classification, increased inventiveness, and good practice [4].

A case study of a notebook design in research and development was presented by Yeh, Huang and Yu [5] through an integration of quality function deployment (QFD) and TRIZ. QFD has been implemented in four phases to identify major contradictions. At each phase of the QFD, major contradiction has been identified and TRIZ has been applied to resolve the contradiction. The final outcomes are three breakthrough solutions generated from the TRIZ 40 Inventive Principles.

Moreover, TRIZ has also been illustrated in the design of a passively compliant robotic joint [6]. Based on their report, TRIZ was demonstrated as a systematic methodology for enhancing creative capability in the design of an innovative robotic joint. Two contradictions have been identified from five literature studies. TRIZ Inventive Principles have been applied to resolve the contradictions and a prototype has been developed and experimentally tested.

TRIZ has also been adopted in a design of an implanted biomedical device, a tracheal stent that fulfills the need of each patient and approve by physicians at the same time [7]. The contradiction occurs due to required customization of the tracheal stent on patients but such tracheal stents come in many materials, shapes, and characteristics. A parametrization tool has been implemented that guides modification of the general dimensions of stents to fit each specific patient. The QFD method has been applied prior to TRIZ to visualize and summarize the design attributes.

Based on the discussion from the aforementioned literatures [3 – 7], resolving contradictions through TRIZ can lead to innovative solution. Thus, based on the TRIZ method, this paper aimed to identify the contradictions that occurred in developing solutions for problems involving consumer products. The application of the TRIZ tools was shown through a case study to solve the contradiction that occured in the bottle changeover process of a water dispenser. Implementation of TRIZ contradiction matrix tool was first conducted to resolve the

contradiction. Finally, solution generation for the contradiction was performed using TRIZ 40 inventive principles to come up with an ideal water dispensing design.

2.0 RESEARCH METHODOLOGY

Figure 1 shows a general framework of the problem solving process in this study [1]. The framework comprises four steps, which conceptually follows similar classical TRIZ problem solving method as shown in Figure 2. The first step in problem solving process is problem definition. In this step, the problem should be clearly defined and what benefits are expected if the problem is solved. The information about limitations of the existing condition and the requirements of the solution are also essential so that the problem formulations can be clearly stated.

The second TRIZ problem solving process involves development of TRIZ model of the problem. In this paper, TRIZ technical contradiction was used to model the problem. The term contradiction is applied in TRIZ to represent the compromise in which designers need to decide upon when implementing a solution. For example, the design intents to improve the weight (reduce the weight) of a product by reducing the product thickness for better maneuverability may also cause deterioration on the product strength in handling the given load. Thus, the contradictions occurred in TRIZ is solved simultaneously to obtain the best solution without having to make a trade-off or compromise in the design.

The next step involves an application of 40 Inventive Principles to solve problem of the developed model of. In the last TRIZ process, the final result of the specific solution which generally covers the solution idea is generated from the selected potential solution obtained in previous step.

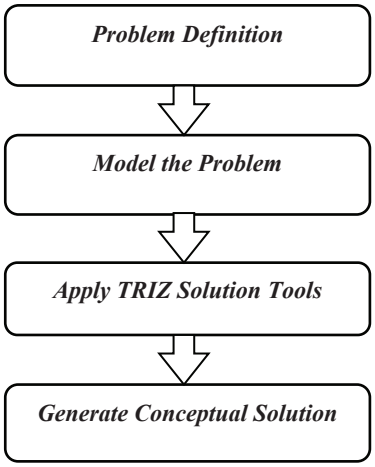

Figure 1: TRIZ problem solving process flow

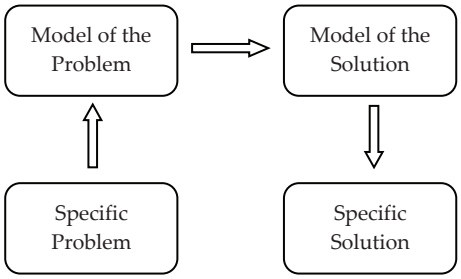

Figure 2: Classical TRIZ problem solving method

3.0 CASE STUDY ON WATER DISPENSER

An application of TRIZ method in solving problem and developing innovative solution in this paper is demonstrated through a case study on water dispenser equipment. A water dispenser unit is daily consumer equipment that provides clean drinking water to the user. In general, there are two types of water dispensing unit; one which uses a dedicated water bottle to supply water (manual refilling method) and the other is the one which is integrated with water pipe as the source of water supply (automatic refilling method). The design of the dedicated water dispensing product is relatively cheaper compared to the integrated dispenser-piping design. However, it requires users to selfchanging the water bottle after it is empty. As shown in Figure 3, the manual water dispenser encompasses four main components, the refill bottle, dispenser insert, dispensing units (for hot and cold water) and dispenser main body.

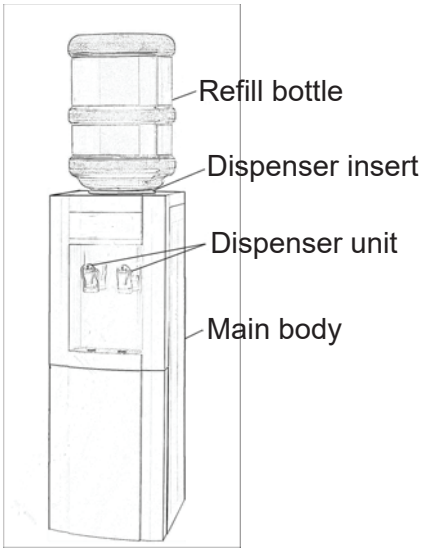

Figure 3: Main components of manual water dispenser

The refill bottle helps to provide high water consumption capacity that is able to cater for many users which is very economical to be used in offices and public places. The issue arises during the refilling process due to the weight of the replacing full water bottle with normal capacity of 5-gallon (22.7 L) . With approximate weight of 23 kg, the refill bottle imposes negative refilling process issue to the consumer particularly women to lift the heavy refill bottle and place it in the correct position on the top of the water dispenser. Thus, the solution to solve the contradiction is determined through implementing TRIZ method.

3.1 Problem Definition using TRIZ

In TRIZ method, the problem was first classified based on the contradiction occurred. As for the water dispenser, the current design provides high drinking capacity and less refilling process. However, imposed refilling difficulty due to high force is required to lift the heavy refill bottle. Thus, based on the situation, TRIZ classified the contradiction as an engineering contradiction, whereby improving one parameter resulted in creating other negative parameter. Using TRIZ method, the specific problem is later converted into general problem based on the TRIZ 39 system parameters definition. The process to generalize the specific problem into more general term representing the situation enables more ideas to be generated by removing the creative thinking barrier caused by the influence of complex technical term. In TRIZ, the problem definition or engineering contradiction statement is formulated based on the "ifthen- but" principle. In general, the word

"if" corresponds to the manipulating variable of the solution such as length, volume and shape while the word "then" corresponds to the positive or improving condition which the solution is intended to achieve such as increasing strength of the product. The last word to formulate the engineering contradictions statement which is "but" in the other hand corresponds to the negative or worsening condition when the solution is implemented, such as increasing the weight of the product [1].

Thus, the specific problem defined into engineering contradiction statement according to TRIZ method was formulated as follows:-

If the refill bottle volume is large, then more drinking water capacity is available but more difficult to lift the refill bottle.

3.2 Solution Generation using TRIZ

Based on the previous engineering contradiction statement, the improving parameter related to TRIZ 39 general system parameter was defined. Based on the TRIZ method, the improving and worsening condition for the problem can be linked with the TRIZ 39 system engineering parameters. The 39 system engineering parameters available in TRIZ include weight of stationary object, weight of moving object, speed, force, strength and shape. Based on the water dispenser problem statement and engineering contradiction statement, two (2) TRIZ engineering parameters were selected which were productivity (parameter no.39) to represent the improving aspect intended for the new design and the coupling worsening effect due to large refill bottle which reduced the ease of operation (parameter no.33) of the whole refilling process. The general parameters obtained were then arranged into the TRIZ contradiction matrix whereby potential solution could be obtained based on the TRIZ 40 inventive principles solution. TRIZ 40 inventive principles solution tool reflects 40 solution principles that are available to be selected. The selection of the solution principles was based on the recommendation after creating the contradiction matrix. Table 1 shows the contradiction matrix formed for the water dispenser problem based on the TRIZ 39 engineering parameters.

Table 1: Contradiction matrix for the water dispenser refilling process based on the TRIZ 39 Engineering Parameters [1]

Improving Parameter	Worsening Parameter	TRIZ 40 inventive solution principles
#39. Productivity	#33. Ease of Operation	#1. Segmentation #28. Mechanics substitution #7. Nested doll #10. Preliminary action (prior action – "do it in advanced")

Based on the contradiction matrix formulated as shown in Table 1, there were four (4) suitable inventive solution principles that could be applied to the problem such as segmentation and mechanics substitution. The next stage in the water dispenser problem solving process using TRIZ method was developing specific solution strategies to solve the occurred contradiction based on the four (4) recommended solution principles shown in Table 1 previously. After analyzing the four (4) solution recommendations namely segmentation, mechanics substitution, nested doll and preliminary action, two (2) possible specific solution strategies were able to be formulated which were related to inventive solution principle no. 1 (segmentation) and no. 10 (preliminary action). Based on the TRIZ general solution recommendations, specific solution strategies related to inventive solution segmentation and preliminary action formulated by the designer as shown in Table 2.

Table 2: Specific solution strategy based on the TRIZ solution principles

TRIZ 40 inventive solution principles	Solution descriptions	Specific solution strategy
#1. Segmentation	a) Divide an object into different parts b) Make an object easy to disassemble c) Increase the degree of fragmentation or segmentation d) Transition to micro-level	a) Use many small refill bottles instead on one large refill bottle. The insert component is also redesigned to from 1 unit to multiple units.
#10. Preliminary action	a) Perform the required change of an object (either fully or partially) before it is needed b) Pre-arrange objects such that they can come into action from the most convenient place and without losing time for their delivery	a) Redesign the refill bottle with handle for ease of handling

Based on the specific solution strategies, new conceptual designs of the refill bottle and the dispenser insert component were developed (refer to Figure 4).

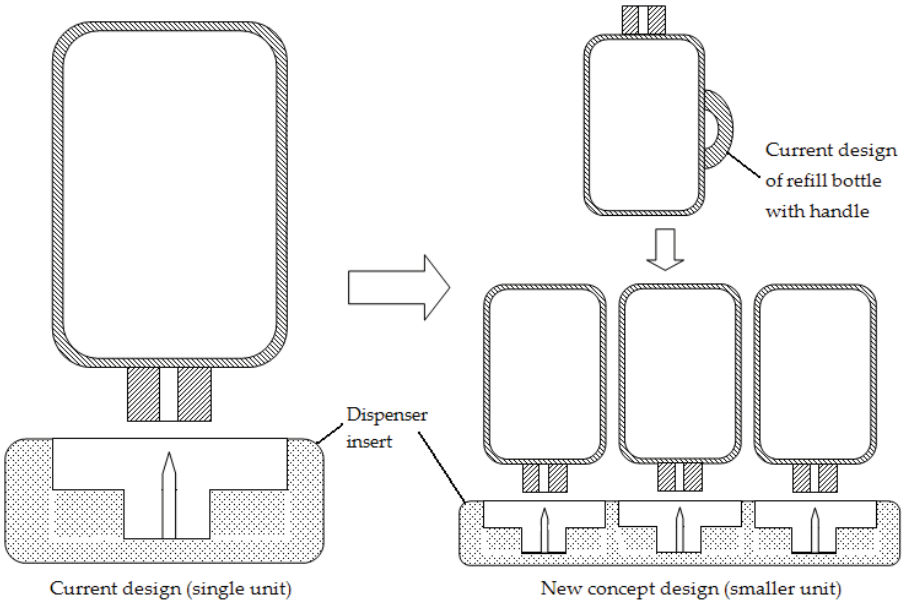

Figure 4: New conceptual design of refill bottle with handle and dispenser insert component for manual water dispenser

The new refill bottle conceptual design developed using the TRIZ tools was smaller in size compared to the initial bottle design. However, by using the new dispenser insert design, many smaller refill bottles could be attached to the dispenser at once to ensure that high water capacity was maintained similar to using single large refill bottle used previously. Another advantage of the new design was that the lifting process of the new smaller refill bottle required less lifting energy. Thus, it can be operated easily especially by women users. Additional advantage of the new design was reflected through the handling process which was also improved by the addition of handle to the bottle for a better grip and an ease of placing the bottle correctly to the dispenser insert section. In addition, the new redesign dispenser insert with undercut slot was also able to expedite and provide precise placement of the refill bottle onto the insert. The application of the TRIZ tools as demonstrated through the case study has provided systematic problem definition and idea generation processes to determine the required solution. Moreover, the solutions generated at the end of the conceptual design process were also able to solve the current problem without having to make a trade-off on the design performance which is usually challenging to be realized using conventional solution generation process.

4.0 CONCLUSIONS

In conclusion, the applicability of the TRIZ method in problem solving process has been demonstrated based on the case study of water dispenser design. It has been shown that the TRIZ method is able to provide innovative solutions to the sample problem through utilization of systematic approach which covers problem definition, idea generation and conceptual solution development. The structured problem solving process is also able to quickly assist in exploring possible solutions based on its proposed solution principle method. In addition, the solutions generated at the end of the conceptual design process are also able to solve the current problem without having to make a trade-off on the design performance which is usually challenging to be realized using conventional solution generation process.

ACKNOWLEDGMENTS

The authors would like to thank Universiti Teknikal Malaysia Melaka and Multimedia University for supporting this project.

REFERENCES

[1] T. S. Yeoh, T. J. Yeoh, and C. L. Song, TRIZ - *Systematic Innovation in Manufacturing*. Malaysia: Firstfruits, 2011.

[2] S. Hamm, Tech Innovations for Tough Times, http://www.bloomberg.com/bw/stories/2008-12-25/tech-innovationsfor-tough-timesbusinessweek-business-news-stock-market-andfinancial-advice, retrieved online of 2nd February 2016.

[3] F. C. Labouriau and R. M. Naveiro, "Using the evolutionary pattern to generate ideas in new product development". *J. Braz. Soc. Mech. Sci. Eng.*, Vol. 37, pp. 231-42, 2015.

[4] J. R. G. Evans, "Seventy ways to make ceramics". *J. of the European Ceramics Soc.*, Vol. 28, pp. 1421-32, 2008.

[5] C. H. Yeh, J. C. Y. Huang, and C. K. Yu, "Integration of four-phase QFD and TRIZ in product R&D: a notebook case study". *Res. Eng. Design,* Vol. 22, pp. 125-41, 2011.

[6] D. Petković, M. Issa, and N. D. Pavlović, "Application of the TRIZ creativity enhancement approach to design of passively compliant robotic joint". *Int. J. Adv. Manuf. Technol.*, Vol. 67, pp. 865-75, 2013.

[7] E. L. Melgoza, L. Serenó, A. Rosell, and J. Ciurana, "An integrated parameterized tool for designing a customized tracheal stent". *Computer-Aided Design,* Vol. 44, pp. 1173-81, 2012.

MICROELECTRONICS THERMAL DISSIPATION CHARACTERIZATION USING TRIZ

M.C., Ong[1], M.N., Abd Rahman[2]

[1,2]Faculty of Manufacturing Engineering,
Universiti Teknikal Malaysia Melaka, Hang Tuah Jaya, 76100 Durian Tunggal, Melaka, Malaysia.

Email: [*1]bromingchung@yahoo.com; [2]mdnizam@utem.edu.my

ABSTRACT: Thermal dissipation of a microelectronic device is a topic of interest amongst the researchers because poor thermal dissipation may cause reliability problem during customer's application. One of the factors that caused poor thermal dissipation of a device is the existence of air gap inside the package. Air gap blocks the heat dissipation path of the device, causing the heat to be entrapped inside the device and to the extent of becoming malfunction. In this analysis, TRIZ was proposed through Parameter Change (PC) as one of the principle solutions to increase the effectiveness of identifying poor thermal dissipation devices. Experiment confirmed that TRIZ PC principle was able to identify poor thermal dissipation in microelectronic device even though the device did not have air gaps. Such identification was not possible through traditional approaches, such as XRay or SAM.

KEYWORDS: *Air Gap, Thermal Dissipation, TRIZ*

1.0 INTRODUCTION

Ability to dissipate heat is one of the important elements in ensuring functionality of a microelectronic device. The thermal dissipation is mainly achieved by means of conduction from the die to the package and by convection from the package to the external environment. One of the common problems faced in thermal dissipation in such device is the presence of air gap between the die and package which significantly reduces its thermal impedance and thermal dissipation capability [1]. Such device potentially has poor reliability performance and has to be selected out. The presence of air gap will slower down the thermal dissipation of the device, but wafer process defects like ionization, inhomogeneous current distribution within a cell field or some parasitic capacitance and inductance may contribute as well to the poor thermal dissipation of the device even though the device is without the presence of air gap [2-3].

X-Ray and SAM are the traditional approaches that are widely used to identify an air gap inside microelectronic device which has potentially poor thermal dissipation. However, these approaches require lots of effort and time. Moreover, X-Ray and SAM are performed by sampling basis only. Nevertheless, electrical measurement may fit in the gap to identify such poor heat dissipation devices if appropriate condition is used as shown in Table 1. The challenge is on the effectiveness of the electrical measurement to identify poor thermal dissipation device because using too low Energy, the measurement may not be sensitive enough; but if using too high Energy, the device may become destructive. This is a typical contradiction found in this Inventive Problem which can be solved by using "The Theory of Inventive Problem"-TRIZ which is a well structured approach to stimulate new idea in solving the effectiveness problem [4]. Table 1 illustrates the advantages of electrical measurement compared to XRay and SAM.

Table 1: Advantages of Electrical Measurement compared to X-Ray and SAM

No	Area	X- Ray	SAM	Electrical measurement
1	Sampling Size	Sampling		100%
2	Time	~1 - 30mins		<1s
3	Effort	High(manual/semi-auto/auto setting)		Low
4	Effectiveness	Medium(wafer process defect can't be identified)		Low if inappropriate condition is used
				High if appropriate condition is used

The effectiveness of using TRIZ is proven because many researchers have unanimously agreed that TRIZ is able to help them to solve Inventive problem and generate more ideas, patents in improving a certain product, process or a system design [5-7]. In this paper, TRIZ methodology was illustrated systematically and how Principle Parameter Change (PC) was used to improve the effectiveness in identifying the poor thermal dissipation device by using electrical measurement was demonstrated.

2.0 ME THODOLOGY

2.1 TRIZ Approach

TRIZ was chosen due to two reasons. Firstly, "Contradiction" was found in the problem itself. By increasing the Energy used, the effectiveness could be increased; however, this increased of Energy

could bring reliability problems toward the device. This contradiction is best solved by using TRIZ because TRIZ deals with "Contradiction". Moreover, TRIZ is a well-structured approach to stimulate new idea in solving the effectiveness problem. This is very important especially in manufacturing and development field.

Figure 1 shows the flowchart of TRIZ. TRIZ begins by drawing the Functional Model Analysis for "Ineffective Electrical Measurement in identifying poor thermal dissipation device". Such diagram was to understand how the system, sub-system and the super-system of an "Ineffective Electrical Measurement in identifying poor thermal dissipation device" were connected. Cause-and-Effect analysis was provided after Functional Model Analysis to identify the root cause of ineffective electrical measurement in identifying poor thermal dissipation device. Next, based on the identified root cause, Engineering Contradiction statement was constructed. Specific improving and worsening system parameters were identified from Engineering Contradiction statement. When these improving and worsening System Parameters matched with the Contradiction Matrix, the related principles to improve the electrical measurement effectiveness in identifying poor thermal dissipation were proposed by TRIZ. In this study, Parameter Change (PC) principle was used to check the effectiveness of electrical measurement in identifying poor thermal dissipation device.

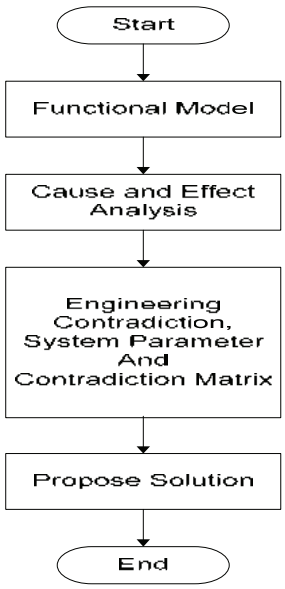

Figure 1: TRIZ Flow Chart

2.1.1 Functional Model

Functional Model analysis in Figure 2 was a modelling to analyze how the components of "Ineffective Electrical Measurement in identifying poor thermal dissipation device" interact with one another. From a typical "Function Model", the "Arrow (→)" is a function symbol that contains lots of information (Bold: Useful; Red: Harmful; Dotted line: useful but insufficient). Generally, if the function is useful, then it must be kept; otherwise it must be eliminated. For the function which is useful but insufficient, then improvement must be done to improve the insufficiency. The interpretation of Figure 2 was as follows: "*Measurement Condition*" was useful but insufficiently supplied to the "*Electrical Measurement*". Therefore, "*Electrical Measurement*" is not sensitive enough in measuring the "*Device*" and not able to distinguish between the good and poor heat dissipation device. In other words, "*Measurement Condition*" should be sufficiently applied to "*Electrical Measurement*" to increase the effectiveness of identifying poor thermal dissipation device.

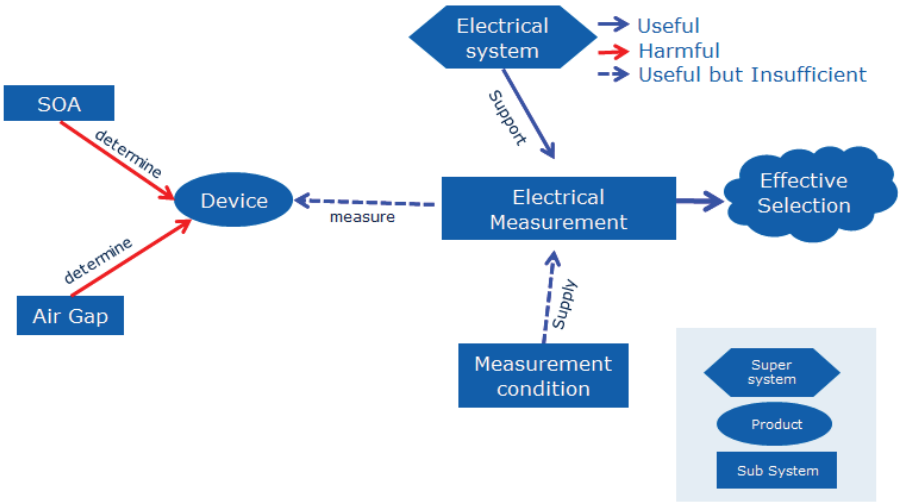

Figure 2: Functional Model of an "Ineffective Electrical Measurement in identifying poor thermal dissipation device"

2.1.2 Cause And Effects Analysis

By performing Cause-and-Effect (CAE) analysis, the root cause of ineffectiveness to identify the poor thermal dissipation device was found. By questioning on "Why the measurement is not effective in identifying poor thermal dissipation device?", the answer led to the root cause "Insufficient Measurement Condition" or "Inappropriate Measurement Condition". This again confirmed the observation seen

in the Functional Model Analysis where the "Measurement Condition" is the root cause for "Ineffective Electrical Measurement in identifying poor thermal dissipation device".

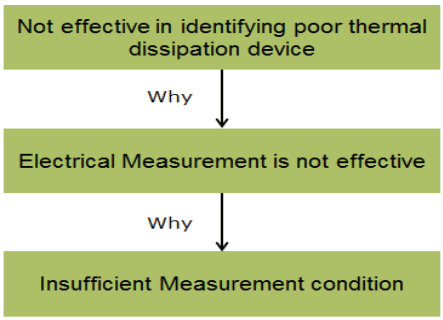

Figure 3: Cause and Effect Analysis for ineffective identification of poor thermal dissipation device.

2.1.3 Engineering Contradiction, System Parameter and Contradiction Matrix

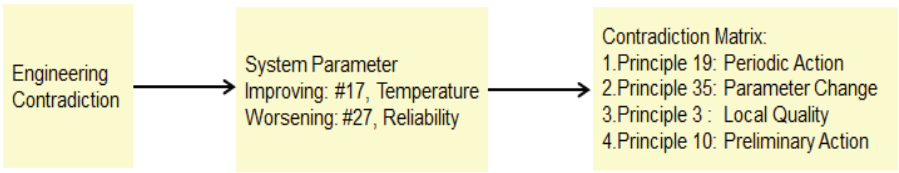

Figure 4: Engineering Contradiction, System Parameter, Contradiction Matrix

Next, based on the root cause mentioned above, Engineering Contradiction statement was constructed.

Engineering Contradiction:

Engineering Contradiction can be easily constructed using "If…then… but…" statement.

If the measurement condition is increased, then the *"Temperature"* of the device is increased, but this temperature rise might destroy the device or cause *"Reliability"* problem.

System Parameter:
From the above Engineering Contradiction statement, the improving and worsening system parameters were identified as follows:

Improving System Parameter: #17, Temperature
Worsening System Parameter: #27, Reliability

Contradiction Matrix:
By putting the improving system parameter #17, Temperature and worsening system parameter #27, Reliability in the Contradiction Matrix, TRIZ proposed the following principles to improve the effectiveness in identifying poor thermal dissipation device.

1. Principle 19: Periodic Action
2. Principle 35: Parameter Change
3. Principle 3 : Local Quality
4. Principle 10: Preliminary Action

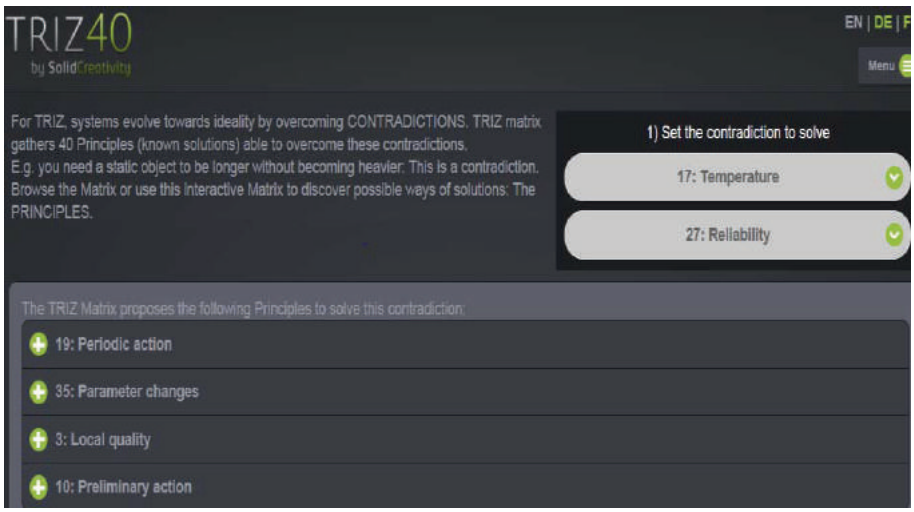

Figure 5: Solutions Proposed by TRIZ[8]

2.1.4 Propose Solution: Principle 35 "Parameter Change"

The solutions proposed by TRIZ must be carefully selected based on Engineering Judgement. Out of the principles proposed by TRIZ, only principle 19 "Periodic Action" and Principle 35 "Parameter Change" were more suitable to increase the effectiveness in identifying poor thermal dissipation devices. However, "Periodic Action" will not be discussed here due to the focus is on Principle 35, "Parameter Change".

In TRIZ context, the definitions for Principle "Parameter Change" were as follows:

a) Change an object's or system's physical state (e.g.: to a gas, liquid, or solid)
b) Change the concentration or consistency
c) Change the degree of flexibility
d) Change the temperature
e) Change other parameters

The definition of "D-Change the temperature" was most relevant in this study where the "Temperature" of the device can be increased by changing the Energy used to increase the effectiveness of identifying poor thermal dissipation device.

The experiment was carried out using with and without air gap device and using the existing measurement condition (Condition A, Before Changed of Energy) and new measurement condition (Condition B, After Changed of Energy). The results and findings were tabulated in the next section.

3.0 RESULTS AND DISCUSSION

3.1 Negligible Air Gap Device versus Air Gap Device

Figure 6 shows the SAM picture for 4 devices. A141 and A42 were with negligible air gap while B75 and B112 were with air gap. Theoretically, those devices with air gap would be having difficulty in thermal dissipation and therefore regarded as poor thermal dissipation device if compared to A141 and A42 which only had negligible air gap. The theory is proven through experiment and could be observed from Figure 8, Graph After "Parameter Change" where device B75 and B112 were showing "Elongated Non-Linear Curve" earlier than A141 and A42 when there was an increased in Current along X-axis. This "Elongated Non-Linear Curve" behavior was the "Curve line" in Y axis which happened especially on poor thermal dissipation device when heat was trapped inside the package and resulted in self - heating phenomena causing non-linear output response [9] before the device became malfunction. While the A141 and A42 still showed a stable linear graph, those poor thermal dissipation devices showed "Elongated Non-Linear Curve" Therefore, the quality performance between good and poor thermal dissipation devices was clearly distinguished. Device with air gap was poorer in thermal dissipation compared to device without air gap.

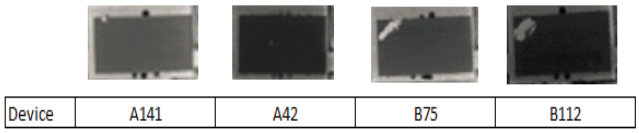

Figure 6: SAM Picture for 4 Devices

3.2 Poor Thermal Dissipation Device in Negligible Air Gap Device

Although A141 and A42 were both devices with negligible air gap, the device quality performance between the two was not identical and can be clearly distinguished as illustrated in Figure 8. Device A42 was observed to have "Elongated Non-Linear Curve" earlier than A141 before it became malfunction while A141 survived at the end of the experiment and did not have any "Elongated Non-Linear Curve". Such observation could be due to the weaknesses inherited from wafer processes [2-3] which caused device A42 performed poorer in thermal dissipation than device A141.

3.3 The Attribute of Poor Thermal Dissipation Device

Based on the experiments, air gap contributed to the poor performance of the device. With the existence of the air gap in the device, the thermal dissipation was rather slow if compared to the good device. However, poor thermal dissipation device may not contribute from the air gap alone. Weaknesses from wafer processes could affect the performance of the device. Therefore, electrical measurement was the better way in identifying poor thermal dissipation devices compared to traditional X-Ray or SAM approach.

3.4 Before and After "Parameter Change"

Following the TRIZ Approach, Figure 7 and Figure 8 show the Graph before "Parameter Change" and the Graph After "Parameter Change" respectively. "Before Parameter Change" which used Condition A (Before Change of Energy) showed that the sensitivity of the electrical measurement was not significant. Therefore, straight curve could be seen and there was no difference between the good and poor thermal dissipation device. However, "after Parameter Change" which used Condition B (After Change of Energy), the effectiveness in identifying poor thermal dissipation devices increased. Good device could be seen with a straight curve while poor thermal dissipation device showed "Elongated Non-Linear Curve". Hence, good and poor thermal dissipation devices were distinguishable.

3.5 X-Ray/SAM and Electrical Measurement in identifying poor thermal dissipation

Based on Table 2, X-ray/SAM is only capable of informing the general relationship between the big air gap and the thermal dissipation; the bigger air gap, the poorer thermal dissipation. However, this statement was not 100% true because B75 device was confirmed having the worst thermal dissipation compared to device B112 although device B112 was having larger air gap. in addition, A141 device was confirmed having the best thermal dissipation compared to A42 device which used electrical measurement although both devices had negligible air gap. In other words, electrical measurement could identify device with poor thermal dissipation more effectively compared to X-Ray and SAM regardless of whether the thermal dissipation was contributed by air gap or by external factor-wafer process defects.

Table 2: Effectiveness of Electrical Measurement compared to X-Ray and SAM

Device	A141	A42	B75	B112	Remarks
Air Gap	small	very small	2nd Biggest	Biggest	NA
If X-Ray/SAM is used in identifying poor thermal dissipation	Fair Thermal Dissipation	Best Thermal Dissipation	2nd Worst Thermal Dissipation	Worst Thermal Dissipation	General Statement: Bigger air gap, poorer thermal dissipation. But not 100% true.
Electrical measurement is used in identifying poor thermal dissipation (Before Parameter Change)	Can't distinguish the good and poor thermal dissipation device				
Electrical measurement is used in identifying poor thermal dissipation (After Parameter Change)	Best Thermal Dissipation	Fair Thermal Dissipation	Worst Thermal Dissipation	2nd Worst Thermal Dissipation	Electrical measurement can identify device with poor thermal dissipation effectively compared to X-Ray and SAM

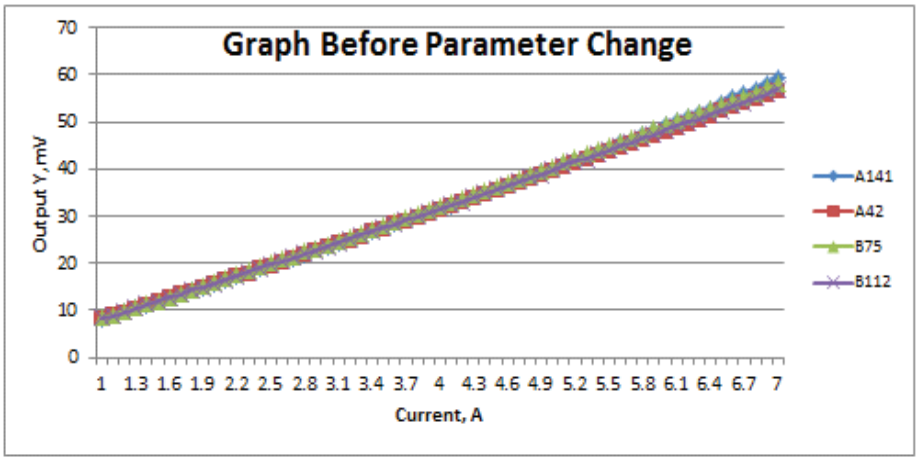

Figure 7: Graph Before "Parameter Change"

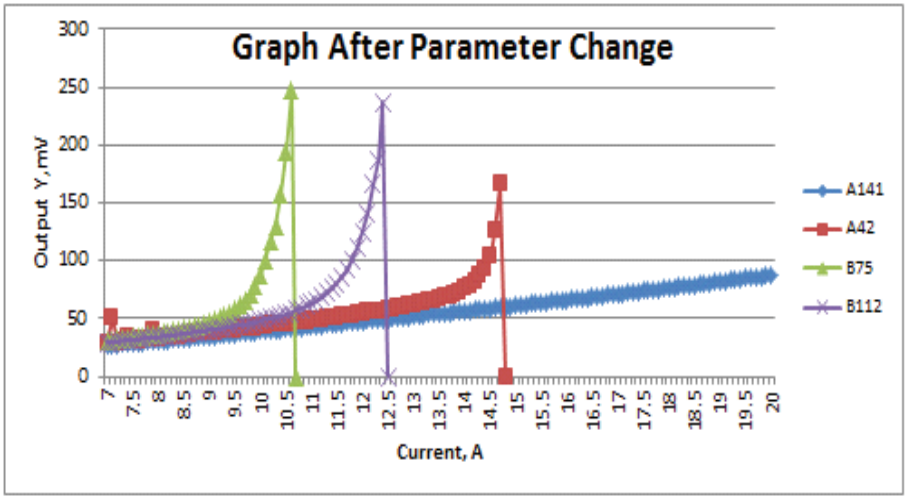

Figure 8: Graph After "Parameter Change"

4.0 CONCLUSION

In conclusion, the advantages of using Electrical measurement in identifying poor thermal dissipation device compared to X-Ray or SAM have been discussed. The inefficiency of electrical measurement in identifying poor thermal dissipation device was also solved using TRIZ approach which has been demonstrated systematically. Principle Parameter Change (PC) provides another perspective in solving the electrical measurement inefficiency problem. Device with air gap is poorer in thermal dissipation compared to device without air gap. However, devices with negligible air gap can have poor thermal

dissipation due to some weaknesses inherited from wafer processes. Such identification of poor thermal dissipation in microelectronic device can be achieved by using electrical measurement with "Parameter Change" of TRIZ principle.

REFERENCES

[1] D.C. Katsis and J. Daniel, "A Thermal, Mechanical, and Electrical Study of Voiding in the Solder Die-Attach of Power MOSFETs" Components and Packaging Technologies, Vol. 29, No.1, 127-36. March 2006.

[2] S. Wolfgang, "Void-Detection in Power Transistors for the automotive use". Master Thesis, Infineon Technologies AG. 2007.

[3] H.Schulze, F. Niedernostheide, F. Pfirsch and R. Baburske,"Limiting Factors of the Safe Operating Area for Power Devices", IEEE Transactions on Electron Device, Vol. 60, No.2, 551–562. February 2013.

[4] T.S. Yeoh, T.J. Yeoh, and C.L. Song, "TRIZ Systematic Innovation In Manufacturing". Firstfruits Publisher, Malaysia. 2012.

[5] J. Chou, "Advanced Engineering Informatics An ideation method for generating new product ideas using TRIZ, concept mapping, and fuzzy linguistic evaluation techniques". Advanced Engineering Informatics, Vol.28, No.4, 441–454. 2014.

[6] P. Jiang, J. Zhai, Z. Chen and R. Tan, "The Patent Design Around Method Based on TRIZ", Proceeding 2009 IEEE IEEM, 1067–1071. 2009.

[7] Y.T. Jin, "TRIZ: Application of Advanced Problem Solving Methodology (ARIZ) in Manufacturing", International Electronic Manufacturing Technology Conference. 2010.

[8] Solid Creativity, 2014. TRIZ40 [online] Available at: http://www.triz40.com/TRIZ_GB.php [Accessed on 5 April 2014]

[9] C. Xu, X. Guo, H. Jiang, and Z. Zhang, "With Temperature Difference Air Flow Sensor", International Conference Electronic Packaging Technology, 655–59. 2014.

MINIMIZING NUMBER OF DEFECTS IN NICKEL PLATING PROCESS USING FACTORIAL DESIGN

N. Q. I. Baharuddin[1], L. Sukarma[2], E. Mohamad[3], A. Saptari[4] and M.R. Salleh[5]

[1,2,3,4,5]Faculty of Manufacturing Engineering,
Universiti Teknikal Malaysia Melaka, Hang Tuah Jaya, 76100 Durian Tunggal, Melaka, Malaysia.

Email: [*1]nurulqasturi@gmail.com; [2]lukman@utem.edu.my; [3]effendi@utem.edu.my; [4]adi@utem.edu.my; [5]rizal@utem.edu.my

ABSTRACT: Product defects may have a serious problem in any manufacturing company because they may increase the production cost due to rework, delays, waste of time and material. The purpose of this study was to investigate significant factors and their interactions in order to find the optimal setting that could reduce the number of defects in nickel plating line. Factorial design has been used as the experimental design technique to identify the critical factors to be controlled. This experiment investigated three different factors using full factorial design. The results were analyzed using Design Expert software. Analysis of variance (ANOVA) was utilized to find the most significant factors. The finding suggested that only one main factor Brightner Correction Solution (BCS) and one interaction factor (BCS and hot COT temperature) affected the number of defects in nickel plating line. The optimum process setting was attained at 22 g/L of BCS and 50°C of hot COT (Cream or Tartar) temperature. A confirmation run using these new settings approved a reduced number of defects in nickel plating process.

KEYWORDS: *Factorial design, Design of Experiment, Product Defects, ANOVA, Nickel Plating Process.*

1.0 INTRODUCTION

Design of experiments (DOE) has been used widely in industries to model and optimize manufacturing processes. This method focuses on minimizing the amount of required experiments for an analysis, while maintaining high quality results [1]. Factorial design, an instrument of DOE, is an excellent statistical method for quality improvement, that is, the optimization of heat treatment variables to eliminate wobbling of gears [2].Using factorial experiment to analyze industrial problems can provide a good result within shortest periods of time with the least costs [3].

The nickel plating process encounters a problem of high reject or defect rate especially in nickel plating production line number five. The Full

Factorial Design experiment was implemented in this study to reduce the number of defective products. This study involved three factors, each with two different levels which is lower and higher. These factors are suspected to have high impact on the number of defects.

A previous study on eliminating wobbling of gears has shown the gear wobbling defects in the gears assemblies can be reduced to less than 1% when applying factorial design [2]. The wobbling of gears can be removed by finding the optimum setting between three heat treatment variables because it causes the multi speed gear assemblies become defective. Factorial design considers a response at every possible combination and set up factors at different levels [2]. The advantage of factorial experiment compared to the conventional experimentation is that all levels of a given factor are combined with all levels of every other factor in the experiment, hence, a possible interaction between factors can be verified.

This study investigated factors and their interactions that had significant contribution to the number of defects in the nickel plating process. The development of regression model helped to explain the relationship between the number of defects of the process and their significant factors or interactions. Moreover, another crucial contribution of this study was to find the optimum setting of parameters which minimized the number of defect products.

2.0 METHODOLOGY

2.1 Determination of the response variable and parameters

Originally, seven factors are assumed to have impact on the number of defects in nickle plating line. However, only three variables were allowed to be adjusted to avoid disruption in production operation. The input variables, therefore, include BCS (Brightner Correction Solution), hot COT (Cream or Tartar) temperature and nickel plating solution temperature.

To prepare the BCS, several steps should be followed and the analysis was performed everyday to ensure the density level as required. The preparation involved titration process as in Figure 1.

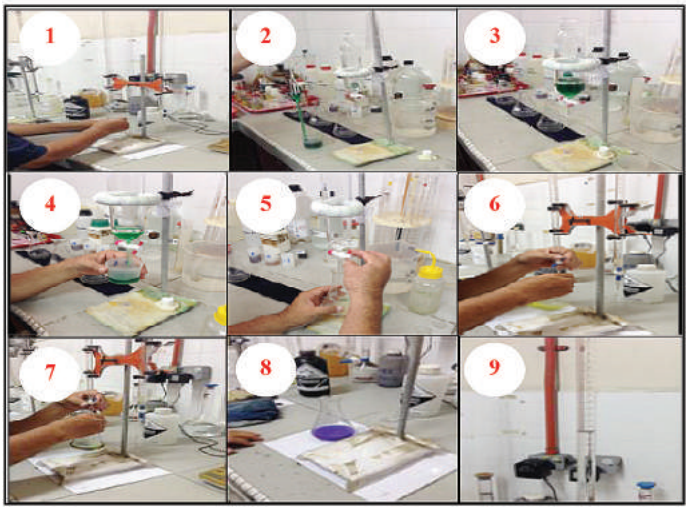

Figure 1: Analysis process of Brightener Correction Solution (BCS)

There are three types of defects in nickel plating process. The first is called yellowish which occurs when color of the product does not meet the required specification. Other types of defects are dull (unbrightened) and rusty. The initial setting parameters can be seen in Table 1.

Table 1: The Initial Settings of the Parameters

Parameters	Level	
	Low	High
Brightener correction solution density (BCS) (g/L)	17	22
Nickel Plating solution Temperature (^{0}C)	52	58
Hot COT Temperature (^{0}C)	50	60

2.2 Data collection and measurement of defects

In this study, data were collected from the result of one shift production run which consisted of 40 lots for every shift. The number of defects in nickel plating process was determined by inspections. Currently, there is no technical method to measure defects for plating process. The inspector was using visual examination by visually looking at the parts and judged whether the parts were rejected or not. This method involved experience whereby every inspector was well trained before they are qualified to do inspection. To avoid variation in the results, only two inspectors were allowed to analyze and detect reject parts. Figure 2 illustrates the conceptual framework on the relationship between independent variables and a dependent variable.

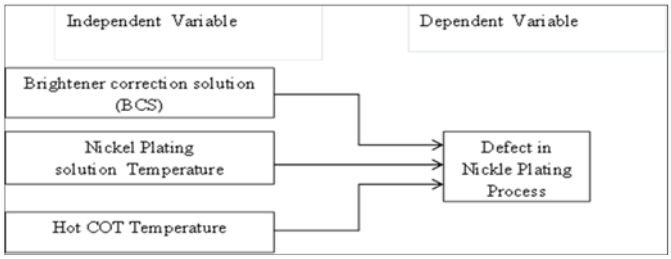

Figure 2: The Conceptual Framework

2.3 Design of experiment

In this experiment, full factorial design was used to study the effect of three independent variables. As the number of factors increases, the number of runs required for a complete replication of the design outgrows the resources of the experiment [5]. Hence, it is practical to use full factorial design when less than five factors are being investigated [2]. This experiment was designed to use a full factorial design that consisted of three factors. Each has two levels which were low and high. With this arrangement, a full factorial design would need 2^3 or equivalent to 8 treatment combinations. This study used the *Yates Standard Order* which was developed by Frank Yates [6] as a method to generate experimental designs in a consistent and logical fashion.. Design matrix in Table 2 shows the 2^3 factorial designs with treatment combinations in Yate's order.

Table 2: Design matrix for 23 full factorial design

Standard Order	Factors		
	(Factor A) Brightener correction solution Density (BCS) (g/L)	(Factor B) Nickel Plating solution Temperature (^{0}C)	(Factor C) Hot COT Temperature (^{0}C)
1	17	52	50
2	22	52	50
3	17	58	50
4	22	58	50
5	17	52	60
6	22	52	60
7	17	58	60
8	22	58	60

Pilot experiment was done simulataneously as the conduct of replicate 1. The purpose of the pilot test was to verify problems that might appear during the experimental run. This was accomplished by running

different random numbers. When the problems were solved, the real experiment could be further conducted on replicate 2 and replicate 3.

In this experiment, ANOVA was applied to identify the most significant variables that influenced the result. This statistical analysis was then applied to the experimental results in order to determine the percent contribution of each factor and factor interactions [6]. This analysis also helped to determine factors which needed to be controlled and not be controlled.

3.0 RESULTS

3.1 Parameter Screening

A visual inspection on the number of defects after the plating process shows different response from different treatment combinations. Table 3 presents the percentage of defect products for three replication.

Table 3: Full Factorial Experimental Results

Standard Order	Factor			Result (% of Defect)		
	A	B	C			
	(Brightener correction solution (BCS) (g/L)	Nickel Plating solution Temperature (^{0}C)	Hot COT Temperature (^{0}C)	Replicate 1	Replicate 2	Replicate 3
1	17	52	50	26.31	35.00	35.13
2	22	52	50	10.00	8.57	20
3	17	58	50	48.50	37.50	10.81
4	22	58	50	7.50	27.50	2.63
5	17	52	60	27.27	25.64	19.44
6	22	52	60	17.50	8.10	22.5
7	17	58	60	10.52	13.88	15
8	22	58	60	17.50	28.00	5.71

According to the results, run order number 3 in replicate 1 produced the highest percentage of defect which was 48.5%. Run order number 3 was a combination of 17 g/l of BCS, 58°C of Nickle Plating Solution Temperature and 50°C of Hot COT Temperature. The run order number 4 in replicate 3 produced the lowest percentage of defect which was 2.63%. Run order number 4 involved 22 g/l of BCS, 58°C of Nickle

Plating Solution Temperature and 50°C of Hot COT Temperature. In order to know the significant factor of the model, the data were analyzed using Design Expert software to determine the analysis of variance (ANOVA), regression model and graphical data.

3.2 Half Normal Plot

Figure 3 shows the resulting plot generated by Design Expert software for number of defect products with all big effects selected according to hierarchy. In this plot, five of the effects (B, C, AB, BC and ABC) fell on or close to the line. On the contrary, the effects of A and AC were relatively separated from the other effects. They, obviously, did not fall on the line. Therefore, both effects should be assumed as significant factors. In other words, both factors A and AC were important and needed to be investigated and analyzed further to see how they influenced the response of variable namely the number of defects.

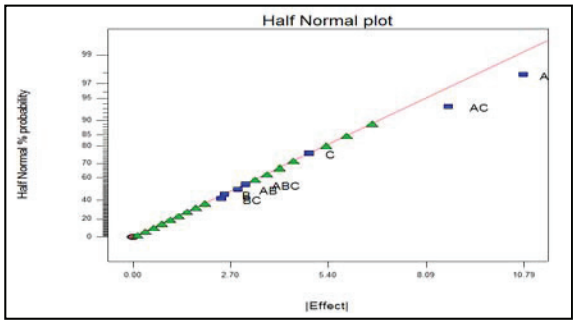

Figure 3: Half-normal Plot Effects for Number of Defects

3.3 Analysis of Variance

Analysis of variance was applied to confirm which factors and their interaction contributed significantly to the number of defects. Figure 4 demonstrates the ANOVA summary for each factor that consists of BCS density, nickel plating solution temperature, hot COT temperature and all interactions among the factors.

ANOVA for selected factorial model

Analysis of variance table [Partial sum of squares - Type III]

Source	Sum of Squares	df	Mean Square	F Value	p-value Prob > F	
Model	1296.68	3	432.23	4.77	0.0114	significant
A-BCS	*698.65*	*1*	*698.65*	*7.72*	*0.0116*	
C-Hot COT 1	*142.06*	*1*	*142.06*	*1.57*	*0.2248*	
AC	*455.97*	*1*	*455.97*	*5.04*	*0.0363*	
Residual	1810.73	20	90.54			
Lack of Fit	*182.73*	*4*	*45.68*	*0.45*	*0.7717*	*not significant*
Pure Error	*1627.99*	*16*	*101.75*			
Cor Total	3107.41	23				

Figure 4: ANOVA result for Number of Defects (all big effects selected)

"Prob>F" often reported on a scale from 0 to 1. If the p-value was less than 0.05 , then, the factor has significant effect on the response, providing at least 95% confident for all results [5]. In this case, A (BCS) with p-value of 0.0116 and AC (BCS and Hot COT Temperature) with p value of 0.0363 were significant since both of p-value were less than 0.05. Even though AC was significant, the main factor C was not significant.

3.4 Regression Model

In addition to graphical analysis, regression analysis was used to find the regression coefficient. According to the results of ANOVA in Figure 6, two factors (A and AC) were statistically significant (p-value < 0.05). However, to maintain hierarchy, factor C should be included to the model. Therefore, the regression model in terms of coded factors is

$$Y = 20.02 - 5.40\ X_1 - 2.43\ X_3 + 4.36\ X_1X_3.$$

Whereby,
Y is the number of defects,
X1 is the brightener correction solution (BCS) density (g/L),
X3 is the hot COT temperature (^{0}C)

According to the regression coefficient above, the number of defect was low if the BCS was at the high level (+1) and Hot COT was at the low level (-1) which produced the total number of defects of 12.69%.

3.5 Model Validation (Residual Analysis)

Residual is a discrepancy between the predicted value and the actual (observed) value [2]. Figure 5 shows the Normal Plot of Residual.

It is essential to diagnose the residuals and validate the statistical assumption from normal line. According to the Figure 5, the resulting plot is approximately linear. The plot showed no abnormalities and there was no signs of any problem in this data. Therefore, the data satisfied the normality assumption because there was no significant deviations.

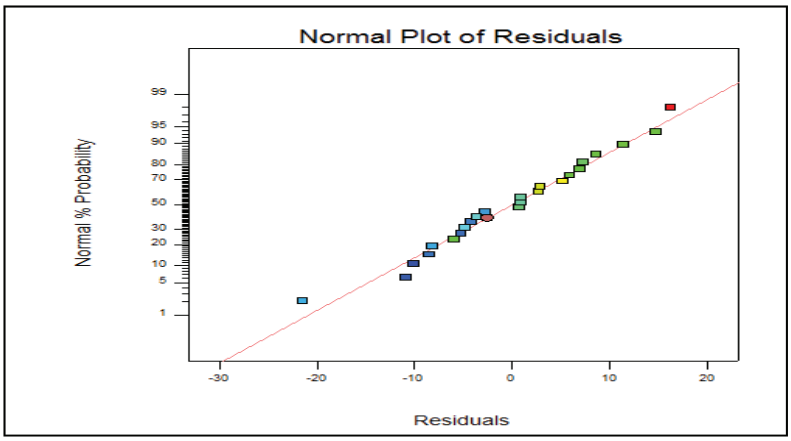

Figure 5: Normal Plot of Residual

3.6 The Optimum Setting of Parameters

One factor plot was used to present the main effect plot of the result. Figure 6 shows the main Effect Plot for BCS. The number of defects would be reduced when the BCS was set for high.

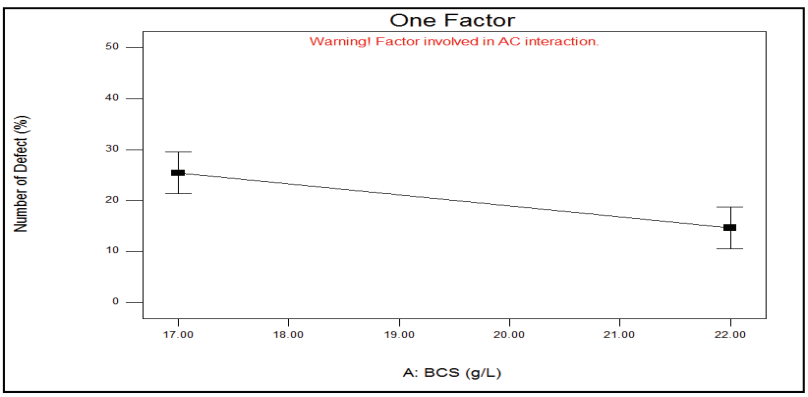

Figure 6: Main Effect Plot for BCS

Furthermore, the highest number of defects (25.42%) was achieved when BCS was at 17 g/L. Then the graph started to decrease to lower level which was 14.63%, when BCS was at 22 g/L. Hence, the optimal condition was achieved when BCS was set at 22g/L.

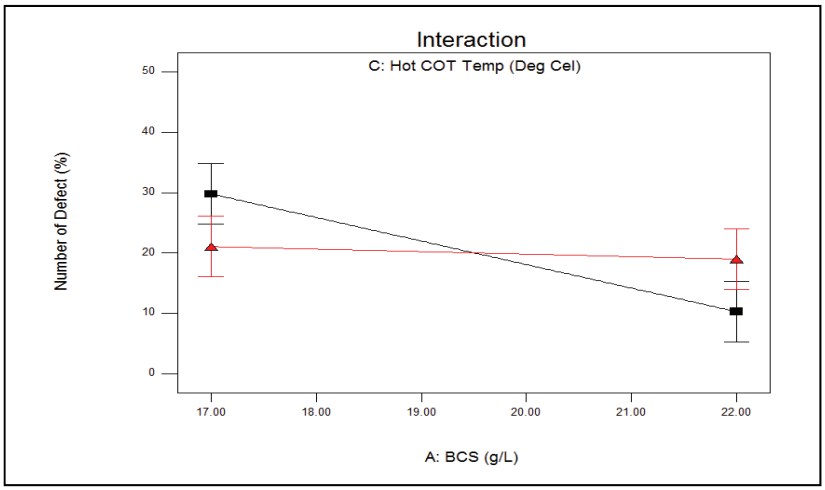

Figure 7 : Interaction Plot of BCS and Hot COT Temperature Vs Number of Defect

According to Figure 7, an interaction exists between BCS and Hot COT Temperature.The two lines overlapped with each other,indicating that the result from one factor was influenced by another factor. From the interaction plot, the lowest number of defect could be achieved when the BCS was 22 g/L (high) and the hot COT was 50 ^{0}C (low). On the contrary, the highest number of defects occured when the BCS was 17 g/L (low) and the hot COT was 50 ^{0}C (high).

If these optimum values were inserted into the regression coefficient model Y = 20.02 – 5.40 X1 – 2.43 X3 + 4.36 X1X3.., the lowest number of defects would be achieved, which was 12.69%, when X1 was replaced by +1 (high level) and X3 was replaced by -1 (low level).

In this study, confirmation run was conducted using these optimum values to see the difference. Within two weeks, there was a reduction in the number of defects. However the production cost also increased because the new setting required high quantity of BCS compared to the usual production run and the cost to buy the BCS was quite high.

For manufacturing firm, producing good quality of product is important to comply with customer requirement. However, they also need to make sure that the production cost does not exceed the budget

because their target is to reduce number of defects without increasing the production cost. Therefore it is hard to continue using the new setting if it may affect the production cost in the long term unless they can find very cheap raw material compared to the current usage. In this case, pre and post comparison cannot be made because the number of defects is analyzed every month and the confirmation run for this study can only be carried out for 2 weeks.

4.0 CONCLUSIONS

In conclusion, an interaction occurs between the two factors which shows that the combination of high level of BCS with the low level hot COT temperature can reduce the number of defects in nickel plating process. In short term, this project has achieved its objectives which is to understand the problem magnitude, the source of the problem, analyze the factors involved and find the optimal setting that can solve the problem. Basically, two parameters are identified as having significant effect in reducing the number of defects in nickel plating process. However, the data collected in the confirmation run are considered as a short term capability. Due to the cost limitation, the company cannot proceed with the new process setting at the longer period of time.

This study is limited in terms of the number of factors involved as only three factors are allowed to be investigated because the company does not want to take a risk by adding other factors that may affect the production process. In order to get accurate results, all the factors or input of the process should undergo the screening experiment to see which factors have important effect to the number of defects. Once the major factors that affect the process have been identified, more complex or multi-level design experiment can be used to identify the optimal settings. For further improvement, the company should take a risk to consider more factors for the experiment. When screening process is done, the interaction of all factors involved can be known. This will facilitate the next phase which is to find the optimal results using Response Surface Methodology so that better and accurate output can be achieved.

ACKNOWLEDGMENTS

The authors extend sincere thanks to the Universiti Teknikal Malaysia Melaka for a continuous support for this study.

REFERENCES

[1] F.Dobslaw, "An Experimental Study on Robust Parameter Settings." P*roceedings of the 12th Annual Conference Companion on Genetic and Evolutionary Computation*, pp. 1999-2002, 2010.

[2] D. C. Montgomery, *Design and Analysis of Experiments*, 8th Edition, New York: John Wiley & Sons, 2012.

[3] L. T. Ek., "Quality Improvement Using Factorial Design". *9th Int Convention on Quality Improvement.* Karachi, Pakistan, pp. 14-15, 2005.

[4] N.Manouselisand C.Costopoulou. "Quality in Metadata: A Schema for e-Commerce." *Online Information Review* 30, No. 3, pp.217-37, 2006.

[5] M.J. Anderson, P.J Whitcomb,. DOE Smplified: Practical Tools for Effective Experimentation 2nd Edition. Productivity Press: New York, 2007.

[6] F.Yates, Experimental Design: Selected Papers. Griffin: London, 1970.

[7] A. Piratelli-Filho and B.D. Giacomo."Application of Design of Experiment Techniques to Estimate CMM Measurement Uncertainty." *Proceedings of American Society for Precision Engineering—ASPE Annual Meeting*, Scottsdale,. 2000.

INVESTIGATION OF FORCES, POWER AND SURFACE ROUGHNESS IN HARD TURNING WITH MIXED CERAMIC TOOL

B., Varaprasad[1] and R. C., Srinivasa[2]

[1]Faculty of Mechanical Engineering,
GVP School of Engineering (Technical Campus), Rushikonda,
Visakhapatnam, India.

[2]Faculty of Mechanical Engineering,
Andhra University, College of Engineering (A),
Visakhapatnam, India.

Email: [*1]varam_prassu@yahoo.co.in; [2]csr_auce@yahoo.co.in

ABSTRACT: Hard turning has been explored as an alternative to cylindrical grinding used in manufacturing parts made of tool steels. In the present study, the effects of cutting speed, feed rate and Depth of Cut (DOC) on cutting force, specific cutting force, power and surface roughness in the hard turning were experimentally investigated. Experiments were carried out using mixed ceramic (Al_2O_3 + TiC) cutting tool having nose radius of 0.8mm, in turning operations on AISI D3 tool steel, heat treated to a hardness of 62 HRC. Response Surface Methodology (RSM) based Central Composite Design (CCD) in Design of Experiments (DOE), was adopted in deciding the number of experiments (20) to be performed with various combinations of input parameters. The range of each one of the three parameters was set at three different levels; namely low, medium and high. The validity of the model was checked by Analysis of Variance (ANOVA). The results yielded that most favorable parameter setting for superior surface finish was acquired at a medium speed of cutting (155 m/min), medium feed (0.075 mm/rev) and low DOC (0.3mm).

KEYWORDS: *Hard turning, Specific cutting force, Surface roughness, AISI D3 and Mixed ceramic.*

1.0 INTRODUCTION

Hard turning is the process of machining hardened steels where the value lies between 45 – 68 HRC (Rockwell hardness) with the latest cutting tools i.e., Poly-crystalline Diamond (PCD), Cubic Boron Nitride (CBN), Poly-crystalline Cubic Boron Nitride (PCBN), Chemical Vapor Deposition (CVD) and Physical Vapor Deposition (PVD) Coated tools and Ceramics. Finishing operation like grinding requires many setups, hard turning is the best option to replace grinding and has several benefits such as coolant elimination, reduced cost of production, enhancement of material properties, reduction in power consumption

and productivity. Ceramic tools are generally used as an alternative to CBN in the manufacturing sector for machining of hard materials such as alloy steels; bearing steels, die steels, graphite cast iron, high-speed steels and white cast iron [1-5]. Therefore hard turning is considered as an alternative process to grinding in a bid to reduce the setup changes, setup cost, setup time, process flexibility, compatible performance characteristics and higher material removal rate and less environmental problems.

Various studies have been conducted to investigate the performance of CBN tool in the machining of tool steels. Bouacha et al. [6] examine effect of cutting parameters on cutting parameters on cutting force and surface roughness in hard turning of AISI 52100 with CBN tool using response surface methodology. The results show that the surface roughness is influenced by feed rate and cutting speed. Aouici et al. [7] conduct extensive experiments on AISI D3 cold steel with mixed Ceramic CC 6050 (with a tool nose radius 0.8 mm, chamfered insert 0.1 mm × 20°), hence, the surface roughness is strongly influenced by the feed rate (87.334 %) and followed by square of feed rate (6.455 %). The surface finish has improved as speed of cutting increases to an extent of 5.03% and deteriorates with the feed rate of 36.672 followed by DOC (27.541%). Initially, cutting force enhances with an increase in feed rate and DOC and reduces with an increase in cutting speed. The lessening in the forces is probably due to temperature increase in the shear plane area, which resulted in the drop in shear strength of the material.

The experimental studies conducted by Aouici et al. [8] yield that the feed force and tangential force are strongly influenced by DOC and cutting speed has negligible influence on these forces while the machining of AISI H11 hardened steels (40, 45, and 50 HRC) is using CBN 7020. Al-Ahmari [9] present empirical models for surface roughness and cutting force in turning operation. The process parameters namely speed, feed, DOC and nose radius are used to develop the machinability model. Two methods used for developing aforesaid models are RSM and Neural Networks (NN). The effect of cutting conditions in a hard turning operation is analyzed by Dilbag and Venkateswara [10]. El Wardany et al. [11] study the quality and integrity of the surface produced during high speed turning of AISI D2 cold work tool steel in its hardened state (60 - 62 HRC) using CBN tool. Kirby et al. [12] predict surface roughness in turning operation using different prediction models. A regression model is developed by a single cutting parameter and vibrations along three axes are chosen for in process surface roughness prediction system. Linear relationship among the parameters and the response is carried out using multiple regression and ANOVA. The results reveal

that for attaining an effective surface roughness prediction model, the cutting speed and DOC may not be necessarily fixed.

Horng et al. [13] present a model by applying RSM and ANOVA techniques to evaluate the machinability of Hadfield steel. Aouici et al. [14] conduct experiments on machining of X38CrMoV5-1 steel treated at 50 HRC by a CBN7020 tool to reveal the influence of the following cutting parameters: cutting speed, feed rate and DOC on surface roughness. They conclude that the surface roughness is sensitive to the variation of feed. Kribes et al. [15] present a statistical analysis to study the influence of cutting conditions on surface roughness in hard turning of 42CrMo4 steel using coated mixed ceramic inserts. Doniavi et al. [16] apply RSM in order to develop empirical model for the prediction of surface roughness by deciding the optimum cutting condition in turning. It is reported that the feed rate influences surface roughness remarkably. With the increase in the feed rate, surface roughness increases. ANOVA results show that feed and speed have more influence on surface roughness than DOC.

Quiza et al. [17] predict ceramic cutting tool wear in hard machining of AISI D2 steel using NN. The models are adjusted to predict tool wear for different values of cutting speed, feed rate, and machining time. One of them is based on statistical regression and the other is based on a multilayer perception neural network. The NN model has a better performance than the regression model in its ability to make accurate predictions of tool wear. Neseli et al. [18] use RSM to optimize the effect of tool geometry parameters on surface roughness in hard turning of AISI 1040 with P25 tool. Gaitonde VN et al. [19] conduct experiments to analyze the effects of DOC and machining time on machinability aspects such as machining force, power, specific cutting force, surface roughness, and tool wear during turning of AISI D2 cold work tool steel using traditional and wiper ceramic inserts.

The present work investigate the influence of process parameters in hard turning of AISI D3 cold work tool steel (62 HRC) using mixed ceramic tool insert (CC6050) on specific cutting force, power and surface roughness. A little work is reported so far in the literature for this combination of tool and work piece material.

2.0 EXPERIMENT PROCEDURE

The work piece material used for experimentation was AISI D3 steel. The circular bar of diameter 70 mm x 360 mm long was prepared. Test sample was trued, centered and cleaned by removing a 2 mm depth of cut from the outside surface, prior to actual machining tests.

2.1 Material, work piece and tool

Due to its high wear resistance, AISI D3 material is usually employed for the manufacture of blanking; drawing dies, punches, rollers profilers, stamping and wood tools and others. A new insert was employed for each run of experiments in order to provide completely identical cutting edge conditions for each test. The chemical composition of the work piece material is given in Table 1. The work piece was heat treated to attain 62 HRC. The process of heat treatment was as follows, the work piece was oil-quenched from 980^{o}C followed by tempering at 200oC. Its hardness value was mean of three readings taken at three different locations on the machined surface. Figure 1 shows the experimental setup.

Table 1: Chemical composition of AISI D3 (wt %)

C	Si	Mn	P	S	Cr	Ni	Mo	Al	Cu	Zn	Fe
2.06	0.55	0.449	0.036	0.056	11.09	0.277	0.207	0.0034	0.13	0.27	Balance

Figure 1: Experimental setup

The tests on the work piece were conducted under dry environment on the lathe Kirloskar; model Turn Master-35, spindle power 6.6KW. The cutting forces were measured by *Kistler* piezoelectric dynamometer (model 9257B). This dynamometer can measure forces in three mutually perpendicular directions i.e. Fx, Fy (0 to 5000N) and Fz (0 to 10000N). The charge generated at the dynamometer was amplified by a Kistler charge amplifier (model 5070A). The signal was acquired by a data acquisition system consists of a personal computer as controller and

cable for PC to charge amplifier connection. The Dyno ware software installed in the PC acquires the force data generated during turning in all three directions. The average value of this force data was used for further analysis. Surface roughness was measured using *Mitutoyo Surftest SJ 210* with measuring range of 17.5mm and skid force less than 400mN. The sample length was 0.8 mm. Average of four readings of surface roughness was recorded on different places of sample surface. These values were obtained without disturbing the assembly of the work piece in order to reduce uncertainties.

The cutting tool used for machining was mixed ceramic tool designated as SNGA 120408 T01020 (*Sandvik make*) that is CC6050. The high hot-hardness and the good level of toughness make the grade suitable as the first choice for hardened steel (50 – 65HRC) in applications with good stability or with light interrupted cuts. Commercial tool holder designated as PSBNR 2525 M 12 (ISO) with the geometry of active part characterized by the following angles: $\chi = 75°$; $\alpha = 6°$; $\gamma = -6°$; $\lambda = -6°$.

2.2 Experiments Design

RSM is a DOE technique used to optimize the number of experiments based on the number of process parameters and their levels on performance characteristics. The RSM is useful for emerging, refining and optimizing the processes, which provides an overall perception of the system outputs within the design space [20]. In order to know performance characteristics in advance, it is necessary to employ empirical models making it feasible to do predictions as a function of operational conditions. Using DOE and applying the regression analysis, the modelling of the desired output against several independent process parameters can be obtained. The RSM is exploited to designate and identify the impact of interactions of different process parameters on the performance characteristics when these are varied simultaneously. In the present investigation, the second-order RSM based mathematical models for surface roughness (R_a) is developed with cutting speed (V_c), feed rate (f), and DOC (a_p) as the process parameters. Figure 2 shows a flow diagram of methodology adopted for the present work.

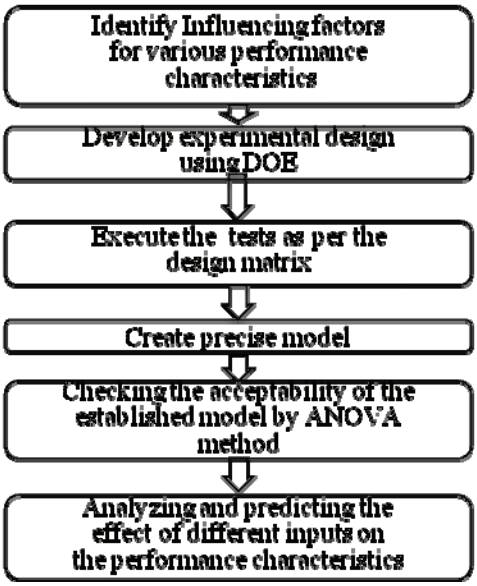

Figure 2: Proposed methodology

In the current study, the quantitative form of the relationship between the desired response and independent input process parameters [20] can be represented by

$$Y = \emptyset(V_c, f, a_p) \tag{1}$$

Where Y is the output and Ø is the acknowledgment function. In the present investigation, the RSM based algebraic models for cutting power, specific cutting force and surface roughness have been developed with speed of cutting(V_c), feed (f) and DOC (a_p) as the action parameters. The acknowledgment apparent blueprint for three factors [24] is accustomed by

$$Y = a_0 + a_1 V_c + a_2 f + a_3 a_p + a_{12} V_c f + a_{13} V_c a_p + a_{23} f a_p + a_{11} V_c^2 + a_{22} f^2 + a_{33} a_p^2 \tag{2}$$

Where Y is desired response and a_0 is the free term of the regression equation, the coefficients a_1, a_2, a_3 and a_{11}, a_{22}, a_{33}……. are the linear and quadratic terms, respectively, while a12, a13,..a23 are the interacting terms.

Three levels are identified for each cutting variable as given in Table 2. The levels of variable are chosen as per recommendations made by the cutting tool manufacturer. Three variables of cutting at three levels

led to a total of 20 tests in DOE. The experimental plan is developed to evaluate the influence of cutting speed (V_c), feed rate (f) and DOC (a_p) on the power (P), specific cutting force (K_2) and surface roughness (R_a) determined from the following equations:

$$\text{Power (P)} = F_2 \times V_2 \tag{3}$$

The value of specific cutting force is generally calculated by the formula given below

$$K_z = \frac{F_z}{f \times a_p} \tag{4}$$

Where, a_p is the DOC. The experimental values of Power, specific cutting force and surface roughness are given in Table 3.

Table 2: Assignment of the levels to the variables

Parameters	Levels		
	-1	0	+1
Speed(m/min)	145	155	165
Feed(mm/rev)	0.05	0.075	0.1
DOC (mm)	0.3	0.6	0.9

3.0 RESULTS AND DISCUSSION

Table 3 shows all the values of the performance characteristics, power (P), three cutting forces (F_x), (F_y) & (F_z), specific cutting force (K_z) and surface roughness obtained when analyzing the influence of the cutting speed (V_2), feed rate (f), and DOC (a_p). The surface roughness is obtained in the range of 0.71 – 2.27μm; specific cutting force 3.1206 - 9.5333 kN/mm2 and power 0.273 - 0.951kW.

Table 3: Values of cutting forces, power, specific cutting force and surface roughness

Sl. No.	Speed (m/min)	Feed (mm/rev)	DOC (mm)	F_x (N)	F_y (N)	F_z (N)	Specific Cutting Force (kN/mm2)	Power P (kW)	R_a (μm)
1	145	0.050	0.3	106.0	138.0	113.0	7.5333	0.273	1.33
2	165	0.050	0.3	098.0	206.7	102.7	9.6000	0.396	1.88
3	145	0.100	0.3	115.0	242.0	150.0	5.2500	0.381	0.90
4	165	0.100	0.3	122.0	254.1	194.6	6.4866	0.535	0.82
5	145	0.050	0.9	321.5	300.0	289.0	6.4222	0.698	2.06
6	165	0.050	0.9	283.7	325.2	312.1	7.6888	0.951	2.11
7	145	0.100	0.9	341.2	340.0	335.0	3.7222	0.809	1.10
8	165	0.100	0.9	332.0	290.0	280.5	3.1206	0.772	0.91
9	145	0.075	0.6	212.6	279.0	220.0	4.8889	0.531	0.84
10	165	0.075	0.6	228.3	290.7	245.3	5.4511	0.674	0.93
11	155	0.050	0.6	213.1	256.0	216.4	7.2133	0.559	2.27
12	155	0.100	0.6	250.3	325.0	310.5	5.1750	0.802	0.93
13	155	0.075	0.3	104.9	170.0	125.0	5.5555	0.322	1.05
14	155	0.075	0.9	298.5	273.4	263.1	3.8996	0.679	0.83
15	155	0.075	0.6	230.0	284.7	252.2	5.6044	0.651	0.71
16	155	0.075	0.6	235.0	274.0	260.0	5.7777	0.671	0.71
17	155	0.075	0.6	245.0	282.0	258.0	5.7333	0.666	0.73
18	155	0.075	0.6	252.0	278.0	248.0	5.5111	0.640	0.75
19	155	0.075	0.6	253.0	280.0	262.0	5.8222	0.676	0.88
20	155	0.075	0.6	260.0	282.0	255.0	5.6666	0.658	0.92

3.1 Statistical Analysis

The results of ANOVA for power (P), specific cutting force (K_z) and surface roughness (R_a) are shown in Table 5, 7 and 9. Table 4, 6 and 8 show the details of estimated regression coefficients. This analysis is done out for a 5 % significance level, i.e., for a 95 % confidence level. ANOVA has been applied to check the adequacy of the developed models. ANOVA table consists of sum of squares and degrees of freedom. The sum of squares is performed into contributions from the polynomial model and the experimental value.

Power is influenced by Speed, DOC and DOC2 and is expressed by equation (5). Table 5 represents the ANOVA table for response surface quadratic model for Power P (kW). The value of "Prob." in Table 5 for model is less than 0.05 which specifies that the model is noteworthy, which is appropriate as it directs that the terms in the model have a major effect on the output.

$$Power\ (P) = 0.612465 + 0.063605 \times Speed + 0.200386 \times DOC - 0.098155 \times DOC^2 \quad (5)$$

Table 4: Estimated Regression Coefficients for Power (kW)

Term	Coef	SE Coef	T	P
Constant	0.612465	0.02408	25.434	0.000
Speed	0.063605	0.02215	2.871	0.017
Feed	0.042165	0.02215	1.904	0.086
DOC	0.200386	0.02215	9.046	0.000
Speed*Speed	0.003540	0.04224	0.084	0.935
Feed*Feed	0.080999	0.04224	1.918	0.084
DOC*DOC	- 0.098155	0.04224	-2.324	0.043
Speed*Feed	-0.032357	0.02477	-1.307	0.221
Speed*DOC	-0.007718	0.02477	-0.312	0.762
Feed*DOC	-0.039353	0.02477	-1.589	0.143
S = 0.0700472 PRESS = 0.464736 R-Sq = 91.29% R-Sq(pred) =17.46% R-Sq(adj) = 83.44%				

Table 5: Analysis of Variance for Power (kW)

Source	DF	Seq SS	Adj SS	Adj MS	F	P	%Con	Remarks
Regression	9	0.513993	0.513993	0.057110	11.64	0.000		Significant
Speed	1	0.040456	0.040456	0.040456	8.25	0.017	7	Significant
Feed	1	0.017779	0.017779	0.017779	3.62	0.086	3	Insignificant
DOC	1	0.401545	0.401545	0.401545	81.84	0.000	72	Significant
Speed*Speed	1	0.000228	0.000034	0.000034	0.01	0.935	0	Insignificant
Feed*Feed	1	0.006249	0.018042	0.018042	3.68	0.084	1	Insignificant
DOC*DOC	1	0.026495	0.026495	0.026495	5.40	0.043	5	Significant
Speed*Feed	1	0.008376	0.008376	0.008376	1.71	0.221	2	Insignificant
Speed*DOC	1	0.000477	0.000477	0.000477	0.10	0.762	0	Insignificant
Feed*DOC	1	0.012389	0.012389	0.012389	2.53	0.143	2	Insignificant
Residual Error	10	0.049066	0.049066	0.004907			8	
Total	19	0.563059					100	

Table 6: Estimated Regression Coefficients for Ks (kN/mm2)

Term	Coef	SE Coef	T	P
Constant	5.2230	0.1665	31.362	0.000
Speed	0.453	0.1532	2.957	0.014
Feed	-1.4704	0.1532	-9.598	0.000
DOC	-0.9573	0.1532	-6.249	0.000
Speed*Speed	0.1262	0.2921	0.432	0.675
Feed*Feed	1.1504	0.2921	3.938	0.003
DOC*DOC	-0.3164	0.2921	-1.083	0.304
Speed*Feed	-0.3374	0.1713	-1.97	0.077
Speed*DOC	-0.3299	0.1713	-1.926	0.083
Feed*DOC	-0.234	0.1713	-1.366	0.202
S = 0.484431 PRESS = 10.8935 R-Sq = 94.55% R-Sq(pred) = 74.69% R-Sq(adj) = 89.64%				

$$Ks = 5.223 + 0.453 \times Speed - 1.4704 \times Feed - 0.9573 \times DOC + 1.1504 \times Feed^2 \quad (6)$$

From the analysis of Table 7, it can be seen that the Speed, Feed, DOC and Feed2 have significant effect on the specific cutting force (Ks). Specific cutting force increases with the increase in feed rate and DOC. Table 9 shows the ANOVA table for response surface. The major effect on surface roughness follows Feed (f) and the product f2. Feed (f) is the most important factor affecting surface roughness.

$$Surface\ roughness\ (Ra) = 0.85164 - 0.499 \times Feed + 0.064591 \times Feed^2 \quad (7)$$

Table 7: Analysis of Variance for Ks (kN/mm2)

Source	DF	Seq SS	Adj SS	Adj MS	F	P	%Con	Remarks
Regression	9	40.7003	40.7003	4.5223	19.27	0.000		Significant
Speed	1	2.0521	2.0521	2.0521	8.74	0.014	5	Significant
Feed	1	21.6204	21.6204	21.6204	92.13	0.000	50	Significant
DOC	1	9.1642	9.1642	9.1642	39.05	0.000	21	Significant
Speed*Speed	1	1.963	0.0438	0.0438	0.19	0.675	5	Insignificant
Feed*Feed	1	3.4062	3.6392	3.6392	15.51	0.003	8	Significant
DOC*DOC	1	0.2753	0.2753	0.2753	1.17	0.304	1	Insignificant
Speed*Feed	1	0.9105	0.9105	0.9105	3.88	0.077	2	Insignificant
Speed*DOC	1	0.8705	0.8705	0.8705	3.71	0.202	2	Insignificant
Feed*DOC	1	0.4382	0.4382	0.4382	1.87	0.202	1	Insignificant
Residual Error	10	2.3467	2.3467	0.2347			5	
Total	19	43.047					100	

Table 8: Estimated Regression Coefficients for Ra

Term	**Coef**	**SE Coef**	**T**	**P**
Constant	0.85164	0.06381	13.347	0.000
Speed	0.042	0.0587	0.716	0.491
Feed	-0.499	0.0587	-8.502	0.000
DOC	0.103	0.0587	1.755	0.110
Speed*Speed	-0.06909	0.11193	-0.617	0.551
Feed*Feed	0.64591	0.11193	5.771	0.000
DOC*DOC	-0.01441	0.11193	-0.126	0.902
Speed*Feed	-0.10875	0.06562	-1.657	0.128
Speed*DOC	-0.07625	0.06562	-1.162	0.272
Feed*DOC	-0.08375	0.06562	-1.276	0.231
S = 0.185611 PRESS = 2.34923 **R-Sq = 93.04% R-Sq(pred) = 52.54% R-Sq(adj) = 86.78%**				

Table 9: Analysis of Variance for surface roughness

Source	DF	Seq SS	Adj SS	Adj MS	F	P	%Con	Remarks
Regression	9	4.6053	4.6053	51170	14.85	0.000		Significant
Speed	1	0.01764	0.01764	0.01764	0.51	0.491	0	Insignificant
Feed	1	2.49001	2.49001	2.49001	72.28	0.000	50	Significant
DOC	1	0.10609	0.10609	0.10609	3.08	0.110	2	Insignificant
Speed*Speed	1	0.4805	0.01313	0.01313	0.38	0.551	10	Insignificant
Feed*Feed	1	1.31328	1.1473	1.1473	33.3	0.000	26	Significant
DOC*DOC	1	0.00055	0.00055	0.00055	0.02	0.902	0	Insignificant
Speed*Feed	1	0.09461	0.09461	0.09461	2.75	0.128	2	Insignificant
Speed*DOC	1	0.04651	0.04651	0.04651	1.35	0.272	1	Insignificant
Feed*DOC	1	0.05611	0.05611	0.05611	1.63	0.231	1	Insignificant
Residual Error	10	0.34452	0.34452	0.03445			8	
Total	19	4.94982					100	

From the above tables the R^2 value for Power (P), Specific cutting force (K_z) and Surface roughness (R_a) is 91.29%, 94.55% and 93.04% respectively.

3.2 Contour Plots

Power, Specific cutting force and Surface roughness should be should be kept to a minimum while machining. An analysis of all performance characteristics have been conducted with the help of contour plots. Contour plot shows a dynamic representation in the study of the performance characteristics. By creating contour plots using minitab16 software for response surface analysis, the optimum region is located by characterizing the shape of the surface. Circular shaped contour represents the independence of factor effects and elliptical contours may indicate factor interaction. The contours of the responses are shown in Figures 3a, 3b and 3c. From the following figures it is clearly understood that power is minimum at low speed and medium feed, minimum at low values of speed and DOC and maximum at high feed and high DOC.

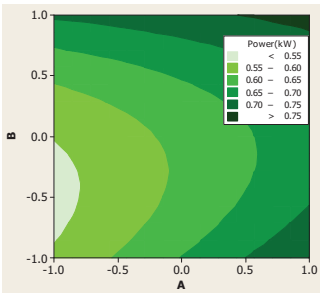

Figure 3(a): Power Vs Speed (A) and Feed (B)

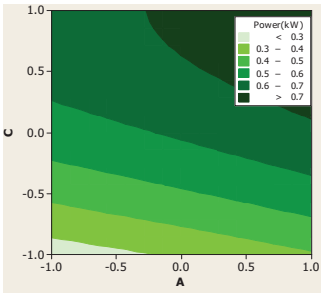

Figure 3(b): Power Vs Speed (A) and DOC (C)

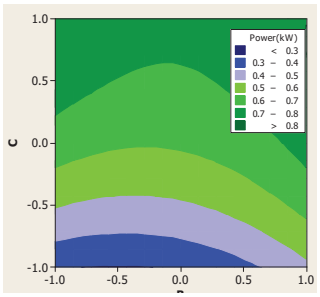

Figure 3(c): Power Vs Feed (B) and DOC (C)

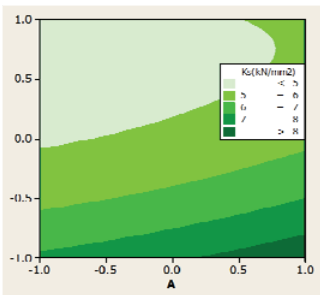

Figure 4(a): Specific cutting force Vs Speed (A) and Feed (B)

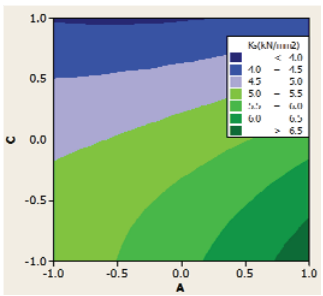

Figure 4(b): Specific cutting force Vs Speed (A) and DOC (C)

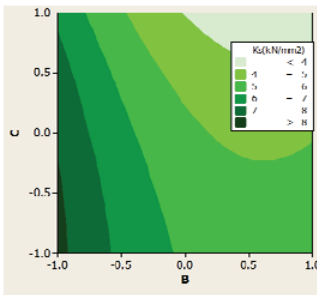

Figure 4(c): Specific cutting force (Ks) Vs Feed (B) and DOC (C)

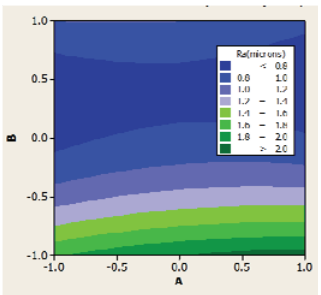

Figure 5(a): Surface roughness (Ra) Vs Speed (A) and Feed (B)

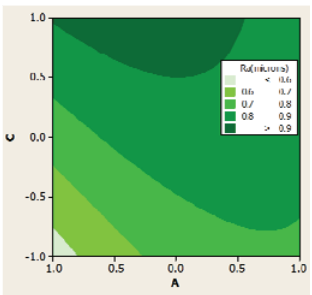

Figure 5(b): Surface roughness (Ra) Vs Speed (A) and DOC (C)

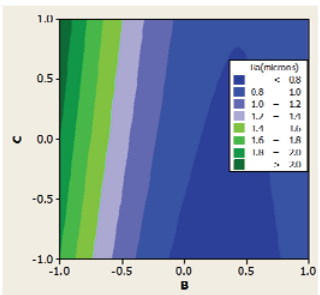

Figure 5(c): Surface roughnes (Ra) Vs Feed (B) and DOC (C)

4.0 CONCLUSIONS

In conclusion, few significant findings from the experiments are as follows;

1) The DOC (72%) has the highest physical as well statistical influence on the cutting power followed by Speed (7%) to perform the machining.
2) Specific cutting force (Ks) is mostly influenced by feed (50%) followed by DOC (21%), then Feed2 (8%) and speed (5%).
3) The surface roughness is strongly influenced by the feed (50%) and followed by feed2 (26%).

From the results, most favorable parameter setting for superior surface finish is acquired at a medium speed of cutting, medium feed and low DOC.

REFERENCES

[1] D. I. Lawarni, N. K. Mehta, and P. K. Jain, "Experimental investigations of cutting parameters influence on cutting forces and surface roughness in finish hard turning of MDN 250 steel," J. Mater. Process Technol. 209, pp. 1092 – 104, 2009.

[2] R. Suresh, S. Basavarajappa, and G. L. Samuel, "Some studies on hard turning of AISI 4340 steel using multilayer coated carbide tool," Measurement 45 (7), pp. 1872 – 1884, 2012.

[3] B. Fnides, M. A. Yallese, T. Mabrouki, and J. F. Rigal, "Application of response surface methodology for determining cutting force model in turning hardened AISI H11 hot work tool steel," Sadhana 36(1), pp. 109 – 123, 2011.

[4] M. W. Azizi, A. Belbah, M. A. Yallese, T. Mabrouki, and J. F. Rigal, "Surface roughness and cutting forces modeling for optimization of machining condition in finish hard turning of AISI 52100 steel," J. Mech. Sci. Technol. 25 (12), pp. 4105 – 4114, 2012.

[5] Z. Hessainia, M. A. Yallese, K. Chaoui, T. Mabrouki, and J. F. Rigal, "On the prediction of surface roughness in the hard turning based on cutting parameters and tool vibrations," Measurement 46(5), pp. 1671 – 1681, 2013.

[6] K. Bouacha, M. A. Yallese, T. Mabrouki, and J. F. Rigal, "Statistical analysis of surface roughness and cutting forces using response surface methodology in hard turning of AISI 52100 bearing steel with CBN tool," J. Refract. Met. Hard Mater. 28, pp. 349 – 361, 2010.

[7] H. Aouici, H. Bouchelaghem, M. A. Yallese, M. Elbah, and B. Fnide, "Machinability investigation in hard turning of AISI D3 cold work steel with ceramic tool using response surface methodology," Int. J. Adv. Manuf. Technol., Vol. 73, Issue 9-12, pp. 1768 - 1775, 2014.

[8] H. Aouici, M. A. Yallese, B. Findes, K. Chaoui, and T. Mabrouki, "Modeling and optimization of hard turning of X38CrMoV5-1 steel with CBN tool: machining parameters effects on flank wear and surface roughness," J. Mech. Sci. Technol. 25(11), pp. 2843 – 2851, 2011.

[9] A. M. Al-Ahmari, "Predictive machinability models for a selected hard material in turning operations," J. Mater. Process Technol. 190, pp. 305 - 311, 2007.

[10] S. P. Dilbag and R. Venkateswara, "Surface roughness prediction model for hard turning process," J. Adv. Manuf. Technol. 32, pp. 1115 – 1124, 2007.

[11] T. I. El-Wardany, H. A. Kishawy, M. A. Elsbestawi, "Surface integrity of die material in high-speed hard machining. Part 1. Micro hardness various and residual stresses," J. Manuf. Eng. 4(122), pp. 32 – 41, 2000.

[12] E. D. Kirby, Z. Zhang, and J. C. Chen, "Development of an accelerometer based surface roughness prediction system in turning operation using multiple regression techniques," J. Ind. Technol. 4(20), pp. 1 – 8, 2004.

[13] J. T. Horng, N. M. Liu, and K. T. Chiang, "Investigating the machinability of Hadfield steel in hard turning with Al2O3/TiC mixed ceramic tool based on response surface methodology," J. Mater. Process Technol. 208, pp. 532 – 541, 2008.

[14] H. Aouici, M. A. Yallese, K. Chaoui, T. Mabrouki, and J. F. Rigal, "Analysis of surface roughness and cutting force components in hard turning with CBN tool: prediction model and cutting conditions optimization," Measurement 45, pp. 344 – 353, 2012.

[15] N. Kribes, Z. Hessainia, M. A. Yallese, N. Ouelaa, "Statistical analysis of surface roughness by design experiments in hard turning," Mechanika 18 (5), pp. 605 – 611, 2012.

[16] A. Doniavi, M. Eskanderzade, and M. Tahmsebian, "Empirical modeling of surface roughness in turning process of 1060 steel using factorial design methodology," J. Appl. Sci. 7 (17), pp. 2509 – 2513, 2007.

[17] R. Quiza, L. Figueira, and J. P. Davim, "Comparing statistical models and artificial neural networks on predicting the tool wear in hard machining D2 AISI steel," J. Adv. Manuf. Technol. 37 (7 – 8), pp. 641 – 648, 2008.

[18] S. Neseli, S. Yaldız, and E. Türkes, "Optimization of tool geometry parameters for turning based on the response surface methodology," Measurement 44, pp. 580 – 587, 2011.

[19] V. N. Gaitonde, S. R. Karnik, L. Figueira, J. P. Davim, "Analysis of machinability during hard turning of cold work tool steel (type: AISI D2)," Mater. Manuf. Process Taylor Francis 24 (12), pp. 1373 – 1382, 2009.

[20] D. C. Montgomery, *Design and Analysis of Experiments*. New York: John Wiley & Sons, pp. 395 – 476, 1997.